PREPARATION AND CHARACTERIZATION OF NOVEL CHIRAL METASURFACES AND THEIR INTERACTION WITH ACTIVE MATERIALS

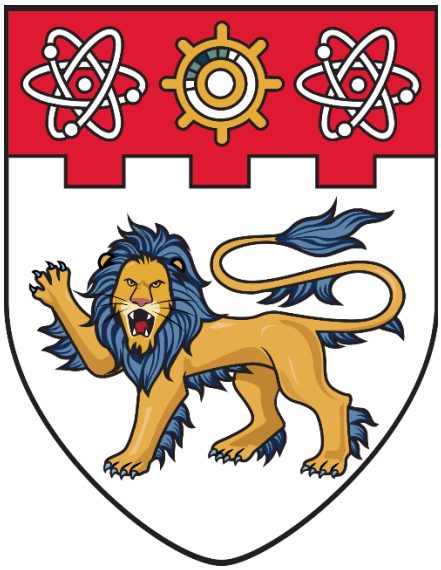

WANG ZENG

SCHOOL OF PHYSICAL AND MATHEMATICAL SCIENCES

NANYANG TECHNOLOGICAL UNIVERSITY

2017

PREPARATION AND CHARACTERIZATION OF NOVEL CHIRAL METASURFACES AND THEIR INTERACTION WITH ACTIVE MATERIALS

WANG ZENG

SCHOOL OF PHYSICAL AND MATHEMATICAL SCIENCES

A thesis submitted to the Nanyang Technological University
in fulfillment of the requirement for the degree of
Doctor of Philosophy

2017

Table of Contents

Acknowledgements

When I was in secondary school, my favorite singer was Stefanie Sun who is a beautiful lady from Singapore and graduated from NTU. From then, I started to learn everything about this lovely country and wished to step on her land one day. Four years ago, I came here NTU to pursue my doctorate degree and future. Here I should thank Ms. Sun first for the power of idol, as well as the companion of those beautiful songs.

The way of Ph.D. will be always tough. This 4-year journey for me was full of surprise, expectancy, suffering, and gratitude. I remember every point I gain and lose, which gave me courage and confidence to carry on. When I watch back, I believe it is these experiences, either sweet or painful, making me more mature and solid.

First, I would like to give my most sincere thanks to my supervisor Prof. Sun Handong who gave me the opportunity to be here and guild me walk along. I learned from Prof. Sun not only the academic knowledge, but also his disposition, spirituality, along with his work ethics and attitudes, which all have a profound impact upon me. Without Prof. Sun's guidance, I cannot even image I can finish this thesis. Also, thanks for the encouragement and patience he gave to me, so I can go out from mistakes and failures to be survived. Then I would like to thank my co-supervisor Prof. Teng Jinghua who provided me great opportunities to work with other fantastic researchers and shared with me very innovative ideas and insightful discussions. Next, I must give my appreciation to my co-supervisor Dr. Giorgio Adamo, who not only trained me to use

FIB and microspectrophotometer, but also help me to solve the experimental problems and improve my academic writings. I need also give my special thanks to Dr. Wang Yue who gave me very help advices on doing research.

Then I want to give my thanks to my great colleagues and friends. Prof. He Tingchao, Dr. Gao Yuan, Dr. Zhao Xin, Dr. Yang Shancheng, Mr. Xiao Lian, Mr. Lim Wenxiang, Ms. Chen Xiaoxuan, Ms. Wang Lin, Mr. Cheng Shijia, Mr. Chan Eng Aik, Mr. Teh Bing Hong, and Mr. Wu Qing Yang Steve for their kind help and enlightening discussions all along.

Last, I want thank my parents and my whole family. It is their unconditional love to support me keep moving forward.

Citations to the published work

Chapter 3 is based on: **Zeng Wang**, Bing Hong Teh, Yue Wang, Giorgio Adamo, Jinghua Teng, and Handong Sun (2017). Enhancing circular dichroism by super chiral hot spots from a chiral metasurface with apexes. Applied Physics Letters, 110(22): 221108.

Chapter 4 is based on: **Zeng Wang**, Yue Wang, Giorgio Adamo, Bing Hong Teh, Qing Yang Steve Wu, Jinghua Teng, and Handong Sun (2016). A Novel Chiral Metasurface with Controllable Circular Dichroism Induced by Coupling Localized and Propagating Modes. Advanced Optical Materials, 4(6), 883-888.

Abstract

Chirality is essential for lives. It is built in numerous crucial bio-molecules to rule their interactions. However, naturally occurring chirality is extremely weak thus rendering highly challenging for the detection and investigation of it. In order to address this problem, artificial stereoscopic chiral nanostructures, also named 3D chiral metamaterials have been proposed and showed huge chiral responses. In contrast to the 3D chiral metamaterials, novel chiral metasurfaces manifest obvious superiorities in terms of viable fabrication and ultra-compact integration, while they are still away from being ideal. One problem is that the chiral response from the chiral metasurfaces is relatively weak, and moreover, the lack of design methodology of chiral metamolecules also hinders the improvements. Another is the tunability of the chiral responses. Due to the complexity of the chiral structures, it is challenging to achieve tunable optical chiral response simply by altering the parameters based on localized surface plasmon resonances, which highly limits the practical usage. This thesis aims at providing solutions for the design of more versatile and advanced chiral metasurfaces possessing enhanced and controllable optical chiral responses and a deeper understanding of the physics underpinning their behaviors. Furthermore, thanks to the resulting tailored chiral responses, the direct CPL emission is obtained via coupling the chiral metasurface with QDs.

Part I: Enhanced circular dichroism from a chiral metasurface with apexes

Manipulating light spin (or circular polarization) is an important research field and may find broad applications from sensors, display technology to quantum computing and communication. To this end, planar metasurfaces with larger circular dichroism are strongly demanded. However, current planar chiral metasurface structures suffer from either fabrication challenge, especially from near-infrared to visible spectrum, or insufficient circular dichroism. In chapter 3, I demonstrate a chiral metasurface composed of achiral nanoholes which allow for precisely creating apexes in the designed structure. The investigation indicates that the apexes act as super chiral hot spots and enable the highly concentrated near-field optical chirality leading to a remarkable enhancement of circular dichroism in the far-field. A 4-fold enhancement of the circular dichroism and a strong optical activity of ~15 degrees have been experimentally achieved. Besides the enhanced chirality, my design genuinely overcomes the nanofabrication challenge faced in existing planar chiral metasurfaces.

Part II: Controllable circular dichroism induced by coupling localized and propagating modes

The enhanced chiral response exhibited by chiral metamaterials and metasurfaces is generally attributed to the effect of localized surface plasmon resonances determined by the constituent materials and structure geometry. How the presence of propagating surface plasmon modes influences chirality is still short of investigation. In chapter 4, I introduce a novel chiral metasurface composed of a chiral arrangement of nanoslits

carved in a continuous metal film, in which propagating surface plasmon modes are proved to be powerful in controlling the metasurface's chiral response. Through modifying the coupling between the localized mode and propagating mode, I theoretically raise a very straight-forward strategy and experimentally achieve a remarkably strong chiral response (~4 degrees of CD) in the visible range that can be also finely tuned and, which makes this design suitable for various potential applications, such as chiral sensing. The results clearly highlight the impact of the propagating surface plasmon modes in controlling chiral responses in metamaterials and metasurfaces. Besides, the conductive nature of my continuous metasurface may open up the possibilities for optoelectronic using.

Part III: **Enhanced circular dichroism and circular polarized emission via the coupling between the chiral metasurfaces and colloidal QDs**

Functionalization of quantum dots (QDs) to induce circular dichroism and direct emission of circularly polarized light has been subject of intensive studies, not only because of obvious practical applications, but also to gain a deeper understanding of quantum semiconductor heterostructures. In chapter 5, plasmonic chiral metasurfaces, controllable by design, are combined with achiral CdSe/ZnS quantum dots, which induces remarkable chiral features in the latter: not only giant enhanced circular dichroism, but also a high degree of the circular polarization in the light emitted by the QDs hybridized with the chiral metasurfaces is observed. By probing the response of QDs combined with tunable chiral metasurfaces, I found indication that the induced

chiral features are closely linked to the correlation between the QDs absorption bands and the chiral bands of the metasurfaces. These findings suggest that plasmonic chiral metasurfaces could play an important role in reshaping QDs with useful chiral properties.

Chapter 1. Introduction

1.1 A brief introduction to chirality

Chirality, as a geometrical definition, is used to describe the structural property of an object which cannot be superimposed to its mirror image. The chiral object and its mirror image are also called a pair of enantiomers with opposite handedness. Since the first report of the rotation of plane polarized light by chiral substances in 1815 by Jean-Baptiste Biot[1], the study on chirality never stopped, which not only contributes to the developments of modern food and drug industry, but also is helping to explore the origin of life. Nowadays, more than 90% compounds used for drug synthesis are chiral and the global chiral chemicals market size has reached to USD 39.79 billion in 2015, which still keeps increasing rapidly[2-4].

In nature, nearly all the fundamental biological molecules are chiral, such as DNA and essential amino acids (the building blocks of proteins), and surprisingly, all these chiral amino acids are of the same left handedness despite the both enantiomers have the same possibility to be generated in achiral environment[5]. While, the origin of the homochirality remains one of the biggest mystery on Earth, it is believed that chirality is the first principle for the development of lives. A pair of enantiomers of a certain chemical compound share identical physical and chemical properties, such as density, freezing point, and acidity unless they interact with other chiral receptor as shown in figure 1.1, which results in the extreme difficulty of distinguishing them. As a chiral

machine, human body is very sensitive to the handedness of the intake chiral compounds. Especially in the pharmaceutical and drug industries, the different enantiomers may express absolutely different physiological effects. For example, thalidomide is a drug used against morning sickness of pregnant women, however only one enantiomer has the desired therapeutic function, while the other is highly toxic to cause birth defects. As another example, ethambutol is for patients with tuberculosis, while its enantiomer results in blindness. However, during the normal synthesis process, it is very hard to avoid the synthesis of the unwanted kind of enantiomers[6]. As a result, the pharmacological investigation of both enantiomers of racemic drugs is required by legislation for the safety of drug using, which also means a huge market for the characterization of chiral molecules[3].

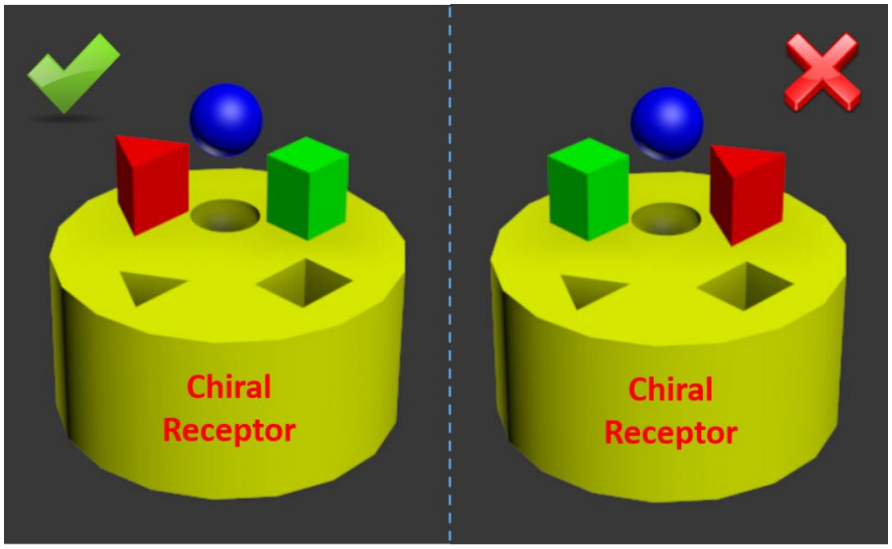

Figure 1.1. *The chiral-chiral interaction*

In order to precisely measure the chiral compounds, various techniques have been developed based on the intrinsic chiroptical effects of these chiral compounds, such as

circular dichroism (CD) and optical activity (OA). Both of them rely on the light-matter interactions, therefore they are also named optically chiral responses. However, due to the extremely weak light-matter interactions, it is still challenging to measure the chiral responses of small chiral molecules. Plasmonic platforms are a promising candidate to enhance the chiral light-matter interactions, and this is the main interest of this thesis.

1.1.1 Circular Dichroism

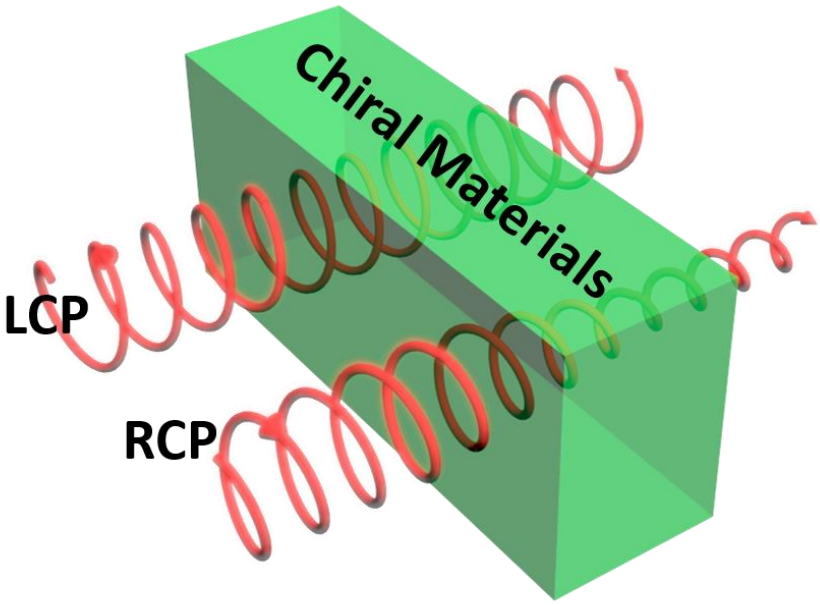

Figure 1.2. *The asymmetric absorption of LCP and RCP when interacting with chiral materials.*

Because of the chiral nature of the circular polarized electromagnetic fields, pairs of enantiomers response differently during the interaction with them, resulting in the optically chiral response: circular dichroism (CD) is the differential absorption between left-handed circularly polarized (LCP) light and right-handed circularly polarized (RCP) light (see figure 1.2), which is defined as:

$$\Delta A = A_L - A_R$$

Where ΔA represents the differential absorption and A_L and A_R indicate the absorption of LCP and RCP light, respectively. As a function of wavelength, CD indicates the refractive index's imaginary part of chiral materials which is dependent on the spin states of external excitation. This excitation could cause an electric transition dipole $\vec{\mu}_{ij}$ and a magnetic transition dipole $\vec{m}_{ij}$ during the electronic transition. The 'i' and 'j' represent initial and final states, respectively. Both of the dipole moments simultaneously contribute to the absorption of radiation, which can be in further concluded as[7]:

$$\mathrm{CD} \propto \vec{\mu}_{ij} \cdot \vec{m}_{ij}$$

While for achiral materials, the electronic transition effect is mostly dominated by the electric transition dipole without symmetry breaking, which as a result vanishes CD.

As the main tool to determine the chirality, CD spectroscopy has a broad range of applications, for example, CD is used to investigate the secondary structure of biological molecules which can be precisely reflected by their CD spectra. In this thesis, CD measurement is a crucial experimental part for characterizing my proposed chiral nanostructures. More detailed information about the experimental setup will be given in the chapter 2.

1.1.2 Optical Activity

Chiral materials, such as sugar solutions, enable the rotation of the plane of polarization of linearly polarized (LP) light when it travels through. This effect was

named optical activity or optical rotation. When linear polarized light propagates in chiral medium, we can investigate by dividing it into LCP and RCP light, which is demonstrated in figure 1.3. Because the presence of chirality, the two kinds of circular polarizations do not experience the same refractive index, which means there is a difference in the phase velocity between LCP and RCP light, As a result, the net linear polarized vector is rotated from the original position by an angle θ, which is determined by:

$$\theta = \pi(n^+ - n^-) \cdot l/\lambda$$

Where n^+ and n^- are the refractive index of LCP and RCP light respectively, and l is the length of chiral medium and λ is wavelength of incident light. Compared with the conventional zero-order waveplates, polarization rotators made from artificial chiral materials could be much more miniaturized thanks to their intense intrinsic chirality. Therefore, it is possible to utilize chiral materials for integrating more advanced optical systems that could be more space-flexible. This is also an important motivation to encourage the studies on the artificial chiral materials to possess stronger chirality than the naturally occurring ones.

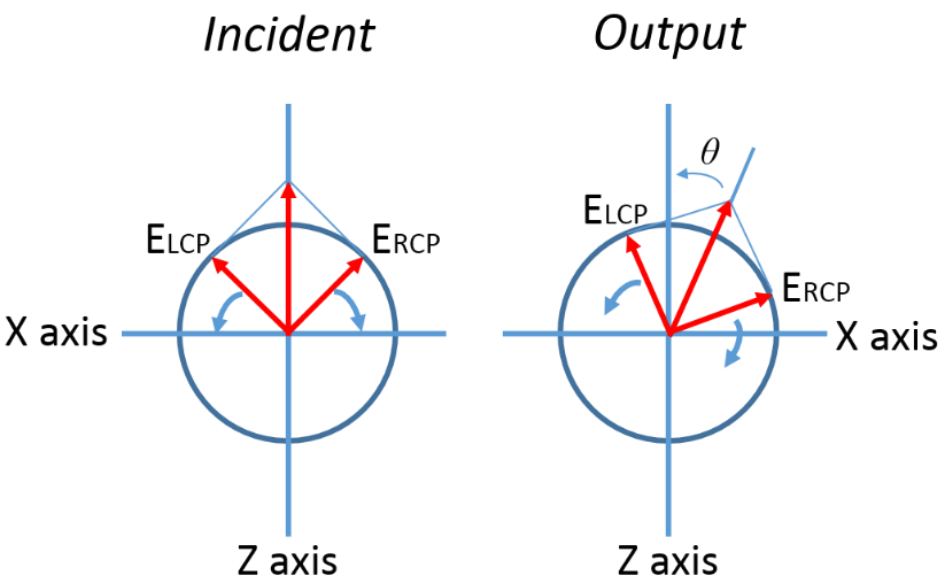

Figure. 1.3. *The schematic of optical activity*

1.2 The connection between chirality and plasmonics

For natural chiral media or molecules, their optically chiral responses are mostly very weak and cannot even be detected by utilizing normal CD technique. The reason is that the tool we utilize to probe their chiral structures is circular polarized light, while its helical pitch ranging in several hundreds of nanometers is much larger than the scales of the chiral features in chiral molecules which mostly being few nanometers or even smaller. This mismatching leads to weak light-matter interactions, resulting insufficient optical signals.

In order to tackle this problem, one way is to enlarge the helical pitches of chiral materials, which have been demonstrated with cholesterical liquid crystals[8] and greatly enhanced chiral responses have been achieved. However, this method is limited by the fact that for the majority of chiral materials with smaller and non-crystalline chiral compounds, it is extremely hard or impossible to re-arrange their chiral structures. Therefore, without changing chiral materials, the other path is to generate electromagnetic fields possessing much stronger optical chirality for triggering more effective chiral-like light-matter interactions. By making use of plasmonic effects, chiral metamaterials and metasurfaces designed with artificial chiral structures have been proposed and showed dramatic abilities in manipulating the circular polarizations so as to perform giant chiral optical responses.

The field of plasmonics has been studied for more than 150 years. In 1857, metal

nanoparticles were first optically studied by Michael Faraday [9] and then in 1902, Robert Wood found that the metallic gratings showed the unexplained reflections[10], which was later on proved that it was caused by plasmonic effects.

For noble metals, the harmonic oscillations of electrons driven by external light field on the surface are named as surface plasmon resonance (SPR) which not only can reserve and transfer the information of the incident light on the metal surface, but more significantly, surface plasmons enable vastly enhanced localized field in a subwavelength scale, which cannot be obtained by optical focusing with dielectric lens due to the diffraction limit. Therefore, SPR offers a versatile platform, especially for the field of nanotechnology, to enable much more intense light-matter interaction by greatly surpassing the input electromagnetic waves. It should be emphasized that the improvement of light-matter interaction has been one of most important factors for the progress of modern industries. For examples, it will determine our future energy from more advanced solar cells with more efficient interactions with sunlight, and help to detect the infected fatal viruses in earlier stage to save lives, etc.

1.2.1 Localized surface plasmon resonances

Localized surface plasmon resonances (LSPRs) describe the local oscillation around metal nanoparticles which are much smaller than the wavelength of the incident light, see figure 1.4. This oscillation is determined by the shape, material, size, and is highly sensitive to the surrounding dielectric environments. This resonant oscillation can provide significant wavelength-dependent enhancements in various physical processes during the interaction, such as absorption, scattering, and intensity of the electromagnetic field at the nanoparticle surface.

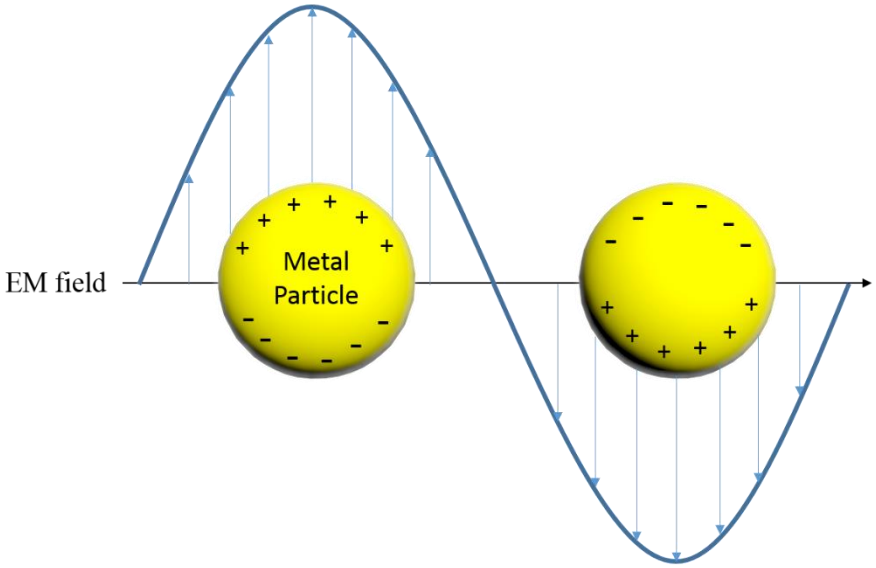

Figure 1.4. *Collective oscillations of the quasi-free conduction electrons*[11]

For a clear physical understanding, we can consider a spherical nanoparticle of radius ***a***, which is much smaller than the wavelength of the excitation light. As displayed in figure 1.4, the light polarized in z direction is illuminated on nanoparticle for the excitation of LSPRs. Due to the static distribution of the electric field around

the nanoparticle, we can employ quasi-static approximation[12] to solve Maxwell's equations. The resulting solution for the electric field around the nanoparticle is solved by:

$$E_{out}(x,y,z) = E_0\hat{\boldsymbol{z}} - \left[\frac{\varepsilon_{in}-\varepsilon_{out}}{\varepsilon_{in}+2\varepsilon_{out}}\right]a^3E_0\left[\frac{\hat{\boldsymbol{z}}}{r^3} - \frac{3z}{r^5}(x\hat{\boldsymbol{x}}+y\hat{\boldsymbol{y}}+z\hat{\boldsymbol{z}})\right]$$

Here, ε_{in} represents the dielectric constant of the metal nanoparticle, and ε_{out} stands for the dielectric constant of the external environment. In this equation, the term in the first brackets manifests the dielectric resonant condition for the nanoparticle. Because of the strongly dependence of ε_{in} on wavelength, when the incident field makes the dielectric constant of the metal approximately equal to $-2\varepsilon_{out}$, the resulting electric field around the nanoparticle will be highly enhanced. For the main plasmonic materials of silver and gold, this resonance can occur in the visible range, which makes it very useful for surface-enhanced spectroscopies. Moreover, diameter and external dielectric constant also play important roles for the resonant responses, which can help to tune the resonant wavelengthes as needed. In further we can deduce the extinction spectrum of the metal sphere[13]:

$$E(\lambda) = \frac{24\pi^2Na^3\varepsilon_{out}^{3/2}}{\lambda\ln(10)}\left[\frac{\varepsilon_i(\lambda)}{(\varepsilon_r(\lambda)+\chi\varepsilon_{out})^2+\varepsilon_i(\lambda)^2}\right]$$

Here, ε_r and ε_i are the real and imaginary components of the metal dielectric function, respectively. N represents the number of the polarizable elements. The factor χ is determined by the shape of the plasmonic nanoparticle, for this case, the sphere

gives the χ as 2. Notably, for complex structures, we have to estimate the values of χ via numerical methods[12,14], such as discrete dipole approximation and the finite-difference time-domain (FDTD) methods[15-17]. In this thesis, I employ the FDTD method in the time domain to obtain the simulated data.

1.2.2 Surface plasmon polaritons

Surface plasmon polaritons (SPPs) comparing to LSPRs (localized mode), are the propagating mode of surface plasmons, which can be excited by photons and electrons and propagate along the metal-dielectric interface[18] (see figure 1.5). However, due to the mismatching of the momentum between the photon and SPP, the direct coupling of them in free-space cannot be obtained. Therefore, in order to compensate the momentum of the incident photon, coupling mechanisms such as the use of prisms and gratings are utilized. As shown in figure 1.5, the electric field of excited SPPs is highly confined on the metal-dielectric interface, which can contribute to greatly enhanced transmission named extraordinary optical transmission[19-22] (EOT) in nanohole array. Also, the intrinsically two-dimensional nature of SPPs provides significant flexibility in engineering SPP based all-optical integrated circuits for optical communications[23-26] and optical computing[27-29] beyond the diffraction limit.

Recently, SPPs have been employed in metasurfaces[30-33] for manipulating the phases and polarizations of the incident light, which enables various applications, such as super lens[34-36], ultra-compact waveplates[30,37-39], etc. In this thesis, SPPs have been

explored and applied to control the optical chiral responses, which have been detailed discussed in the chapter 4.

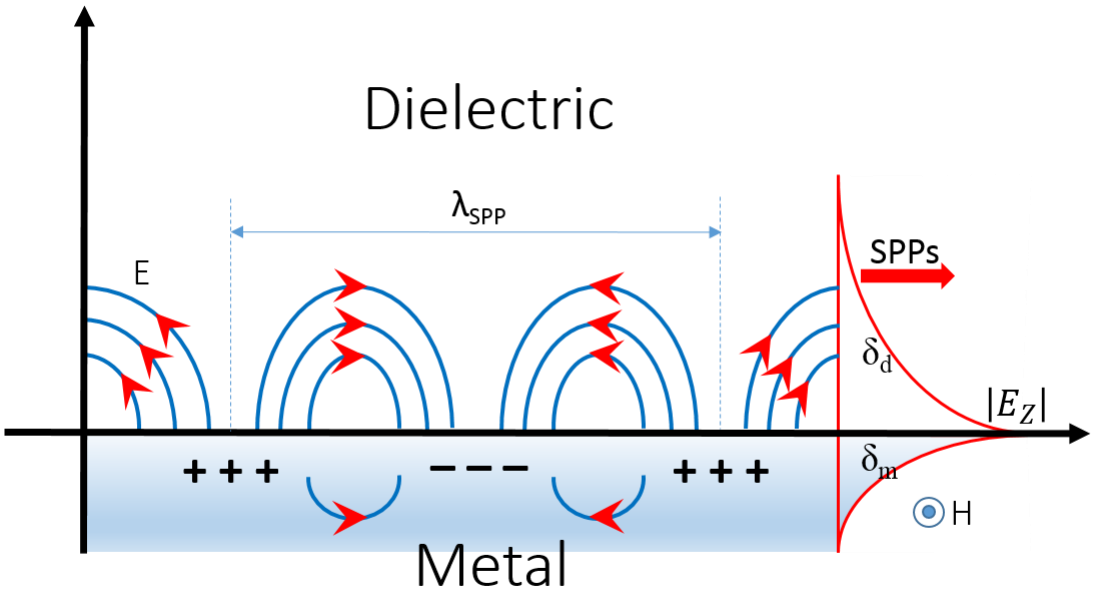

Figure 1.5. *Surface plasmon polaritons*[40] *at a dielectric–metal interface.* δ_d *and* δ_m *represent the skin depth of the SPPs in dielectric and metal, respectively.* λ_{SPP} *shows the wavelength of the SPPs which is normally shorter than that of excitation light due to the dispersion relationship.*

1.3 Chiral metamaterials and metasurfaces

The word 'meta' is from Greek, meaning of 'beyond', which refers to 'beyond conventional materials' for the name of 'metamaterial'. The concept of metamaterials[41] is to engineer materials with unprecedented electromagnetic properties which cannot be found in nature as, for example, materials possessing a negative refractive index[42-

[46]. They provide new degrees of freedoms for manipulating EM waves, from microwave to optical frequency.

Inspired by natural chiral molecules, artificial chiral structures named chiral metamaterials[47-58] have been a crucial branch of metamaterials. Thanks to the enormous progress in nanofabrication technology[59] and subwavelength imaging techniques[60], chiral structures in deep subwavelength scales can be realized experimentally. These chiral metamaterials enable giant chiral responses including CD[52,58,61-65], OA[48,66-68], as well as their nonlinear counterpart SHG-CD[69,70] and SHG-OA[71], which is, on one hand considered from the observation from the far field. On the other hand in the near field of the metamaterials, the surface plasmon resonances not only provide an enhanced EM field in the vicinity, but also generated field with much stronger helix chirality than that of CPL. This field with strong chirality is also named as 'super chiral field' which is demonstrated very useful for sensing bio-molecules with ultra-high sensitivity.

The key ingredient for achieving chiral metamaterials is the design of the chiral unit cell. A properly designed chiral pattern could support asymmetric modes corresponding to different spin states of the incident EM wave, resulting in the giant chiral responses. It has been widely accepted that three dimensional chiral metamolecules could display strong chiral responses because their spatial helix can interact adequately with CPL. However recently, planar chiral metamaterials or chiral metasurfaces have been also demonstrated to show significant optical chiral responses that are comparable to the performances of their three dimensional counterparts. That

makes chiral metasurfaces exceedingly attractive due to their lower complexity of fabrications and more compact for the trend of miniaturization of practical plasmonic devices.

1.3.1 Three dimensional chiral metamaterials

Three dimensional (3D) helical structures have been widely applied for 3D chiral metamaterials. In 2009, Justyna K. Gansel. *et al.* have demonstrated a uniaxial photonic metamaterial composed of 3D gold helices[51] which are arranged on a two-dimensional square lattice. Figure 1.6a displays the process of fabrication, in which an array of helical pores were firstly fabricated, then the gold was deposited by electrochemical method. Lastly, the polymer was etched by plasma with the gold helices remained. The experimental results in the figure 1.6b show that in the wavelength range from 3.5 to 7.6μm, only the left-handed CPL can transmit through, while the other is almost blocked. Further on in the work by Marco Esposito *et al.*, the chiral responses of 3D helices have been extended to the optical range[67]. Focused ion beam induced deposition (FIBID) was employed to realize the multiple-helical structures. It can be noticed in the figure 1.6c, the pitch number from 0.5 to 1.5 can be precisely controlled by this technique. Respectively in the figure 1.6d, with the increase of the pitch number, the chiral responses were raised in a board wavelength range from 420 to 680nm that almost covering the visible range.

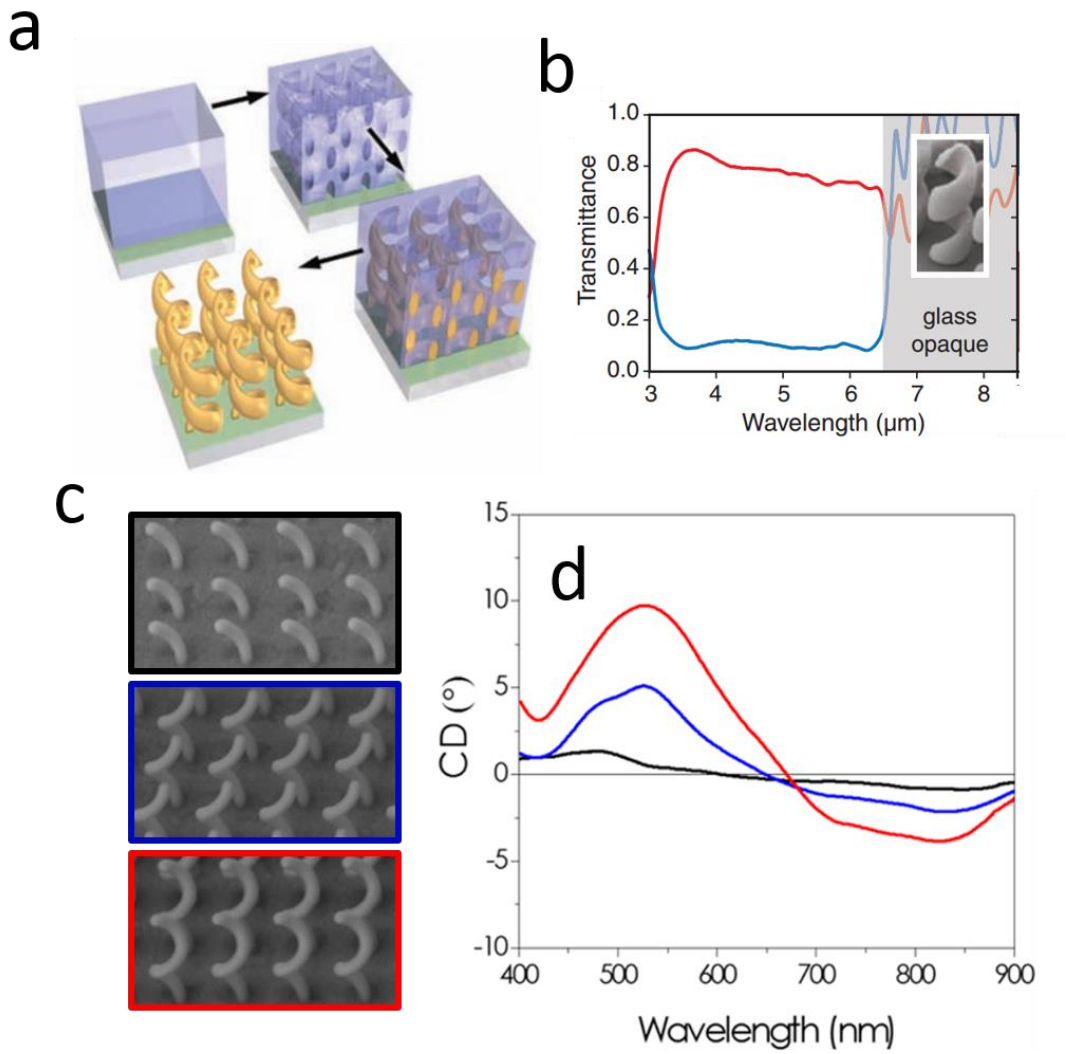

Figure 1.6. *3D helical structures. (a) Fabrication process of 3D gold helices by direct laser writing and electrochemical deposition of gold*[51]*. (b) Asymmetric transmittance of left-handed (red curve) and right-handed (blue curve) CPL with the normal incidence on this chiral metamaterials*[51]*. (c) Scanning electron microscope (SEM) images of the 3D helices array with 0.5 to 1.5 pitched from up to down*[67]*. (d) CD spectra of the 3D helices show an increasing trend with the pitch number added*[67]*.*

Another design strategy of 3D chiral metamaterials is stacking of planar structures. For a single layer, it can hardly generate the optical chirality due to non-chiral property of the metamolecules, while the combinations between the adjacent layers give rise to the rotation power for giant asymmetric responses of different handed CPL. In 2012, Mario Hentschel *et al.* introduced a concept of configurational chirality[54] that is shown in figure 1.7a. It is known that the electronic properties of a chiral molecule are generally influenced by its composite as well as its configuration. Similarly to chiral molecular system, the configurational arrangement of plasmonic nano-disc can possess strong chirality which is displayed in figure 1.7b. The handedness can be switched or even eliminated via altering the position of the single nano-disc on the top layer, which in one aspect demonstrates the near field coupling between the 2 layers results the chiral responses. Moreover, it was shown when the 4 nano-disc with different sizes but also the same chiral arrangement, the chiral responses vanished because of the off-resonant property of the discs, which from another aspect confirmed the resonant coupling is a key for the chiral performances. Another example of dual-layer chiral metamaterials formed by twisted-arcs[55] (see figure 1.7c) was proposed by Yonghao Cui *et al.*, in this work the circular dichroism was in further enlarged to ~0.35 (see figure 1.7d), and meanwhile, both the high transmittance and the subwavelength thickness achieved in this work could enable more practical usages for nano optics and integrated photonics.

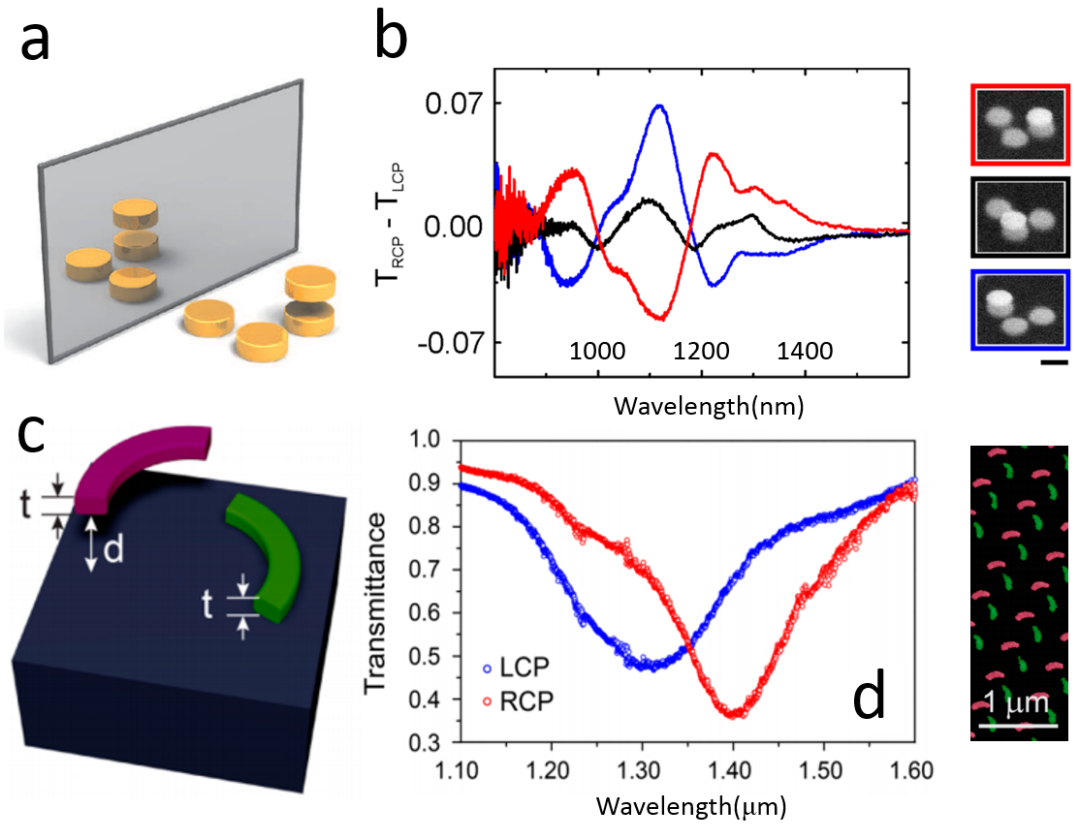

Figure 1.7. *Duel-layer 3D chiral metamaterials. (a)The configurational chiral unit cell composed by gold nano-disc*[54]*. (b)The CD spectra of the 3D chiral metamaterials shown in the figure 1.7a, which is calculated by the differential transmittance of right and left CPL, and the SEM images of samples are put in the right side*[54]*. (c)Duel-layer 3D chiral metamaterials formed by twist-arcs*[55]*. (d) The left side spectra show the giant asymmetric transmittance of left and right CPL and the SEM of the arc sample is arranged on the right of this figure*[55]*.*

1.3.2 Chiral metasurfaces

Although originally discovered in 3D chiral structures, chiral effects can also emerge in a two-dimensional (2D) metasurface, which has been well accepted.

In 2005, the first observed giant optical activity from quasi-planar chiral metamaterial[48] has been reported by Kuwata Gonokami *et al.* This chiral metasurface was composed by gammadion shape meta-atom shown in the figure 1.8a. The perfect mirror image of the rotation degree of the opposite handed patterns in figure 1.8a undoubtedly confirmed the emerge of chiral responses in quasi-2D structure. It was explained the optical chiral response was cause by the asymmetry of light-plasmon coupling at the air-metal and substrate-metal interfaces. Beside the optical activity, the circular dichroism was also reported from the gammadion structures[72], which is shown in figure 1.8b. Although, the demonstrated CD in this chiral metasurface was not as high as the performances of 3D chiral nanostructures, the planar property showed a great potential as a chiral platform in sensing the biomolecules by the chiral surface. In this work, the picogram level detection of some certain chiral materials has been achieved, which, in a practical way, provides a direction for the ultra-sensitive bio-sensing via chiral metasurfaces.

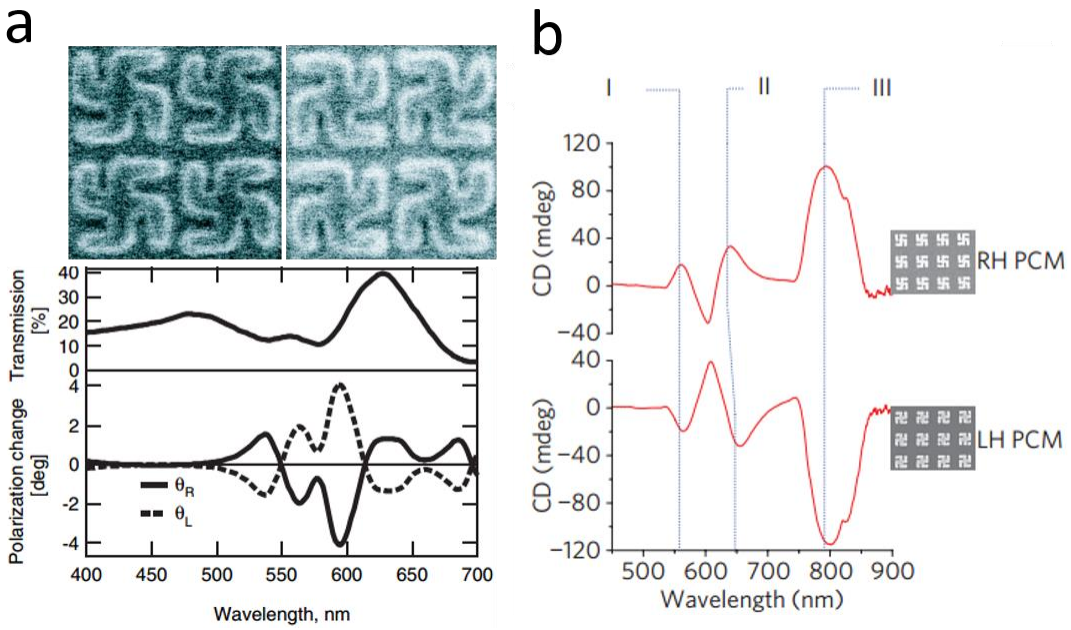

Figure 1.8. *Optical rotation and circular dichroism from chiral metasurfaces. (a) The giant optical activity from gammadion chiral metasurface*[48]*. (b) The circular dichroism from gammadion chiral metasurface for ultra-sensitive biosensing*[72]*.*

For an intrinsic chiral pattern with the normal excitation, the origin of the CD from the chiral metasurfaces is mostly because of the circular polarization dependent electromagnetic field distribution, and this asymmetric field distribution results in an asymmetric absorption for different circular polarizations, which is CD. This physical mechanism was just established in recent years, which was also experimentally proved by several recent reports[61,73]. As displayed in figure 1.9a, the single metamolecule composed by one Au and two Si nanospheres, without an array arrangement and substrate, which means there was no asymmetry caused by the interfaces, can also show

the CD[73]. This optical chiral responses demonstrated the quasi-2D chiral meta-molecule itself can also possess the intrinsic chirality via its heterogeneous composition.

Another more visual work[61] was given by A.B. Khanikaev et al. in 2016, which is displayed in figure 1.9b. In this work, the origin of CD in the chiral metasurface has been experimentally demonstrated via using scattering-type near-field-scanning optical microscopy (s-SNOM) to reveal the circular polarization dependent near field distribution. It can be noticed the pair of enantiomers displayed in the right side of figure 1.9b. The direct mapping under the normal excitation of right circular polarized (RCP) light indicated an asymmetric field distribution that is caused by the intrinsic chiral nature of the pattern. In further, because of the existence of the non-radiative (Ohmic) dissipation, this asymmetric distribution results into the different absorptions that matches the CD from the aspect of far field.

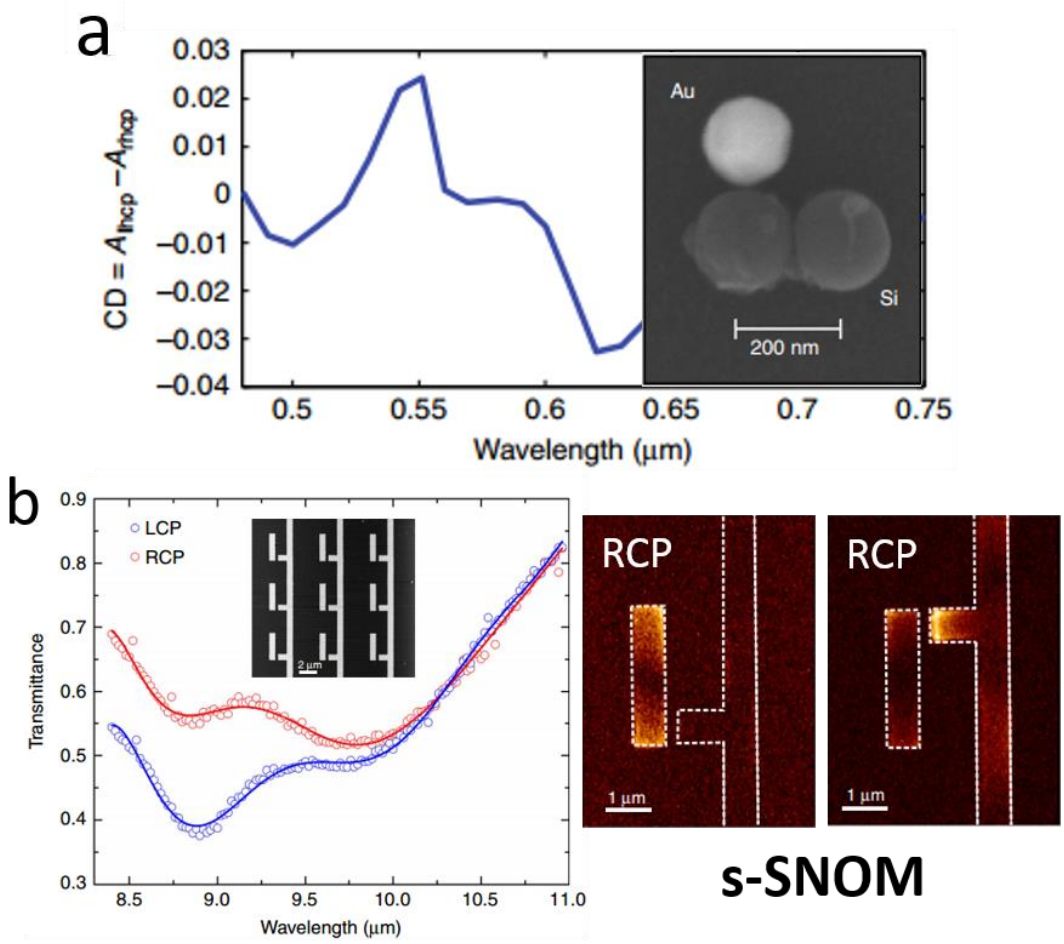

Figure 1.9. *The origin of CD in chiral metasurfaces. (a)The CD spectrum (left side) and SEM image (right side) of a heterogeneous nanosphere trimer*[73]*. (b)The transmittance spectra (left side) of a chiral metasurface excited by LCP and RCP and the s-SNOM measurements of the optical field (right side) above two planar-chiral metasurfaces illuminated by RCP light*[61]*.*

1.4 The application perspective

The tremendous progress in the research of plasmonic chiral nano-structures has enabled numerous possible applications. Under the plasmonic effects of field enhancements, the well-designed plasmonic chiral structures have enabled various applications, such as negative refractive index materials[75], biosensing[72] and ultra-compact waveplates[55]. In the future, we could look forward to smarter, programmable and switchable, chiral nanostructures and chiral metamaterials for more complex enantioselective reactions.

1.4.1 Another path for negative refractive index

Thanks to the extraordinary properties, negative index materials have attracted intense attentions, especially in the area of metamaterials. In a normal way, the achievement of negative refractive index materials requires simultaneously engineered negative permittivity ε and negative permeability μ, which needs the identical resonant bands of both the electric and magnetic responses. With the rise of chiral metamaterials, an alternative route toward negative refraction was given. The strength of the cross-coupling effect can be described by a chiral intensity parameter κ, then we have the constitutive relations of a chiral material is given by:

$$\begin{pmatrix} D \\ B \end{pmatrix} = \begin{pmatrix} \varepsilon_0 \varepsilon & -i\kappa/c \\ i\kappa/c & -\mu_0 \mu \end{pmatrix} \begin{pmatrix} E \\ H \end{pmatrix}$$

Where ε_0 and μ_0 represent the permittivity and permeability respectively in vacuum and ε and μ are the relative permittivity and permeability of the chiral medium. The speed of light in vacuum is defined by c. From this electromagnetic relations, it can be derived[74] the refractive index of LCP and RCP for a normal incidence:

$$n_{\pm} = n \pm \kappa$$

Here, $n = \sqrt{\varepsilon\mu}$ which means the refractive indices of either LCP or RCP can be negative if the κ is big enough. In figure 1.10, two kinds of chiral metamaterials demonstrating negative refractive indices are displayed. A chiral metamaterial[45] with negative refractive indices at terahertz frequencies around 1 THz has been shown in figure 1.10a and b. The degeneracy for the LCP and RCP is raised by the strong chirality κ in this terahertz metamaterial, which contributes to the achievement of negative refractive index. The similar case of U-shaped split ring resonators[75] (SRRs) achieved the negative refractive indices at gigahertz frequency, which is illustrated in figure 1.10c and d. However, for the near-infrared and visible range, it is still challenging to achieve the negative refractive indices by chiral metamaterials due to the insufficient chiral responses. Therefore, it is a main motivation for the research on chiral metamaterials or metasurfaces to possess stronger chiral responses in light frequency, which can be expected for the future studies in this area.

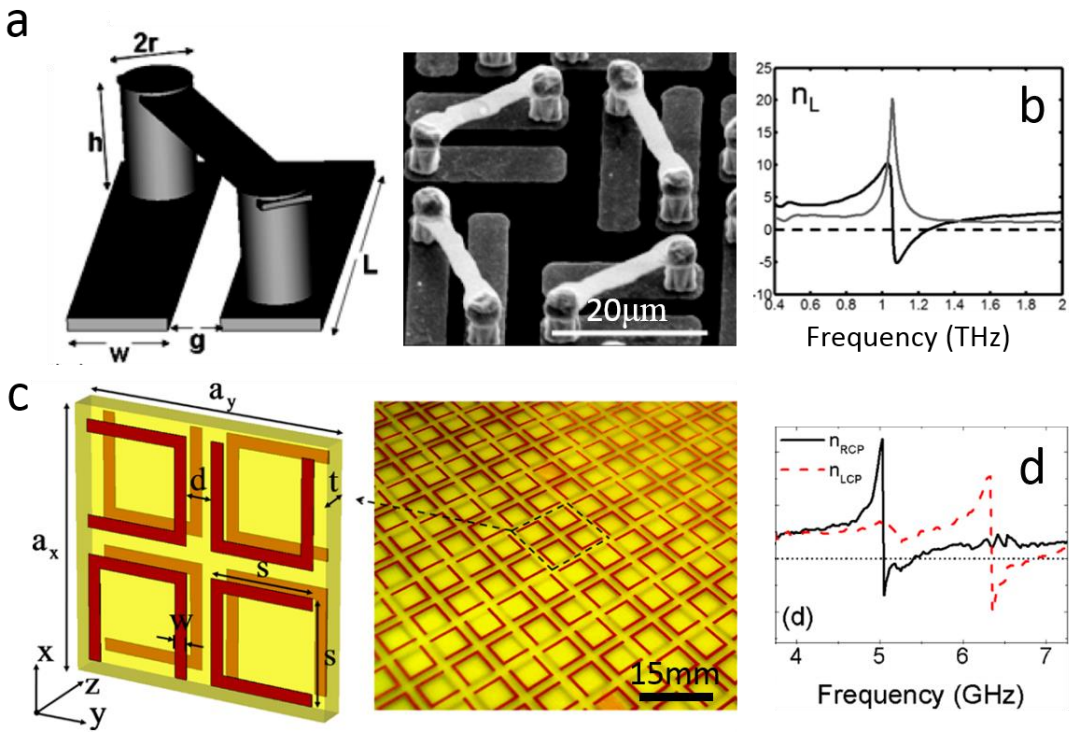

Figure 1.10. *Negative refractive index due to chirality. (a) The schematic of the chiral metamolecule (left side) with resonant band at THz and the SEM image (right side)*[45]*. (b) The experimentally real (black) and imaginary (gray) parts of the refractive index for LCP*[45]*. (c) The schematic of the chiral metamolecule with resonant band at GHz*[75]*. (d) The experimentally real parts of the refractive index for LCP and RCP*[75]*.*

1.4.2 Ultra-sensitive bio-sensing by superchiral field

A chiral object and its enantiomer can interact differently with other chiral objects, which helps to distinguish the pair of enantiomers. This is the principle for sensing chiral biomolecules. Normally, the chiral tool used for probing the chiral biomolecules

is circularly polarized light, which relates to the effect of CD. For a certain chiral molecule, the intensity of the CD signal is proportional to the optical chirality of the incident electromagnetic field. This optical chirality is defined quantitatively by Lipkin[76]:

$$C \equiv \frac{\varepsilon_0}{2}\mathbf{E} \cdot \nabla \times \mathbf{E} + \frac{1}{2\mu_0}\mathbf{B} \cdot \nabla \times \mathbf{B}$$

This formula describes the optical chirality as a time-even pseudoscalar, in which ε_0 and μ_0 respectively represent the permittivity and permeability of free space and **E** and **B** are the time dependent electric and magnetic fields. The physical meaning laid behind is that only if the **E** and **B** have the parallel components, the quantity *C* is valid. Therefore it can be easily calculated that the optical chirality of CPL is constant, which infers that there is no freedom for CPL itself to enhance the chiral interaction between the chiral biomolecules. Recently, it has been demonstrated plasmonic chiral nanostructures can realize the near-field with much larger optical chirality than that of CPL, which dramatically increased the sensitivity of detecting chiral molecules. This enhanced optical chirality is also known as superchiral field.

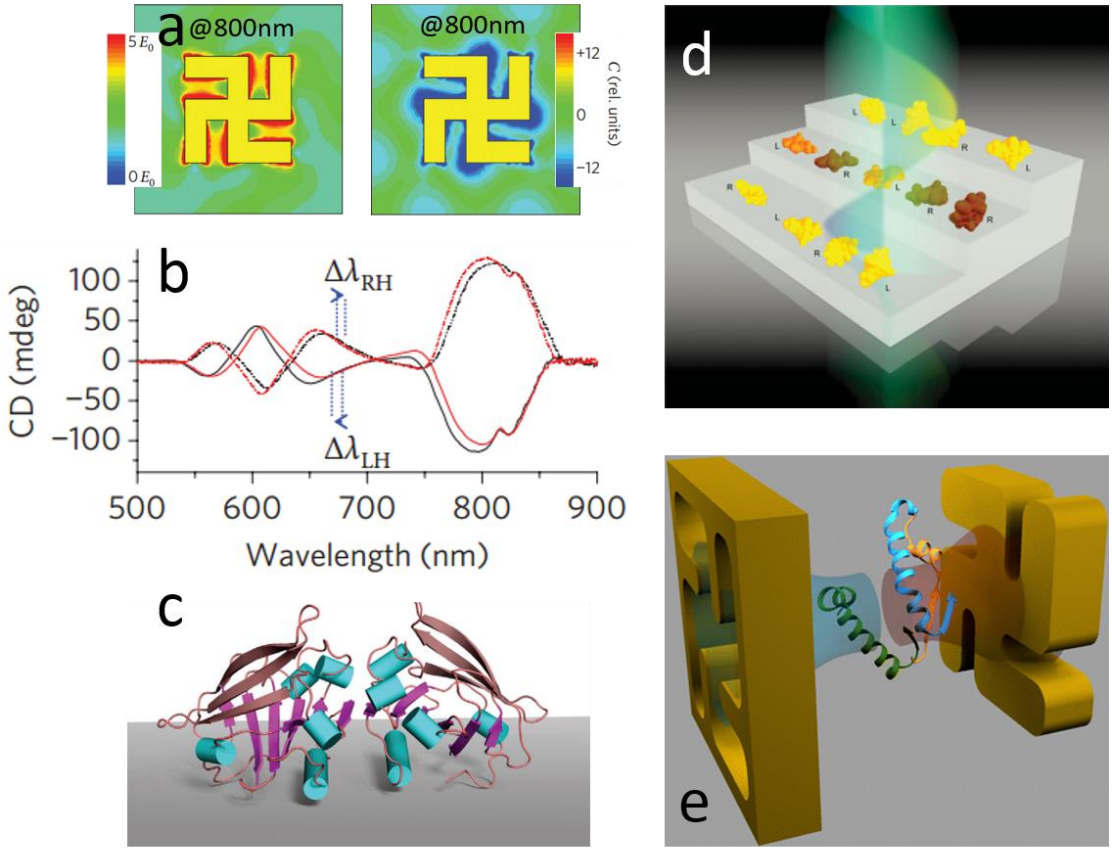

Figure 1.11. *Superchiral field for enhanced biomolecule sensing. (a)The enhanced electric field distribution (left side) and the corresponding enhanced optical chirality distribution (right side) on a gammadion chiral metasurface*[72]*. (b)The CD spectra show opposite shifting directions when put a pair of enantiomers on the chiral metasurfaces that displayed in* ***a***[72]*. (c)The schematic of the pair of enantiomers in* ***b***[72]*. (d)The schematic of putting the chiral molecules at the nodes of the CPL standing waves to enhanced chiral signal*[7]*. (e) Schematic of detecting biomacromolecular secondary structure using superchiral field without relying on measuring effective refractive indices*[77]*.*

The first experimental demonstration of superchiral field for chiral molecule sensing was reported by E. Hendry *et al.* in 2010. It can be noticed in the figure 1.11a, in the vicinity of the chiral metasurface, the field of optical chirality is largely enhanced at the resonant band, as well as the electric field. The chiral molecules with opposite handedness show the difference in the effective refractive indices when interacting with the superchiral field (see figure1.11b and c). Moreover, due to the intense chiral optical environment, the chiral signal was greatly enhanced, which was found to be up to six order higher than the traditional optical polarimetry method. Another path to sense the chiral molecules employing superchiral field was raise by Yiqiao Tang *et al.,* which is illustrated in figure 1.11d. By theoretical calculations[7], it was found out via interacting the chiral molecules with the nodes of a standing wave that generated by two counter-propagating CPL, the enhanced chiral responses can be obtained. Experimental results[78] show an 11-fold enhancement over CPL in discrimination which agrees well with the theoretical predictions. However, the effective range of the nodes in the standing waves is just several nanometers, which makes the positioning of the chiral medium extremely difficult. This may be a problem for practical applications. Other examples, like unitizing chiral solid inverse plasmonic nanostructures[77] (see figure 1.11e), also manifest significant potentials in sensing biomolecules via superchiral field.

1.4.3 Direct CPL emission from active materials

Beside ultra-sensitive biosensing, the near-field enhancement of the metamaterials also bring the opportunity for the coupling with active materials including

semiconductor quantum dots (QDs) and dye molecules. For the hybrid system of metamaterials and emitters, this coupling is intend to manipulate the properties of the emissions, relating to the controlled intensity[79-82], polarizations[83,84] and emitting directions[85,86], which have been well demonstrated and reported. In the case of chiral category, one of the main goals is for achieving direct CPL emissions. One method[87] was presented by Kuniaki Konishi *et al.* that the InAs QDs were embedded in a GaAs-based chiral metasurface displayed in figure 1.12a. This hybrid system shows a degree of CPL around 20% (see figure 1.12b) in the frequency of near-infrared regime. The following improvements[88] have been demonstrated by S. V. Lobanov *et al.* in 2015 which is illustrated in figure 1.12c and d. Compared with the previous work, the only structural change is the chiral metamolecule, which results in a more than 80% of the degree of CPL. The physical origin of the achievements of the direct CPL emissions can be understood in terms of the reciprocity principle taking into account the structural symmetry, which introduces strong imbalance between left and right circularly polarized components.

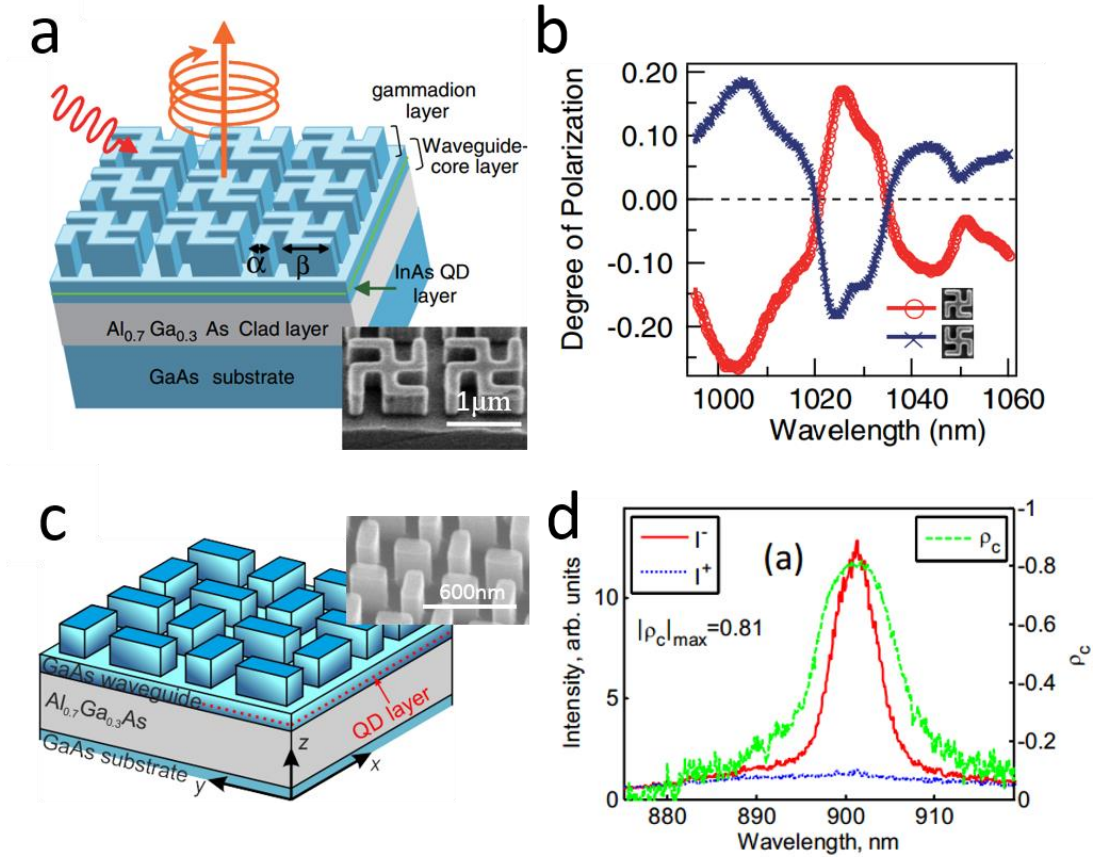

Figure 1.12. *Direct CPL emission of QDs via coupling with chiral nanostructures. (a) Schematic and SEM image of designed gammadion chiral nanostructures*[87]*. (b) Spectra of the CPL degree of the left and right gammadion chiral nanostructures*[87]*. (c) Schematic and SEM image of designed slab chiral nanostructures*[88]*. (d) Spectra of the CPL degree of the right slab chiral nanostructures*[88]*.*

1.5 Objectives and significance of the study

In contrast to 3D chiral metamaterials, novel chiral metasurfaces manifest obvious superiorities in terms of viable fabrication and ultra-compact integration, while there is still a distance away from the ideal. One problem is that the chiral responses from the chiral metasurfaces are relatively weak, and moreover, the lack of design methodology

of the chiral metamolecules also hinders the improvements. Another is the tunability of the chiral responses. Due to the complexity of the chiral structures, it is challenging to achieve tunable optical chiral responses via simply altering the parameters only based on the localized surface plasmon resonances, which highly limits the practical usage. This thesis aims at providing solutions for more versatile and advanced chiral metasurfaces possessing enhanced and controllable optical chiral responses and at gaining a deeper understanding of its physical mechanisms. Furthermore, thanks to the achieved tailored chiral responses, the direct CPL emission is obtained via coupling the chiral metasurface with QDs. Nowadays, CPL has been widely used in chemical and biological industries, however its generation still relies on the conversion from linear polarized light, which not only requires expensive waveplate setup, but also bring in energy loses during the process. Therefore, the hybrid system demonstrated in this thesis for directly CPL emission is very significant for providing a feasible way to address these problems and shed light for the future studies.

Part I: Enhanced circular dichroism from a chiral metasurface with apexes

In chapter 3, the role of apexes in a chiral metasurface is demonstrated and the idea of super chiral hot spots is also introduced. This proof-of-principle study, indicates that chiral metasurface with apexes permit to highly concentrate the near field of optical chirality, leading to very high circular dichroism. This work experimentally demonstrates a 4-fold enhancement of the circular dichroism and achieve a record high ~15 degrees of the optical activity for planar designs. The results highlight the

importance of apexes on both the near- and far-field metasurfaces' chiral, and demonstrates how ultrasensitive enantiomeric sensing may benefit from super chiral hot spots thus providing a new tool for chiral nanostructures with apexes inserted by-design.

Part II: Controllable circular dichroism induced by coupling localized and propagating modes

In chapter 4, a novel chiral metasurface, made of an array of nanoslits milled in a ~100nm thin gold layer on a sapphire substrate has been studied, that exhibits pronounced intrinsic chiral optical resonant responses (~4 degrees of CD) and narrow linewidth (~36nm) from visible to near IR frequencies which, thanks to the effect of surface lattice resonances introduced by a propagating mode, are finely controllable by the tuning of both the lattice period and the length of nanoslits. The results clearly highlight the impact of the propagating surface plasmon modes in controlling chiral responses in metamaterials and metasurface and provide a new kind of large and controllable chiral platform for applications. Furthermore, when compared to chiral patterns made of isolated metallic nanoparticles, this metasurface, etched in a continuous metal film, allows electrical conductivity across the film, thus enabling applications for optoelectric devices as well.

Part III: **Enhanced circular dichroism and circular polarized emission via the coupling between the chiral metasurfaces and colloidal QDs**

Functionalization of quantum dots (QDs) to induce circular dichroism and direct emission of circularly polarized light has been subject of intensive studies, not only because of obvious practical applications, but also to gain a deeper understanding of quantum semiconductor heterostructures. In chapter 5, plasmonic chiral metasurfaces, controllable by design, are combined with achiral CdSe/ZnS quantum dots, which induces remarkable chiral features in the latter: not only giant enhanced circular dichroism, but also a high degree of the circular polarization in the light emitted by the QDs hybridized with the chiral metasurfaces is observed. By probing the response of QDs combined with tunable chiral metasurfaces, it indicates that the induced chiral features are closely linked to the correlation between the QDs absorption bands and the chiral bands of the metasurfaces. These findings indicate that plasmonic chiral metasurfaces could play an important role in reshaping QDs with useful chiral properties.

Chapter 2. Experimental Techniques

2.1 Nanofabrication technique

As the main interest in this thesis, optical chiral metasurfaces, which consist of metamolecules with the features' size on the nanoscale level, can generally be manufactured by two methods, top-down[89] and bottom-up[90]. Bottom–up nanofabrication methods, including atomic layer deposition[91], molecular self-assembly[92], and DNA-scaffolding[93] have been widely utilized to generate multi-functional nanostructures, for example, Kuzyk Anton, *et al.* has used DNA-scaffolding for producing chiral plasmonic nanostructures with tailored optical response[65]. Various techniques have been also employed for the top-down approach, such as direct laser writing (optical lithography), focus ion beam (FIB), and electron beam lithography (EBL), to cut, mill and shape materials into the desired shape and order. Optical lithography[94] is a dominant microfabrication technique in semiconductor industry, which employs ultraviolet (UV) or x-ray to expose on a so-called photoresist layer and the selective remove is enabled by the subsequent chemical development process. However, the limitation of optical lithography is obvious that its resolution can hardly meet the needs of the fabrication of optical metasurfaces.

Basically, the minimum feature size of these fabrication systems can be estimated by:

$$W = k_1 \cdot \frac{\lambda}{NA}$$

Where W represents the minimum feature size and k_1 is an encapsulating process-related factor and typically equals to 0.4. NA is the numerical aperture and λ is the wavelength of the light used. Considering the working wavelength of 193nm from excimer lasers, the resolution can only reach to around 50nm that is too big to fabricate the subwavelength structures for visible range. Therefore, for a higher resolution, an obvious solution is shortening the working wavelength. FIB and EBL use particles instead of light for nanofabrication. These particles have much shorter wavelength, which vastly increases the fabrication resolution. For example, the de Broglie wavelength of electron used by EBL is 0.87nm. Recent years, with the developments of beam focusing and microscopic techniques, the deviation of the fabrications based on FIB and EBL can be controlled within several nanometers[95]. The bottom-up approach, in contrast, usually seeks to arrange small components into more complex assemblies.

In this thesis, all the fabrication work is carried out via the top-down approach, which will be introduced in detail in the following parts.

2.1.1 Focus ion beam fabrication

Since the early 1980s, Focus ion beam (FIB) technology has been widely used for various materials science applications[96-100] from circuit editing[101] to semiconductor research[102-104]. Modern FIB system normally consists of a versatile dual-beam platform,

including both the electron beam and ion beam. The FIB instrument (FEI Helios 650) shown in the figure 2.1a is the one used for fabricating the chiral metasurfaces demonstrated in this thesis. This dual beam system is displayed in figure 2.1b. In the vacuum chamber, both electron and Ga^+ ion beams are focused on the sample. Because the ion beams are unavoidable damaging the sample during the imaging due to the mass of the ions and their energy. Therefore, the ion beam is mainly used for the milling process, while the electron beam is mostly used for observing samples as a SEM function.

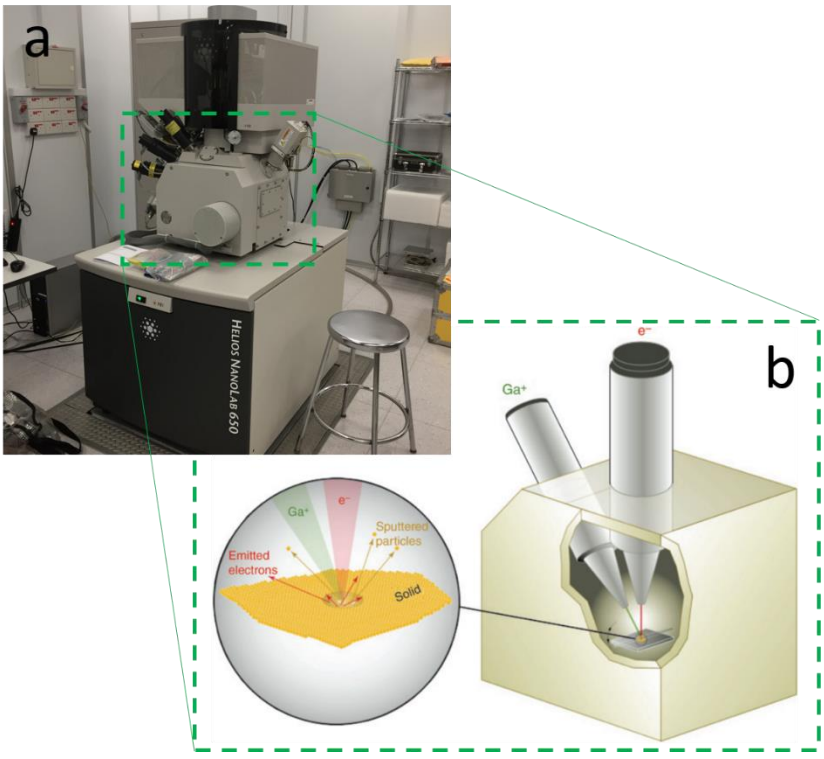

Figure 2.1. *The dual-beam system of the FIB instrument. (a)The FIB instrument located at CDPT (Center for Disruptive Photonic Technologies, NTU) cleanroom. (b)The schematic of the duel-beam system*[105].

The procedure of nanofabrication by FIB is displayed in figure 2.2. Firstly, the substrate is properly prepared after the standard cleaning process and next, the thermal evaporation technique is employed to deposit the thin film on the cleaned substrate. As a physical vapor deposition method, thermal evaporation technique enables ultra-precise control of the thickness of thin film, which greatly benefits the performances of the metasurfaces. The last step is to put the substrate with the thin film into the FIB chamber for the focusing and the final structure milling. Because the patterns are carried out via etching through the thin film, they are normally called 'negative'.

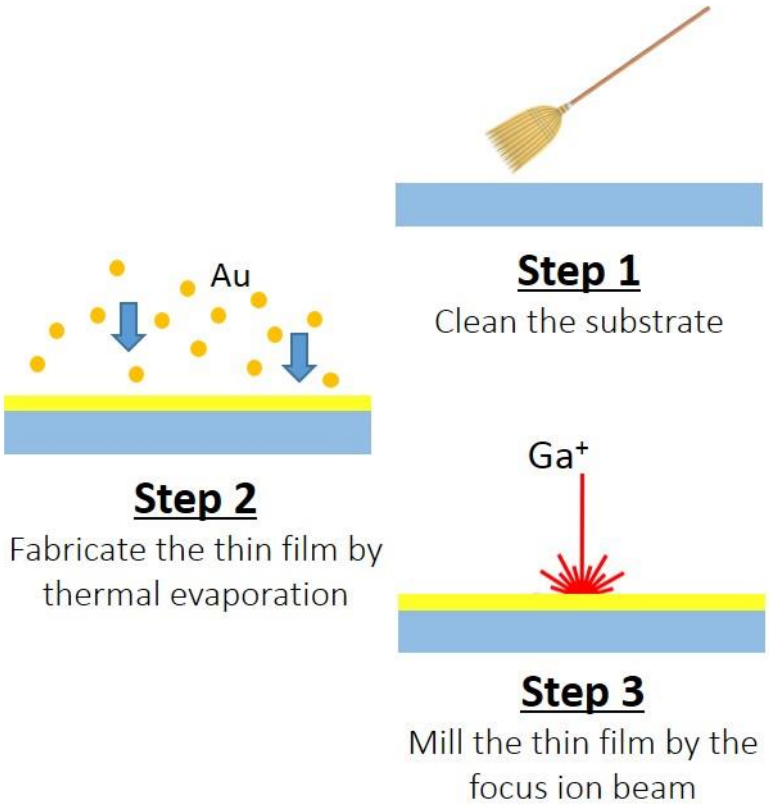

Figure 2.2. *The general process of fabricating the metasurfaces by FIB*

2.1.2 Electron-beam lithography (EBL)

Electron-beam lithography[106,107] (EBL) is another main top-down method for fabricating complex nanostructures. There are several main steps in processing EBL as shown in figure 2.3. After the first step of cleaning the substrate, an electron-sensitive film called a resist is spin-coated on the substrate surface with the wanted thickness that can be finely controlled by the settings of angular acceleration and final angular velocity of the spin. The next step is exposing a focused beam of electrons to draw custom shapes on the resist surface, which can alters the solubility of the resist layer, enabling selective removal of either the exposed or non-exposed regions of the resist by immersing it in a solvent (chemical developing). Then, the required materials, such as metals are deposited on the surface to fill the removal regions. The final nanostructures are subsequently obtained after the lift-off of the remaining resist layer by chemical development.

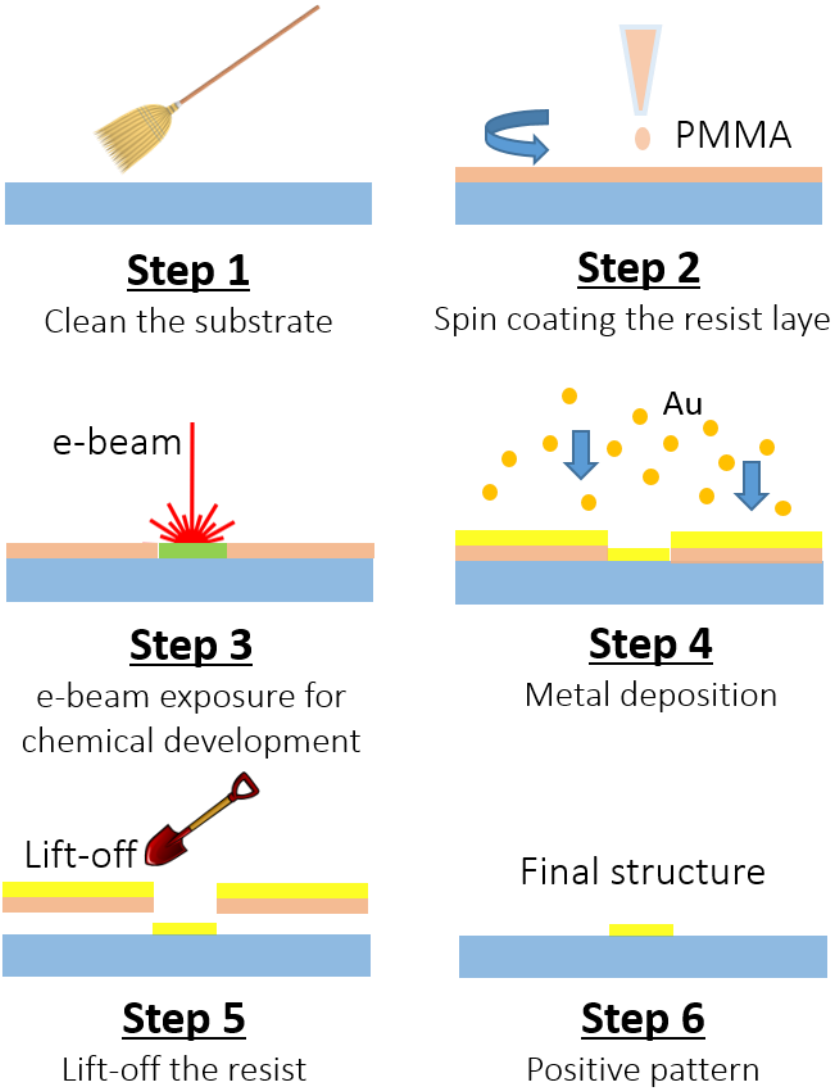

Figure 2.3. *The general process of fabricating the metasurfaces by EBL*

Compared to FIB, the resolution of EBL is not only determined by the beam focusing, but also highly influenced by the resist[108]. Therefore, it is more complex for EBL in the case of fabricating metasurfaces. In figure 2.4, Complementary chiral metasurfaces fabricated by FIB and EBL respectively, are displayed. It can be observed the pattern etched by FIB is composed of the arrays of nanoslits, thus it is also named negative pattern. On the contrary, the pattern made by EBL shown in figure 2.4b is

positive. Because the writing speed of e-beam is much faster than that of ion beam, EBL thus enable the manufacture for large area still with the high resolution, while it is very hard for FIB. In table 1, more detailed comparisons of the features between the EBL and FIB have been listed, which may permit readers to have a more straightforward understanding on the difference between the two techniques.

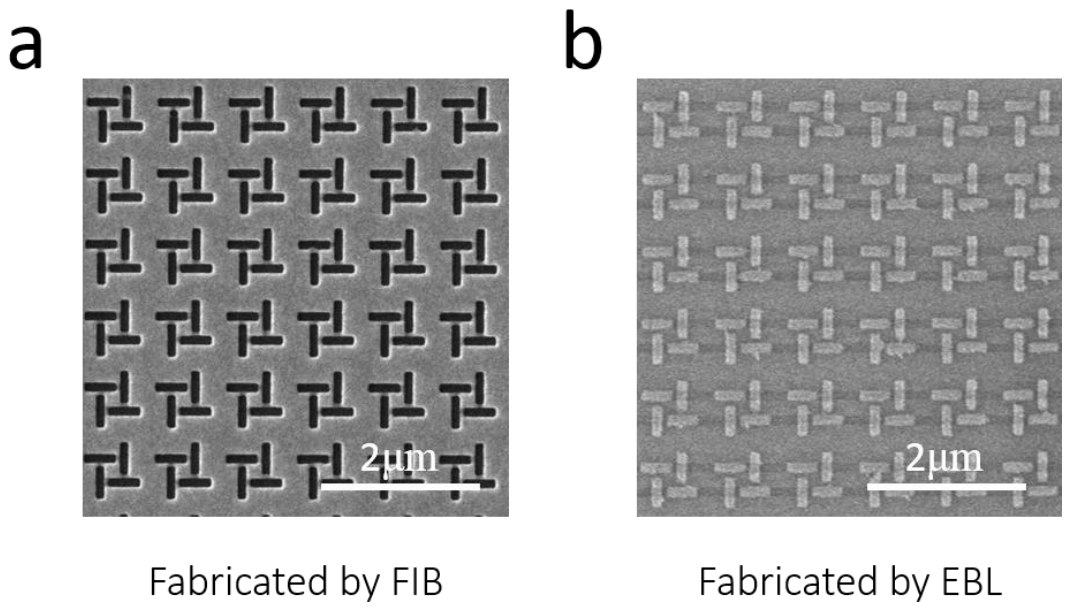

Figure 2.4. *Complementary chiral metasurfaces fabricated by (a) FIB and (b) EBL*

Features	EBL	FIB
Writing style	Direct writing	Direct writing
Writing source	Electron beam	Ga+ ion beam
Writing resolution	Sub-10nm	~5nm
Writing speed	Slow	Very slow
Scattering from the substrate	High	Low
Physical sputtering etching	Not available	Available
Chemical assisted etching	Available	Available
Extensive substrate damage	Slight	Severe

Table 1. *Comparisons of the main properties between the EBL and FIB*

2.2 Characterization techniques

In this part, the experimental methods employed to characterize the optical properties of proposed chiral metasurfaces will be introduced.

2.2.1 Circular Dichroism and Optical Activity

In order to obtain the CD and OA, the measurements of polarization-dependent transmittance of the proposed chiral metasurfaces are main experimental work. Due to the microscopic scale of the samples (around 50μm*50μm), a spectrophotometer that equipped with a microscope is needed for the characterization of their CD and OA. The one employed here is a commercial instrument from Jasco with the model of MSV-5200 that shown in figure 2.5a. This MSV-5200 includes a Peltier-cooled PbS detector with variable spectral bandwidth and the wavelength can be tuned from 200nm to 2700 nm. The figure 2.5b shows the 3D-stage and the objective of this instrument, which enables a clear aperture as small as 5μm. Due to the built-in automated Glan-Taylor polarizer system, this system provides linear polarized source with an optional automated linear polarization analyzer. In fact, this system is not designed for the measurements of CD spectra which are normally measured by specialized CD spectrophotometer. However, most commercial CD spectrophotometers are designed for measuring solutions or films which are mostly scaled in millimeter and bigger. Therefore, a conventional CD spectrophotometer without a built-in microscope can be hardly used to measure the optical chirality of a chiral metasurface.

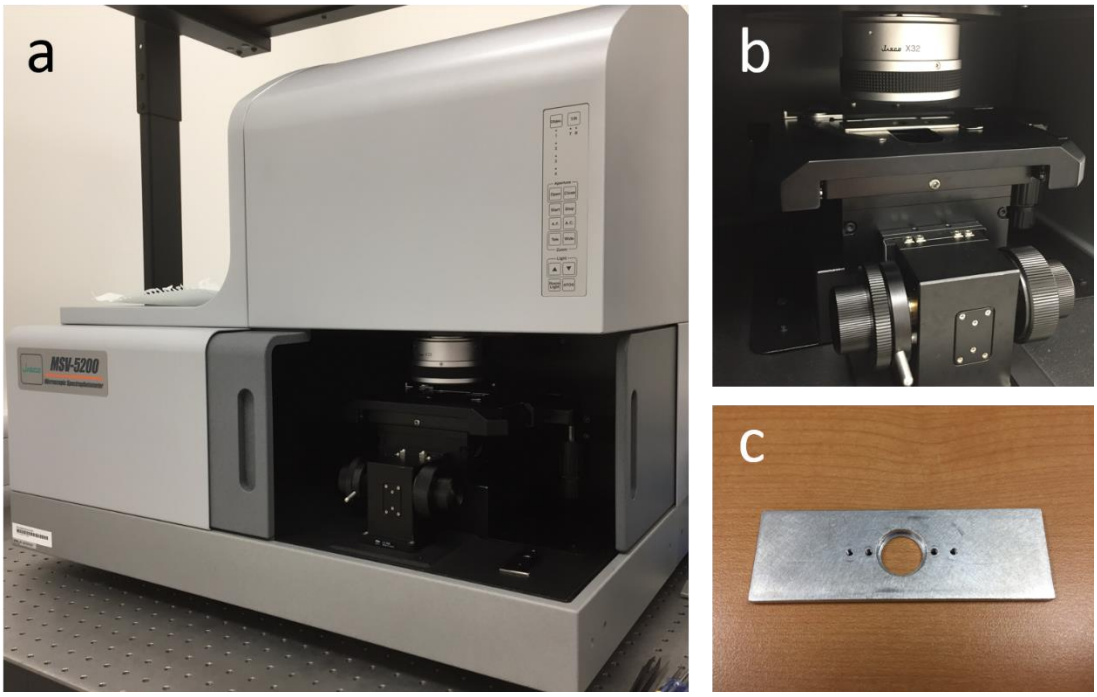

Figure 2.5. *The microspectrophotometer MSV-5200 located at CDPT. (a)The overview of the microspectrophotometer. (b)The 3D-stage and objective of the microspectrophotometer. (c)The home-made sample holder that designed to generate the CPL source*

In order to make the microspectrophotometer usable for CD measurements, the linear polarized source need to be converted to CPL, which means another quarter waveplate is needed in its optical path. For this purpose, one special sample holder displayed in the figure 2.5c was designed and manufactured. Considering the limited space between the 3D-stage and objective, the holder is designed to have the unmounted quarter waveplate with a half inch aperture inserted, which can convert the incident linear polarized light to CPL.

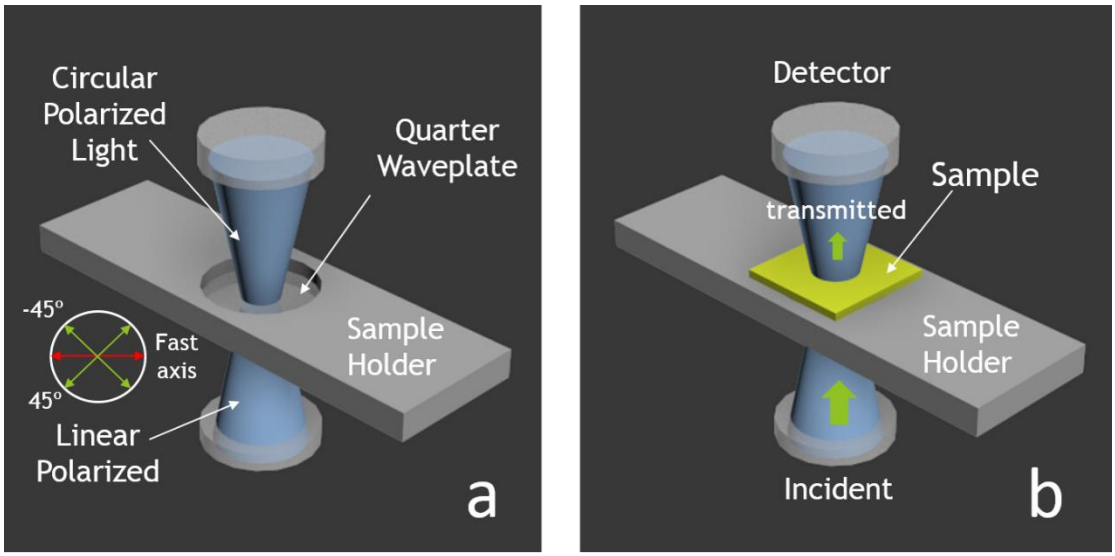

Figure 2.6. *The schematic of the microspectrophotometer to generate the CPL source by inserting the broadband quarter waveplate. (a)Converting the LPL to CPL. (b)The measurement of circular polarization-dependent transmittance*

As shown in the figure 2.6a, the fast axis of the achromatic quarter waveplate is set in the horizontal direction, and meanwhile, controlling the incident linear polarizations with 45 or -45 degree to it can generate both the circular polarizations. As a result, the CD can be obtained by the formula, $\tan\theta = \frac{\sqrt{T_{RCP}}-\sqrt{T_{LCP}}}{\sqrt{T_{RCP}}+\sqrt{T_{LCP}}}$ in which θ represents the ellipticity. The geometry of the simplified set-up is put in figure 2.6b. Besides the CPL, the angles of incident LPL can be also tuned for different elliptical states output for various usages. Figure 2.7 demonstrates the differential transmittance spectra of a 4-fold symmetry chiral pattern that proposed in chapter 4. It has mentioned before CPL can be obtained via controlling the incident linear polarizations with 45 or -45 degree to the fast axis of the quarter waveplate. If the angle is smaller than 45, such as 15 and -15 (see figure 2.7a), and then the output polarization will be ‘left’ and ‘right’

elliptically polarized light. Basically, for a 4-fold chiral pattern, maximum differential transmittance will be obtained by the excitation of CPL, which is understandable, because for the circular and elliptical polarizations with same intensity, the elliptical one can be still decomposed into CPL and LPL, while the latter is invalid to contribute to the differential transmittance, which results to the smaller overall signal. In figure 2.7b, the experimental results perfectly meet the theoretical expectations that the maximum differential transmittance was achieved by the excitation of left and right CPL and with the smaller angles of incident LPL, the differential transmittance decreased to almost zero when the incident angles of LPL are only 5 and -5 degree. These results completely indicate the system for measuring CD is well established.

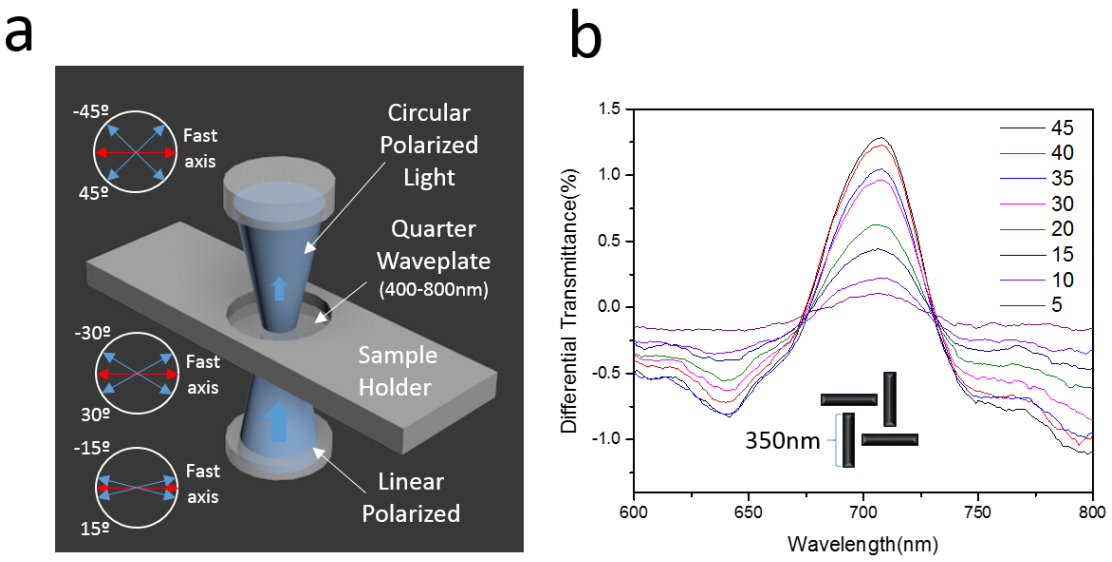

Figure 2.7*. Differential transmittance of a chiral metasurface excited by different elliptical polarized light. (a)The angles of incident LPL can tuned to generate from linear, elliptical to circular polarizations. (b)The differential spectra of the 4-fold*

symmetry chiral pattern excited by different elliptical states from less circular to completely circular polarization.

For the measurement of the OA, the built-in linear polarization analyzer is applied perpendicular to the incident polarization direction, and then the information of the transmittance can indicate the optical rotation of the sample.

2.2.2 Photoluminescence (PL) measurement

In this thesis, the exploration of the coupling between QDs and chiral metasurfaces is one of the main interests, which thus requires the PL measurements to reveal the reshaped properties of the QDs.

PL is a phenomenon where the specimen emits light due to the absorption of photons. For semiconductor, an exciton formed by a bonded electron-hole pair can be generated by absorbing a photon[109-111]. The relaxation of the excitation state is very complex. Some of the electron-hole pairs recombine and emit the photons with the lower energy. While, impurities of the material can also capture the pairs and form a series of transition[112,113] such as acceptor bound exciton (AX), donor bound exciton (DX). Moreover, the aforementioned transitions could also interact with the optical phonons and form series of replica transitions, equally spaced from their zero-order transition by quanta of optical-phonon energy. Via carefully collecting all these

transitions' signals and disperse them with fine gratings, information of the existence and ionization energy of the samples could be extract from the spectra non-destructively.

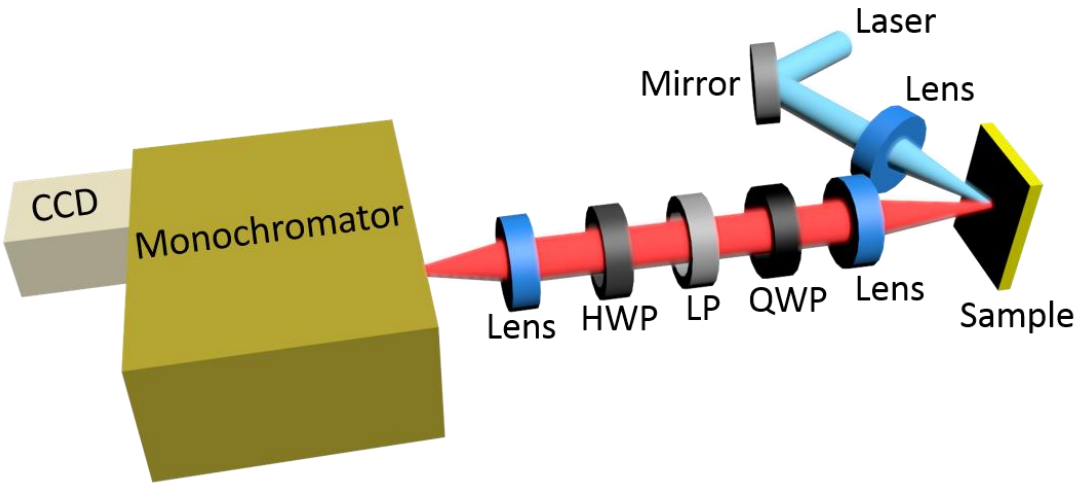

Figure 2.8. *The experimental setup for the PL measurement of the hybrid system*

In the case of characterize the coupling of QDs with chiral metasurfaces, the key point is to analyze the circular polarization component of the emission. For this purpose, the experimental set-up has been built and shown in figure 2.8. The continuous wave He-Cd laser delivering laser beam at optical wavelength of 442 nm was used as the excitation source. The laser power was set to be ~0.1 mW such that negligible quenching effect was observed. The laser beam was focused onto the sample by an objective with diameter of ~50 μm at an angle of ~45° to surface normal. The emission signal from the sample was collected in the forward direction and analyzed by a silicon-based charge coupled device equipped with an achromatic quarter wave plate (QWP, Thorlabs AQWP05M-600), a linear polarizer (LP, Thorlabs LPVISE200-A) and an achromatic half-wave plate. The achromatic quarter wave plate and the linear polarizer

were used to select the targeted circular polarized emission. Basically, the RCP (|R⟩) and LCP (|L⟩) waves can be respectively described in terms of Jones vectors as:

$$|\mathrm{R}\rangle = \frac{1}{\sqrt{2}}\begin{pmatrix}1\\-i\end{pmatrix}$$

$$|\mathrm{L}\rangle = \frac{1}{\sqrt{2}}\begin{pmatrix}1\\i\end{pmatrix}$$

In the two vectors above, the two components in a vector from top to bottom represent the wave oscillation in x and y, respectively, and the wave is propagating in the direction of z. The quarter waveplate with fast axis in horizontal can be also described by the Jones matirx as:

$$M_Q = e^{i\pi/4}\begin{pmatrix}1 & 0\\0 & i\end{pmatrix}$$

Considering EM wave can be completely described by the RCP and LCP, hence the output wave after the quarter waveplate can be calculated by:

$$L_R = e^{i\pi/4}\begin{pmatrix}1 & 0\\0 & i\end{pmatrix}\frac{1}{\sqrt{2}}\begin{pmatrix}1\\-i\end{pmatrix} = \frac{e^{i\pi/4}}{\sqrt{2}}\begin{pmatrix}1\\1\end{pmatrix}$$

$$L_L = e^{i\pi/4}\begin{pmatrix}1 & 0\\0 & i\end{pmatrix}\frac{1}{\sqrt{2}}\begin{pmatrix}1\\i\end{pmatrix} = \frac{e^{i\pi/4}}{\sqrt{2}}\begin{pmatrix}1\\-1\end{pmatrix}$$

Here, the calculated Jones vectors of L_R and L_L are orthogonal and corresponding to the linear polarizations of 45 and -45 degree, respectively. Therefore, the linear

polarizer can be further utilized to select either L_R or L_L, by which the emitting intensity of the original RCP and LCP can be obtained accordingly.

The half-wave plate was utilized to fix the polarization of the emission into the monochromator. It should emphasize that it is very important to make sure the emission measured by monochromator should be kept by the same polarization. Because the actual efficiency of the monochromator is polarization-dependent, therefore, different polarizations will introduce fake signals resulting unreliable data.

Chapter 3. Enhancing Circular Dichroism by Super Chiral Hot Spots from A Chiral Metasurface with Apexes

3.1 Introduction

For natural chiral molecules, the detection of the CD is still challenging because of the incredibly weak signal. The reason is believed that, in the traditional way of CD characterization, CPL as the probing tool is not 'twisted' enough to match the much smaller chiral structures of chiral molecules, which consequently causes the inherently weak chiral matter-light (CPL) interaction[7].

In recent years, the study of metamaterials with artificial chiral building blocks is trying to provide solutions[47,48,55,64,68,114-116]. Three dimensional chiral metamaterials[52,54-56,62,67,117,118] made by plasmonic materials have been proved the capacity of not only exhibiting tremendous enhanced chiral responses, but also manipulating the light spin modes. The realization of this kind of metamaterials would benefit various applications, such as ultrasensitive bio-detection[77], miniature circular polarizers[51], and quantum communications[119].

However, thanks to the structural complexity, the difficulty of fabrication is still a challenging issue despite several innovative fabrication methods are proposed recently[67,120], but the limitations of materials selection, spectral range of chiral optical

response still exist. Alternatively, two dimensional chiral metamaterials or metasurfaces[47,48,53,58,64,121-123] are deemed a feasible approach which does not rely on the 3D nature of chirality to perform the effect of circular dichroism. By manipulating the asymmetric finite non-radiative losses[58,61] or the cell-cell coupling[121-123] corresponding to different spin modes, pronounced chiral responses are observed from various careful designed chiral metasurfaces. Nevertheless, there are still very limited studies on the design methodology of chiral metasurfaces towards significant enhanced chiral effects.

Here I propose a chiral metasurface, composed of an array of achiral nanoholes milled by advanced focused ion beam (FIB) technique in an ultra-thin gold film. I demonstrate a straightforward design strategy that apexes can be readily formed in a metasurface by a slight overlap of the nanoholes. The optical chirality in the near-field is highly concentrated around the apexes due to chiral-like interference between the achiral nanoholes so as to generate the super chiral hot spots. Experimentally the designed structure well coincides with FIB milling technique, which greatly mediates the fabrication difficulty usually existent in other approaches. As a result, a remarkable ~4-fold enhancement of the circular dichroism has been achieved with the apexes added. A huge optical activity (OA) signal of ~15 degrees is observed experimentally. My results highlight the impact of apexes on enlarging the chiral response of metasurfaces by generating the super chiral hot spots, potentially shedding a light on the design of next generation chiral metamaterials.

3.2 Method

3.2.1 Nano-fabrication

First the 100nm Au film on glass substrate that is cleaned by standard procedure is prepared by thermal evaporation and then I fabricated the chiral metasurfaces a focus ion beam writer (FEI Helios 650) operated at 30 kV and 12pA.

3.2.2 Experimental characterizations

A commercial micro-spectrophotometer (Jasco MSV5200) has been used to measure the normal incident transmittance of the metasurfaces under the luminance of left and right circular polarized light to quantify CD. The source of CPL is converted from the linear polarized light by inserting quarter waveplates into the optical system. Both the in and out aperture of the measurements is set as 50um that just fits the area of the metasurface array. All the baselines are obtained by measuring the clean glass substrate. The OA was measured by the same facility (MSV5200) utilizing the combination of linear incident light and analyzers that was set parallel and perpendicular respectively corresponding to the polarized direction of incident light to determine the rotatory.

3.2.3 Numerical simulation

I utilized the software Lumerical FDTD solutions to numerically study the chiral metasurface which is modeled in the X-Y plane. Bloch boundary condition is set in the X, Y directions due to the periodic nature and perfectly matched layer (PML) boundary

is for Z direction. I apply a frequency domain power monitor to obtain the data of transmittance and a frequency domain profile monitor for the data of electromagnetic distribution. The optical chirality is calculated in the built-in script workspace in this software based on the electromagnetic data monitored in the abovementioned frequency domain profile monitor. The mesh accuracy level in this FDTD model is set as 7 which corresponds to very high accuracy. I use the Palik database to define the reflective index of glass substrate and Au film. The convergence of all the simulations is around the order of 10e-5.

3.3 Results and discussions

Sharp plasmonic structures[124] in nano materials has been widely studied and utilized to confine and enhance the near-field intensity, such as the plasmonic bowtie antenna[125,126]. The reason in this work I choose nanohole as the basic unit is because by controlling the distance between the nanoholes, the apexes are easily created and removed without altering the rotatory feature of the chiral pattern. As a result, the systematic study based on the impact of the apex can be demonstrated clearly.

As shown in Figure 3.1, the chiral metamolecule is formed by 7 achiral nanoholes of identical diameter $a=200$ nm, separated by a gap g that can span from positive (Fig. 1a) to negative (Fig. 3.1b) values: as a whole, this pattern resembles a rotated letter ‘Z’ with an angle of 60 degrees between the adjacent arms and possesses intrinsic chirality due to the breaking of in-plain mirror symmetry. The chiral cells are arranged in a

square lattice array with a period *p*. Figures 3.1c and 3.1d show scanning electron microscope (SEM) images of the chiral metasurface, for values of the gap *g* of respectively *g*~20nm (no overlap) and *g*~-20nm (overlap), milled in ~100nm thin gold film on a glass substrate that indicated in the figure 3.1e.

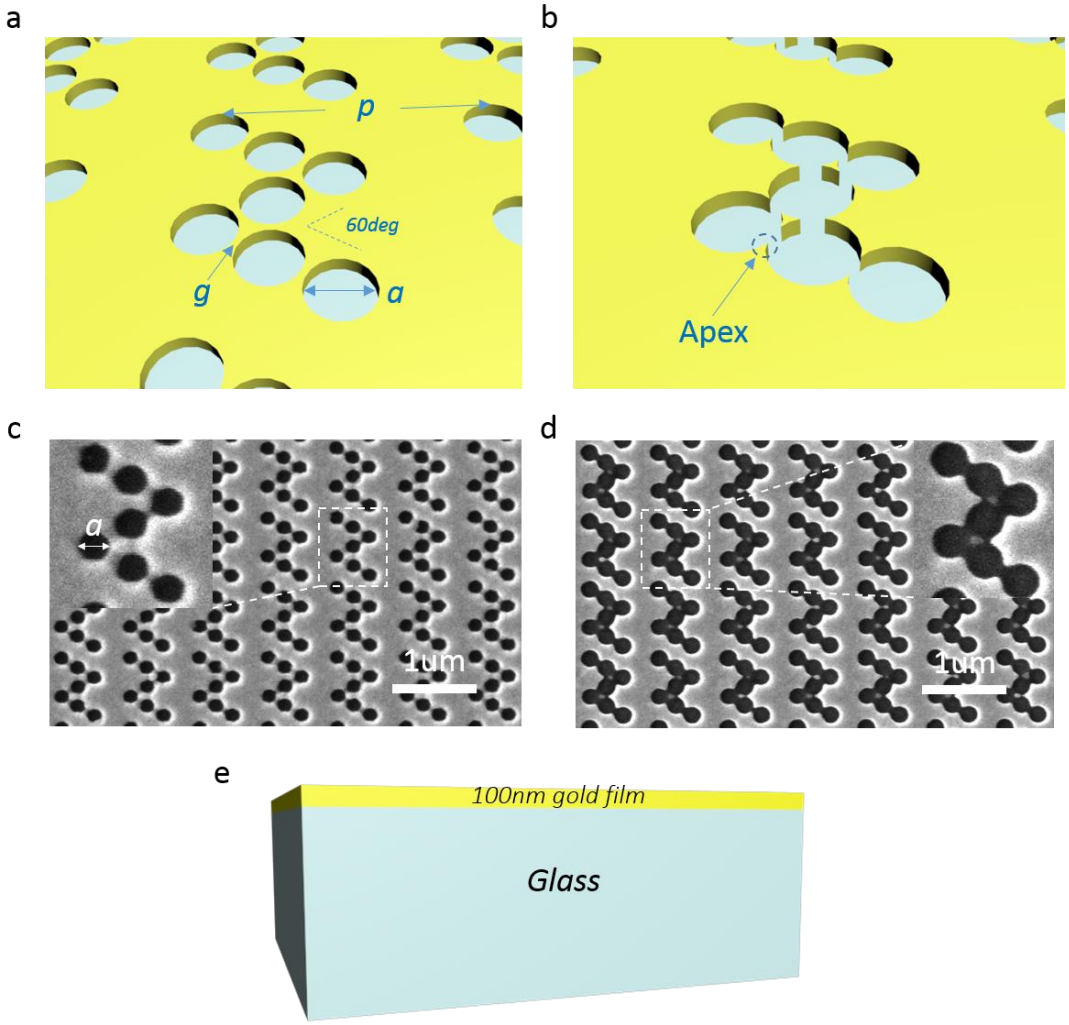

Figure 3.1. *Schematic illustration of the investigated chiral metasurface (a) without and (b) with the overlapping among the milled nanoholes and (c) (d) the corresponding SEM images. (e) The cross-section of the chiral metasurface.*

In order to investigate the resonant modes of chiral responses, I perform full-wave numerical simulations for three chiral patterns of varying gap size between the nanoholes: g = 20nm (non-overlap nanoholes), g = 0nm (touching nanoholes) and g = -20nm (overlapping nanoholes). In the simulation, the chiral metasurfaces are excited in normal direction and the spectra of the circular dichroism (CD) that shown in figure 3.2a, are calculated by the differential transmittance between the left and right circular polarized light. Huge chiral optical responses are indicated from the results in which the peak of black curve corresponding to the g = -20nm exceeds 10 percent.

More importantly, from the red curve to the black one, it shows an apparent trend that the chiral optical responses increase dramatically, which just matches the appearance of the apexes with the gaps getting vanishing. It also can be noted that the curves manifest red shift, which is understandable: with the smaller gaps, the distances between the chiral unit cells become bigger with a constant period so that the collective effects governed by the interference among the cells are shifted to red.

In order to achieve a clearer understanding, the electric field distribution at resonant is mapped corresponding to excitations by left (LCP) and right (RCP) circular polarized light in Figure 3.2 from b to g. First, comparing the left panel (Figure 3.2b, d, f) with the right (Figure 3.2c, e, g): the distributions of the hot spots related to the enhancement of the electric field show a clear dependence on the polarization of the incident light, which evidently accounts for the dramatic asymmetric transmittance of RCP and LCP illustrated in Figure 3.2a. Second, with the apexes generated, it can be

observed the intensity of the electric hot spots located at the apexes' area is highly enhanced with the ratio nearly one order, which although is not surprising about the degree of enhancement, however it is significant to simply link this electric field enhancement to chiral responses.

Because compared with design guidelines, like helix matching from previous studies[127], it is more straightforward and practical to achieve larger chiral responses through rising the near field intensity. In order to explicit understand the physical mechanism behind, we can simply refer to the formula which describing the non-radiative (Ohmic) losses: $P_{abs} = \frac{1}{2}\omega\varepsilon''|E|^2$, where the angular frequency ω and imaginary part of the permittivity ε'' are constant. Obviously, when the electric field intensity $|E|$ dramatic increases with the apex generated, as shown Figure 2b-g, the asymmetric non-radiative (Ohmic) losses will become much larger because of the circular polarization dependent electric distribution, as a result, the metasurfaces with apexes show enhanced chiral responses.

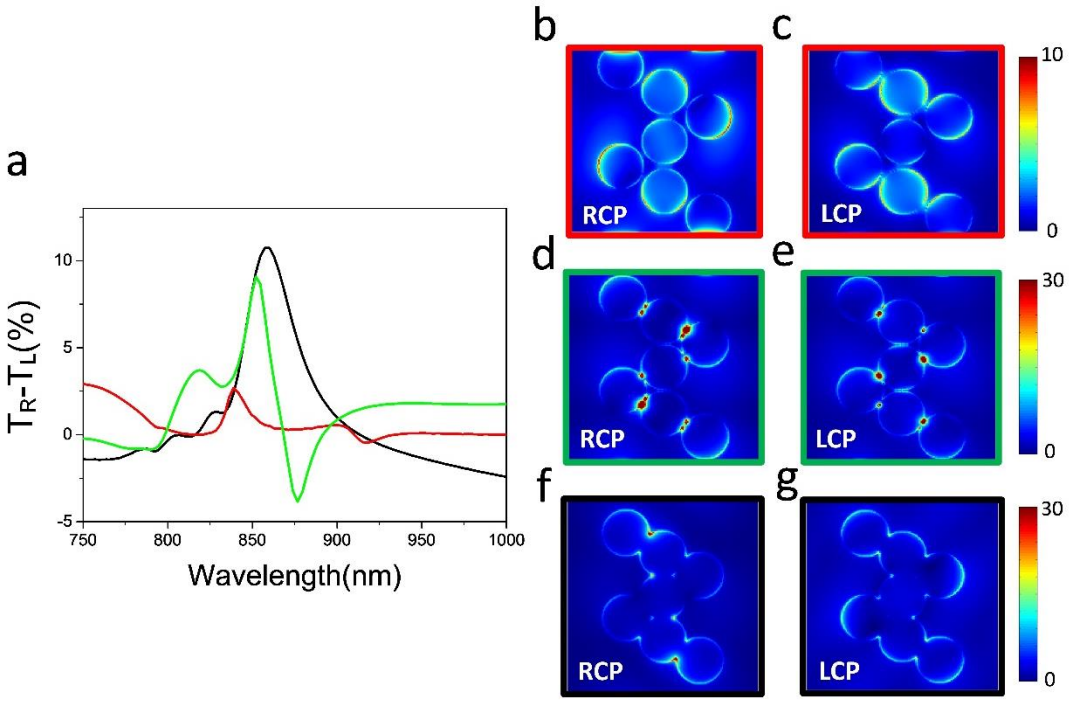

Figure 3.2. *(a) The transmitted circular dichroism, corresponding to the gap distances of 20nm (red curve), 0 (green curve), -20nm (black curve), from the simulations shows the trend of increasing when the apexes are generated. The stimulated electric field distribution maps at the resonant wavelengths excited by right (RCP) and left (LCP) circular polarized light for the chiral patterns with identical lattice period 800nm but various gap distances of g=20nm(b, c), 0(d, e), -20nm(f, g), respectively.*

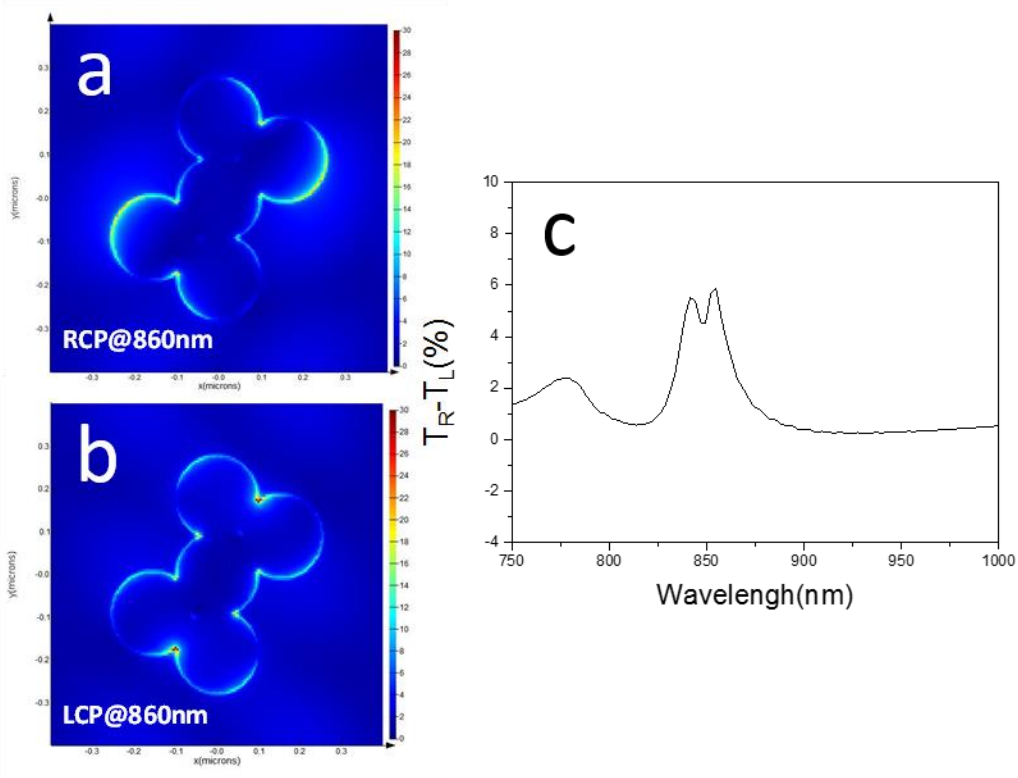

Figure 3.3. *The CD responses of the 5-hole pattern with apexes. (a) The stimulated electric field distribution excited by RCP at the wavelength of 860nm. (b) The stimulated electric field distribution excited by LCP at the wavelength of 860nm. (c) CD spectrum of the 5-hole pattern.*

In order to make sure the 7-hole design is optimal, the 5-hole pattern with the same overlapping distance of 20nm has been also studied by the numerical method. Figure 3.3 illustrates the results that the 5-hole pattern also shows the chiral responses while the CD of 6% (FIG.3.3c) is obvious smaller than the 12% shown in the 7-hole pattern. Therefore, the 7-hole pattern is chose for the next-step investigations.

To further elaborate the relationship between the enhanced electric field and chiral responses, I quantitatively introduce the optical chirality *C*, a time-even pseudoscalar which is used to describe the spiral level of electromagnetic field[7,76,78]: $C = -\frac{\varepsilon_0 \omega}{2} \mathrm{Im}[\boldsymbol{E}^* \cdot \boldsymbol{B}]$, where the $\boldsymbol{E}$ and $\boldsymbol{B}$ denote the complex amplitudes of electric and magnetic field, respectively. In contrast to the circular polarized light, chiral metamaterials enable several orders higher optical chirality in the near field[72,127,128], which in the other hand contributes to the far field effects of tremendous circular dichroism or optical activity.

Base on the results reported in the Figure 3.2, I in further calculate the near-field optical chirality for my chiral metasurfaces with and without apexes and that is illustrated in Figure 3.4. Compared with the relatively weak chiral hot spots without overlapping nanoholes in Figure 3.4a, the optical chiral field shown in Figure 3.4b, c is highly enhanced and concentrated, especially at the positions around the apexes, which could be explained by the asymmetric interference among the unit cells. Because besides the localized mode, the propagating mode that have been reported[121,122] play a crucial role especially for the milled chiral metasurfaces through the cell-cell interference, constructively or destructively, contributing to the collective chiral responses. Therefore it is understandable the apexes, compared with smooth boundary more likely become a super chiral hot spot when the condition of interference is satisfied. From this, it can be concluded overlapping the nanoholes for the apexes generated in the chiral metasurfaces not only benefits the electric field enhancement in

the near-field, but meanwhile lifts the intensity of optical chirality so as to reinforce the optical chiral responses in the far field.

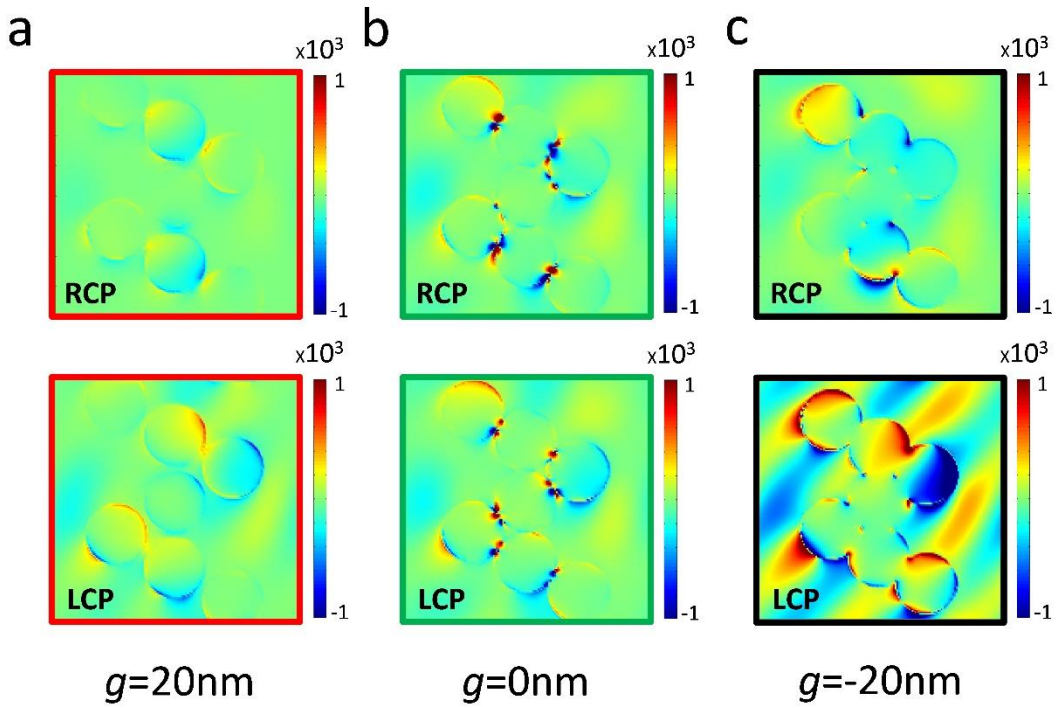

Figure 3.4. *The stimulated optical chirality field distribution maps at the resonant wavelengths excited by left (LCP) and left (RCP) circular polarized light for the chiral patterns with identical lattice period 800nm but various gap distances of g=20nm(a), 0(b), -20nm(c), respectively.*

I verified my proposed design strategy by experimental measurements on two 50μm x 50 μm array samples fabricated by focused ion beam milling on a 100nm thin gold sample deposited over a glass substrate. I selectively fabricated the patterns with gaps of 20nm and -20nm to illustrate the impact of the apexes on the chiral responses, while the touching holes with zero gap is left out, due to the extreme degree of difficulty

in fabrication. I determined the CD spectra by measuring normal incidence transmittance of both left and right circular polarized light using a commercial microspectrophotometer (Jasco MSV-5200) coupled with broadband quarter waveplate: the CD signal was deduced in terms of the ellipticity θ by the expression: $\tan\theta = \frac{\sqrt{T_{RCP}}-\sqrt{T_{LCP}}}{\sqrt{T_{RCP}}+\sqrt{T_{LCP}}}$. The numerical and experimental results displayed in Figure 3.5 show remarkable agreement, within the fabrication accuracy, they both display a 4-fold enhancement. Furthermore, the black curve in Figure 3.5b, reaches an outstanding CD peak value of 2.1 degrees that becomes comparable to the chiral responses of three dimensional chiral metamaterials[5,54,129].

The blue shift of the experimental results corresponding to the simulation results could be explained by the fabrication inaccuracy. It is understandable the actual diameter of nanoholes because of the ion etching effect will be slightly larger than that in simulations, which is equivalent to decrease the distances between the chiral metamolecules, thus resulting in the blue shift of the collective chiral responses in experiments.

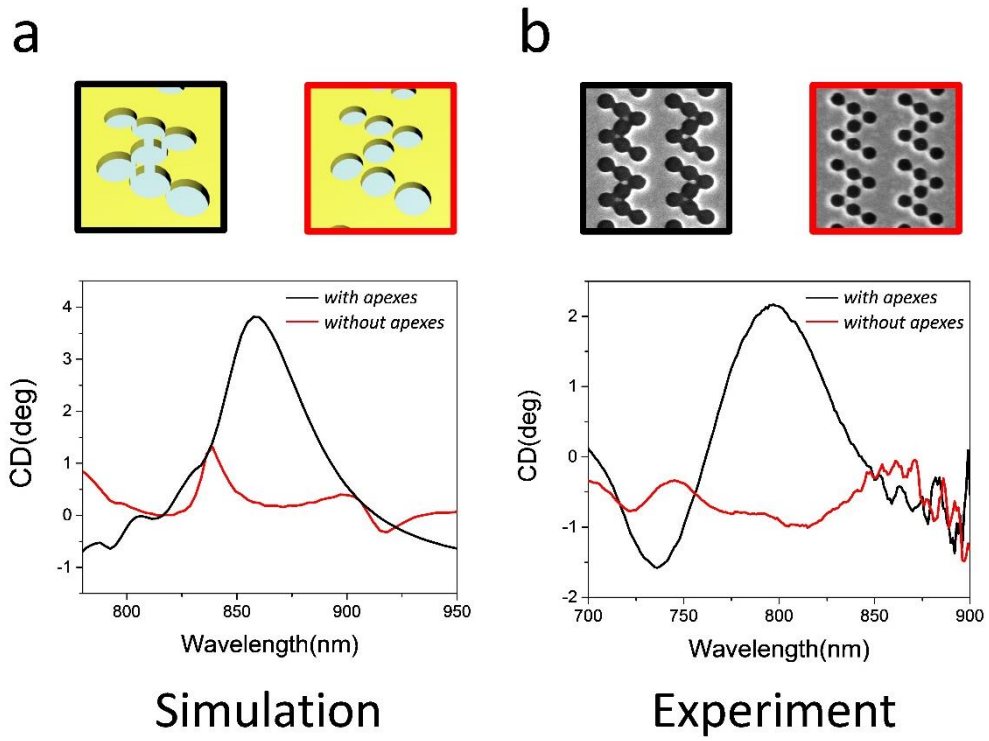

Figure 3.5. *(a) Simulated and (b) experimental circular dichroism spectra corresponding to the chiral metasurfaces with (black curve) or without (red curve) apexes*

Finally I investigate the role of asymmetric interference generated by the above-mentioned propagating mode, which allows an easy spectral tuning of the chiral hot spots resonance wavelength by altering the lattice period: this resembles a cavity modifying the interference between the chiral metamolecules. Experimentally, I fabricated chiral metasurfaces with overlapping nanoholes of various periods (p=770nm, 800nm and 830nm) but identical unit cell and measured both their optical activity and circular dichroism spectra, as shown in Figure 3.6. The peaks of both OA and CD spectra are significantly red-shifted proportionally to the increment of the

period, which visibly confirms the modulation of the propagating mode on the super chiral hot spots. Moreover, for a period of 830nm, the OA spectrum reaches a peak value of 15 degrees which makes the proposed chiral metasurfaces suitable for applications in ultra-compact optical rotators.

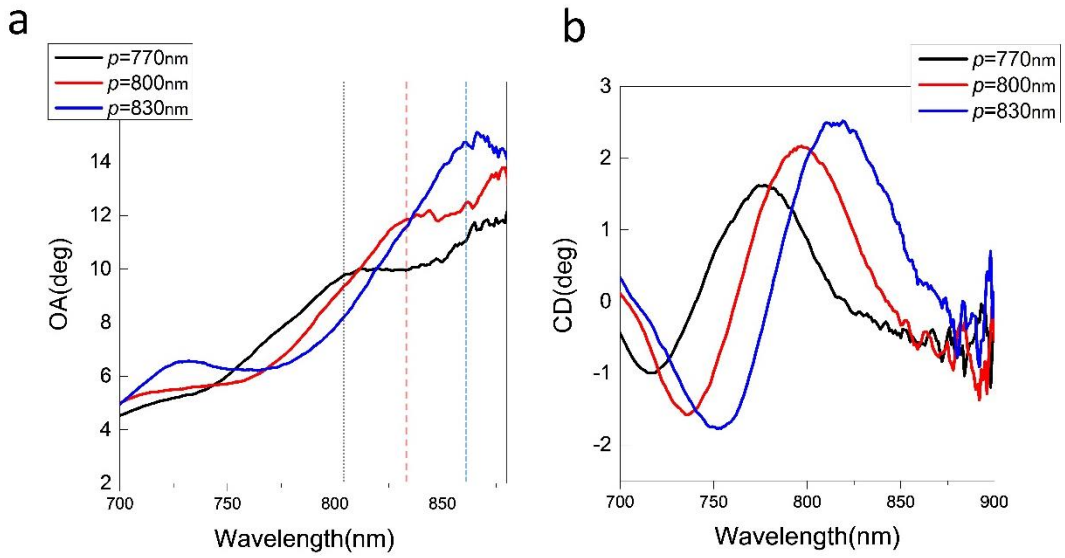

Figure 3.6. *Experimental optical activity spectra (a) and circular dichroism spectra (b) corresponding to the chiral metasurfaces with identical unit cell but various periods.*

3.4 Conclusion

In conclusion, I have proposed a chiral metasurface composed of achiral nanoholes which allow to create apexes in the nanostructured design and have investigated the impact of the apexes on the metamaterial chiral response. I found that the chiral metasurface with apexes give a greatly enhanced optical chiral responses. I demonstrated that the presence of the apexes highly enhances and concentrates the intensity of both electric field and optical chirality in the near field and reported a 15

degree optical activity and large circular dichroism in planar metasurfaces. These super chiral hot spots allow more efficient chiral-matter interactions which could potentially benefit in various applications. I suggest that the inclusion of apexes in metamaterial designs could prove as a practical strategy to enhance their chiral optical responses and should be investigated further.

Chapter 4. Controllable Circular Dichroism from a Novel Chiral Metasurface by Coupling Localized and Propagating Modes

4.1 Introduction

The advantages of chiral metasurface, compared with the 3D species are obvious that it is much easier to fabricate and moreover, because of its planar property, it is more suitable for ultra-compact integration in a minimized optical system. The exploration on chiral metasurfaces ranging from the initial famous gammadion shape meta-atom[48,68] to split-rings[57,130,131], fish-shapes[49], L-shape[64], and achiral oriented structures[63,115,121], have covered the wave frequencies from visible to gigahertz(GHz)[132]. As the highly promising platform for chiral molecule sensing[7,78], the chiral metasurface requires to locate their pronounced chiral response in the frequency range of UV to near IR, which could enable the resonant coupling with chiral molecules.

However, the challenge is that for the existing 2D chiral structures designed for the visible or near-IR range, their chiral responses are relatively weak that may be not strong enough for the abovementioned coupling. Some with pronounced chiral responses but require strict oblique incident angles, which highly limits the practical usage. From another aspect of physical understanding, most previous studies linked the enhanced mechanism of the chiral responses only to localized surface plasmon

resonance (localize mode), which not only is a limitation for deeper physical understanding, but also loses a degree of freedom to control the chiral responses by the surface plasmon polaritons. Consequently, the chiral responses shown in previous works were mostly spectrally fixed, which severely limits the practical applications.

Herein, a novel controllable chiral metasurface is demonstrated, which is simply composed of nanoslit array etched from the gold ultrathin-film with the thickness of ~100nm. This chiral metasurface not only experimentally exhibits pronounced chiral optical responses from visible to near IR frequencies. More importantly, based on the effect of surface lattice resonances[133,134] introduced by the propagating mode, finely tunable chiral resonances are observed and achieved. Moreover, the tuning of the propagating mode is innovatively combined with the localized mode by tuning the length of nanoslits, which further enlarges the range of tunability. Furthermore, compared with the most existing chiral patterns formed by isolated metallic nanoparticles, my etched continuous structure allows for functions of both chirality and conductivity, thus enables direct application for optoelectric devices.

4.2 Method

4.2.1 Nano-fabrication

The fabrication work was completed by a three-step process. Firstly, the double polished sapphire substrate was prepared and cleaned. Secondly, 100 nm gold film was coated on sapphire substrate by thermal evaporation. Lastly, a focus ion beam writer

(FEI Helios 650) operated at 30 kV and 7.7 pA was used to etch the gold thin film for the chiral nanostructures.

4.2.2 Experimental characterizations

The chiral metasurface was measured under normal illumination by the abovementioned micro-spectrophotometer (Jasco MSV-5200) coupled with boardband quarter waveplates (Thorlabs). A home-made sample holder into which quarter waveplates can be inserted is employed in this system. I keep the fast axis in horizontal orientation as shown in Figure 2.6 in chapter 2 and set the incident light with linear polarization, while at 45 or -45 degrees, relative to the fast axis direction of the inserted quarter waveplate. Accordingly, left and right circular polarized light can be generated from the linear polarizations after the quarter waveplate and then go through the sample. The baselines were obtained by measuring the clean sapphire substrate under the identical optical settings of the measurements of chiral structures.

4.2.3 Numerical simulation

All the simulation work was completed by the software FDTD Solutions. The reflective index of sapphire substrate (Al_2O_3) and Au film was from Palik based on the built-in database of the software. In the X and Y directions, I use Bloch boundary condition because of the periodic property of the metasurface, while for the Z direction, perfectly matched layer (PML) boundary was employed. The mesh size of (5 nm, 5 nm, 5 nm) was applied for the structure of metasurface.

4.3 Results and discussions

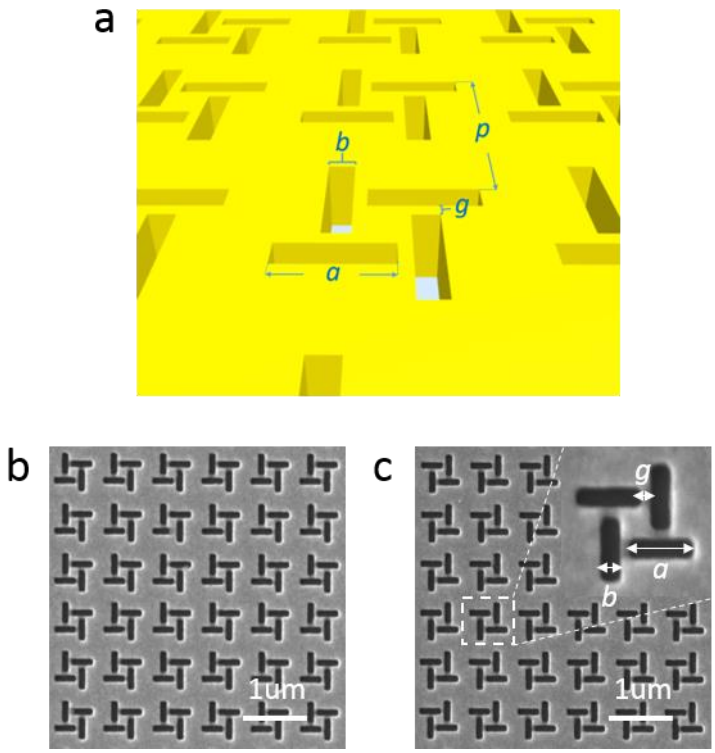

Figure 4.1. *(a) Schematic illustration of the chiral metasurface. (b) SEM images of left-handed chiral metasurface. (c) SEM images of right-handed chiral metasurface.*

The proposed chiral pattern is displayed in Figure 4.1 that a square lattice metasurface array with unit lattice period of *p*. It can be noticed in the figure 4.1a each metamolecule is formed by 4 nanoslits of identical length *a* and width *b* separated by a gap *g*. In further, each nanoslit rotates a 90 degree respecting to the preceding one and is aligned with its long axis to the center of the following one, in either clockwise or anticlockwise rotation, which determines the handedness of this chiral arrangement. Figures 4.1b and 4.1c show SEM images over a magnified area of a 40*40 μm^2 metasurface array (50*50 unit cells). The 2 samples displayed are designed with

identical parameters but with converse handedness (a=350 nm, b=100 nm, g=50 nm, p=810 nm) which are supposed to show the mirror image CD spectra. The nanofabrication is completed via etching the gold thin film by focus ion beam (FIB). Moreover, in order to reveal the influence of the propagating mode, the arrays with the identical unit cell with the same handedness but different lattice constant are also experimentally prepared.

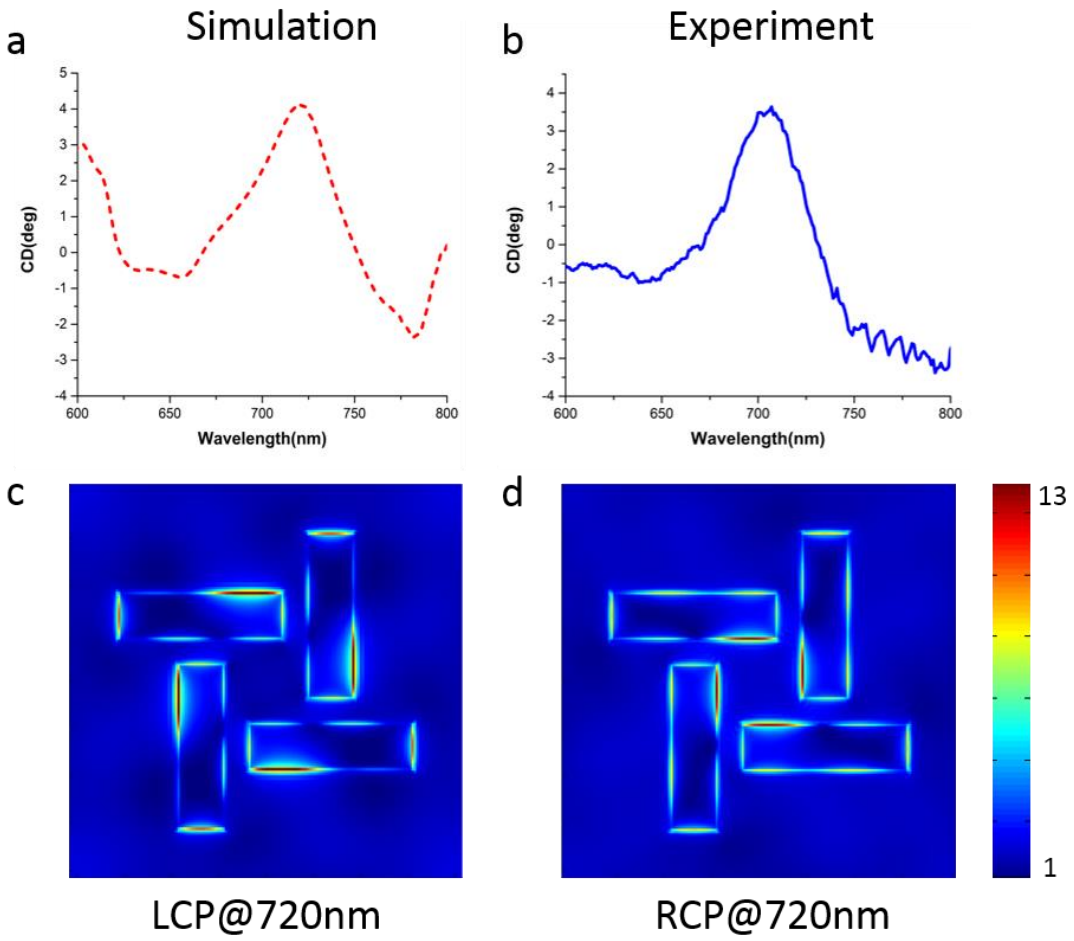

Figure 4.2. *Stimulated and measured chiral optical responses of the proposed metasurface. (a) The FDTD simulation results of the CD spectra of the chiral metasurface. (b) The experimental CD spectra measured by optimized micro-*

spectrophotometer. (c) Electric field intensity maps of the metasurface under left and (d) right circularly polarized illumination, at the resonant wavelength (720 nm).

Based on the resonant profile of single nano-slit, the chiral configuration makes the overlapping of E-field and H-field hot spots could occur around the 4 gaps[7,53], which means the coupling between the adjacent single nano-slits in one unit cell could contribute to the enhancement of optical chiral response by the localized mode. In order to investigate the chiral features, full-wave numerical simulation was carried out for the left-handed pattern (a=350nm, b=100nm, g=50nm, p=810nm), and the results are shown in the figure 4.2. Firstly, it can be observed in the figure 4.2a that a CD spectrum with a strong peak approaching to 4 degree that located around 720nm theoretically indicates the pronounced chiral responses possessed by the proposed chiral metasurface. Secondly, by comparing the experimental results that shown in the figure 4.2b with the simulations, a perfect agreement has been made which ensures the chiral ability of the chiral metasurface. Notably, considering the nanoslits' length of 350nm, the CD peck is approximately located at the wavelength of two-fold of the length, which just fits the fundamental localized plasmon resonance of nanoslits[53,135]. This indicates that the chiral responses from the chiral metasurface are highly linked to the excitation state of the single nanoslits which under the excitations in further interact with each other in the chiral arrangements for the output of chiral effects.

For a clear physical insight, based on the respective excitations by left and right CPL, the electric field distribution on the metasurface was mapped, which are displayed

in the figure 4.2c, d. It can be clearly seen that the same chiral pattern shows obvious circular polarization dependent distribution of the enhanced electric field, which leads to the significant chiral optical responses.

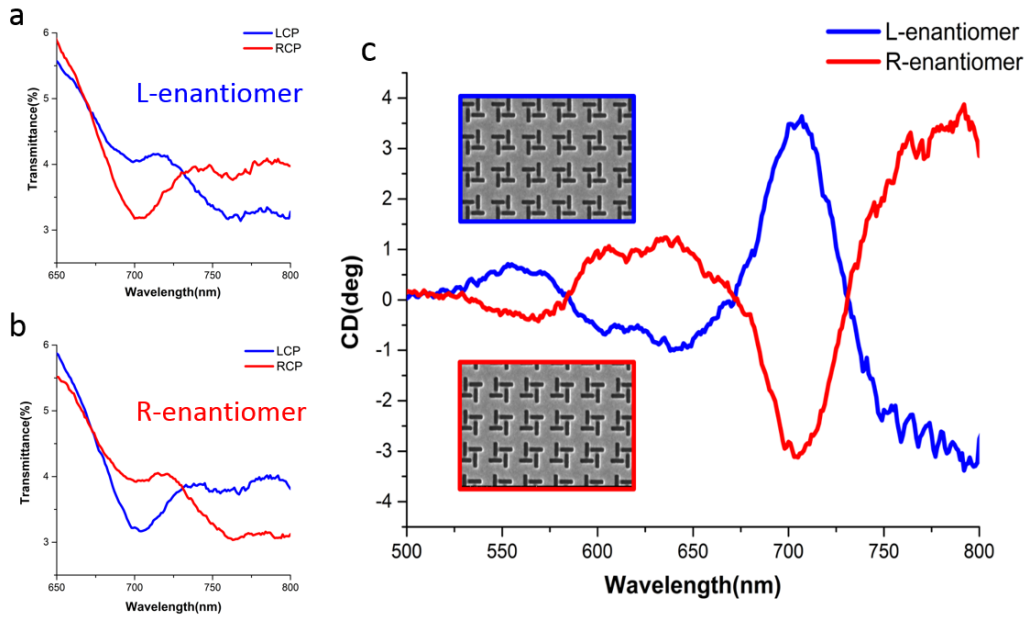

Figure 4.3. *The mirror image is obtained experimentally by the CD spectra of the left and right handed chiral metasurface. (a) The absolute transmittance spectra corresponds to left (blue curve) and right (red curve) circular polarized illumination of the left-handed and (b) right-handed enantiomer metasurface. (c) The CD spectra transferred from the transmitted spectra of the both handed metasurface, which form a perfect mirror image.*

To confirm the chiral nature of the proposed metasurface, I carry out Circular Dichroism (CD) measurements for both enantiomers. Figures 4.3a and 4.3b show transmittance spectra for left and right enantiomers respectively, where clear

differences can be observed in the transmittance spectra of LCP (blue curve) and RCP (red curve) together with a complementary behavior for the two handedness. The CD spectra, which can be retrieved by the transmittance by using the formula θ (deg) = 33(log(T_{LCP}) – log(T_{RCP})), are reported in Figure 4.3c for both enantiomers: they are almost perfect mirror images and exhibits a huge ellipticity of nearly 4 degrees at 703 nm which is comparable with the chirality strength given by more elaborate three dimensional structures that require far more complex fabrication techniques. The FWHM of the resonance in the CD spectra is about 36 nm which could be a significant superiority for this chiral metasurface to become a promising candidate for chiral-molecule sensors. Because the mechanism is that different molecular chiral structures usually show differences in CD spectral shifts that is, however, very slight when I use chiral metasurface to sense them, thus, a sharper peak benefits to detect subtler differences in spectral shifts in order to improve the sensor's sensitivity.

Beside the pursuit of the pronounced optical chiral effects at visible range, the tunability is becoming more and more important ability that need to be considered when proposing a new chiral structure. Several related pioneer work has been done by varying either the chiral layer thickness[62] or the refractive index of the proximity dielectric environment[136]. Here, I propose a much more straight forward strategy to achieve the tunable chirality. Due to the nanoslit being the element of the chiral pattern, it provides a possibility that on the one hand I can simply tune the length of nanoslits so as to shift the CD peak corresponding to modify the resonance of the localized mode, on the other

hand the lattice period is set as a variable to modify the cell-cell interaction through modifying the near-field interference, which is ascribed to the effects of the propagating mode.

To verify this, I first prepared three arrays with identical unit cell (a=350nm, b=100nm, g=50nm) but various lattice periods (p=810nm, 830nm, 850nm). The experiment and simulation results with a good agreement are put in the figure 4.4a, b, in which an obvious blue shifting of the CD spectra is observed with the enlarged lattice periods from 810nm to 850nm. What's more, it can be noticed that the CD spectra shifting distance is proportional to the increment of the period (for experiments, 7nm CD spectra shifting corresponding to the period increment of 20nm), which indicates that beside the intrinsic chiral pattern contributes to the chiral optical responses by localized plasmon resonance, the lattice period can also make an influence by modifying the cell-cell coupling and thus, for applications, this proportional tunability enables the ability of superfine control of the chiral response, which means, for example, the device can be designed exactly to match the resonance of the targets.

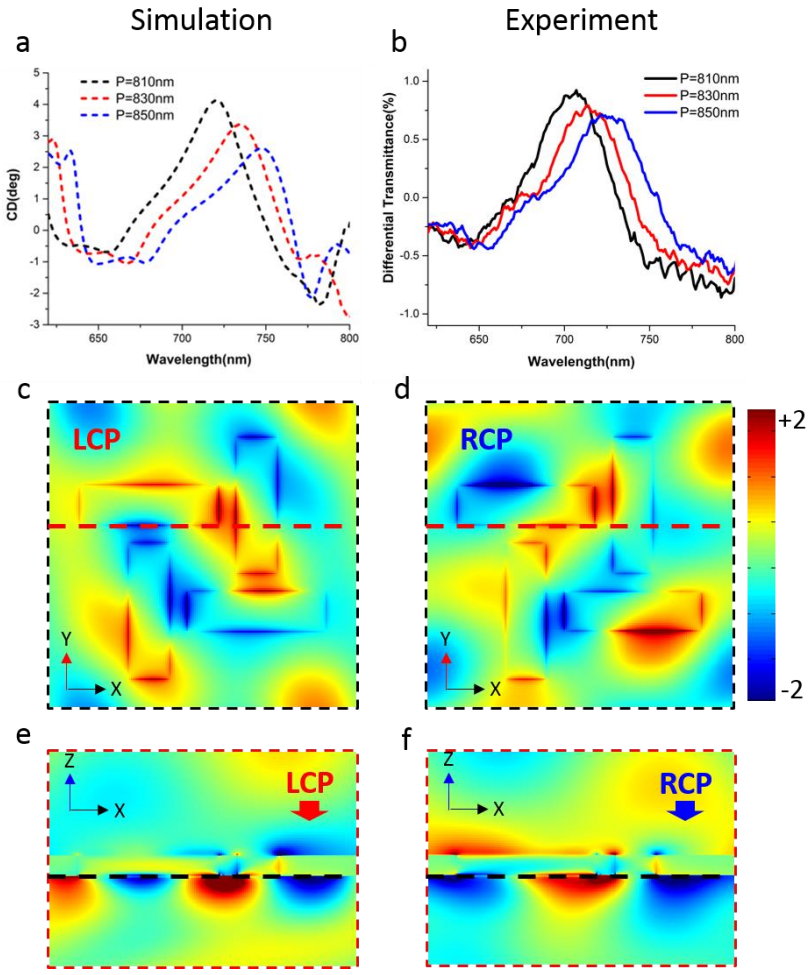

Figure 4.4. *Controlling the chiral response by varying the lattice period. (a) Simulation CD spectra and (b) experimental differential transmittance spectra for the array with identical unit cells but various periods of 810nm (black curve), 830nm (red curve) and 850nm (blue curve). For the array with the period of 830nm, the electric field Z-component distributions excited by LCP and RCP on the (c, d) bottom surface and cross-section (e, f) cut by the red dash line in figure 4c, d are mapped.*

The underlying mechanism can be understood as follow: the changing of the lattice period tunes the interference condition of the propagating mode so as to modify the collective CD spectra. For a clear demonstration, I map the electric field z-component

distribution with the circular polarized illumination of 735nm corresponding to the CD peak for both the bottom surface (figure 4.4c, d) and the cross-section (figure 4.4e, f) of the array with the period of 830nm. The model is simulated as an infinite array. Comparing the figure 4.4c, d to indicate, the surface plasmon resonance under the excitations of LCP and RCP displays an apparent asymmetric propagating feature on the near-field surface, which effectively enables the circular polarization dependent couplings among the chiral unit cells and results to a collective CD.

Therefore, through tuning the lattice period, the coupling is modified effectively to make the chiral response controllable and tunable. To be a contrast, the totally inverse chiral patterns in which nanorods replace the nanoslits with identical parameters have been also fabricated with the various lattices periods (p=810nm, 830nm, 850nm), however, there is no obvious shifting detected during the CD measurements (for the details, please see the support information), which may further indicate that the cell-cell coupling is a resultant of the propagating mode on the surface that is invalid for the inverse structures. Another interesting point here is that, the magnitude of the CD peaks drop with the enlarging lattice period. This phenomenon can be heuristically explained by considering the combination of the localized mode and the propagating mode. The unchanged unit cell will fix the localized mode and it exists an optimal parameter for the lattice period to offer the matched propagating mode corresponding to the localized mode, which will result to the strongest chiral response.

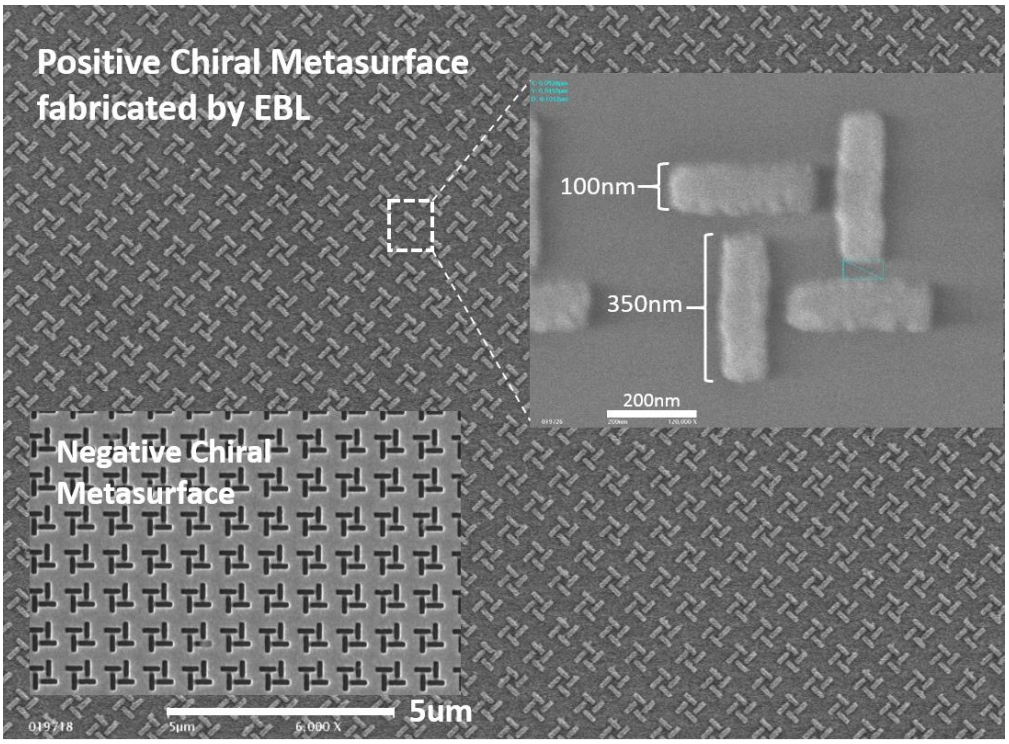

***Figure 4.5**. The inverse chiral metasurface (a=350nm, b=100nm, g=50nm, p=810nm) fabricated by E-beam lithography technology.*

In order to provide solid evidence of enabled tunability by propagating mode, the inverse chiral patterns have been also prepared as a reference that shown in the figure 4.5, in which nanorods replace the nanoslits with identical parameters for the unit cell and lattices periods (p=810 nm, 830 nm, 850 nm) and form the positive chiral pattern. The CD spectra of the positive patterns are demonstrated in figure 4.6 in which it can be easily detected there is no obvious shift in the CD with the enlarged lattice period from 810nm to 830nm. Form this, it can in further prove the existing of the propagating mode that can hardly happen in positive pattern possess the ability to modify the chiral responses by the cell-to-cell coupling.

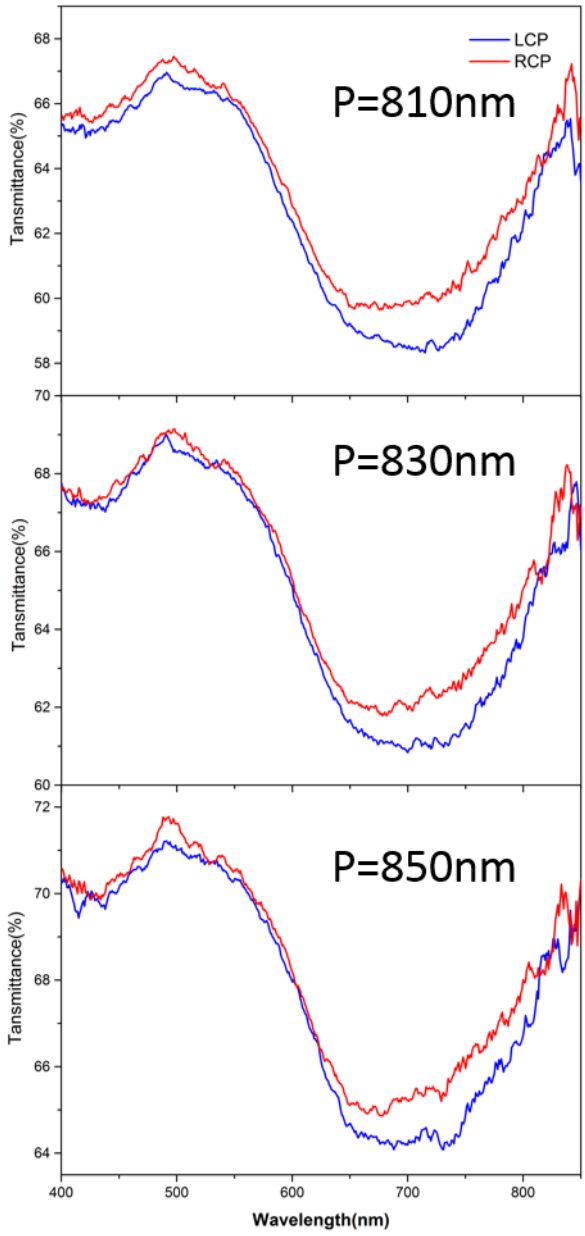

Figure 4.6. *The absolute transmittance spectra corresponds to left (blue curve) and right (red curve) circular polarized illumination of the positive chiral metasurface with various lattice periods (p=810/830/850nm). The obvious transmittance difference between the LCP and RCP excitation can be detected, however, there is no apparent shifting with sweeping the lattice period, which indicates no effective cell-cell coupling occurs.*

So far, the propagating mode has been proved to be a perfect tool for the fine tuning of the chiral optical response by the adjustment of the lattice period. However, the limitation is this tuning is just valid for a narrow wavelength range. In order to achieve a large tuning range, the localized mode is engaged. It has been mentioned the excited state of the nanoslits will highly influence the chiral responses, which indicates that the changing of the localized resonance by altering the length of the nanoslits can enable a big shift of CD. In order to experimentally demonstrate this 'coarse' tuning strategy, the samples with different nanoslit lengths of 300 nm, 350 nm and 400 nm have been fabricated. Due to the change of the length of the nanoslits, the shift of the localized mode is induced for the single slit, and in further resulting the shifted resonant profile of the chiral unit cell. Figures 4.7a, b and c illustrate the transmittance spectra of three left-enantiomer samples with different nanoslits length that corresponding to the three SEM images in figure 4.7d from top to bottom respectively. The enlargement of the slits length leads to a red shift of the optical chiral response across a significant wavelength range (>100 nm) as expected, which can be easily observed in Figure 4.7e where CD spectra of the three samples are put together and can be easily compared. Therefore, the tuning strategy of combining both the localized and propagating modes has been realized, which not only enables the coarse tuning by altering the length of the nanoslits, but also allows further fine tuning based on the coarse tuning via adjusting the lattice period. This combination could be summarized as having a 'coarse tuning +

fine tuning' knobs corresponding to the modification of the localized and propagating mode, respectively.

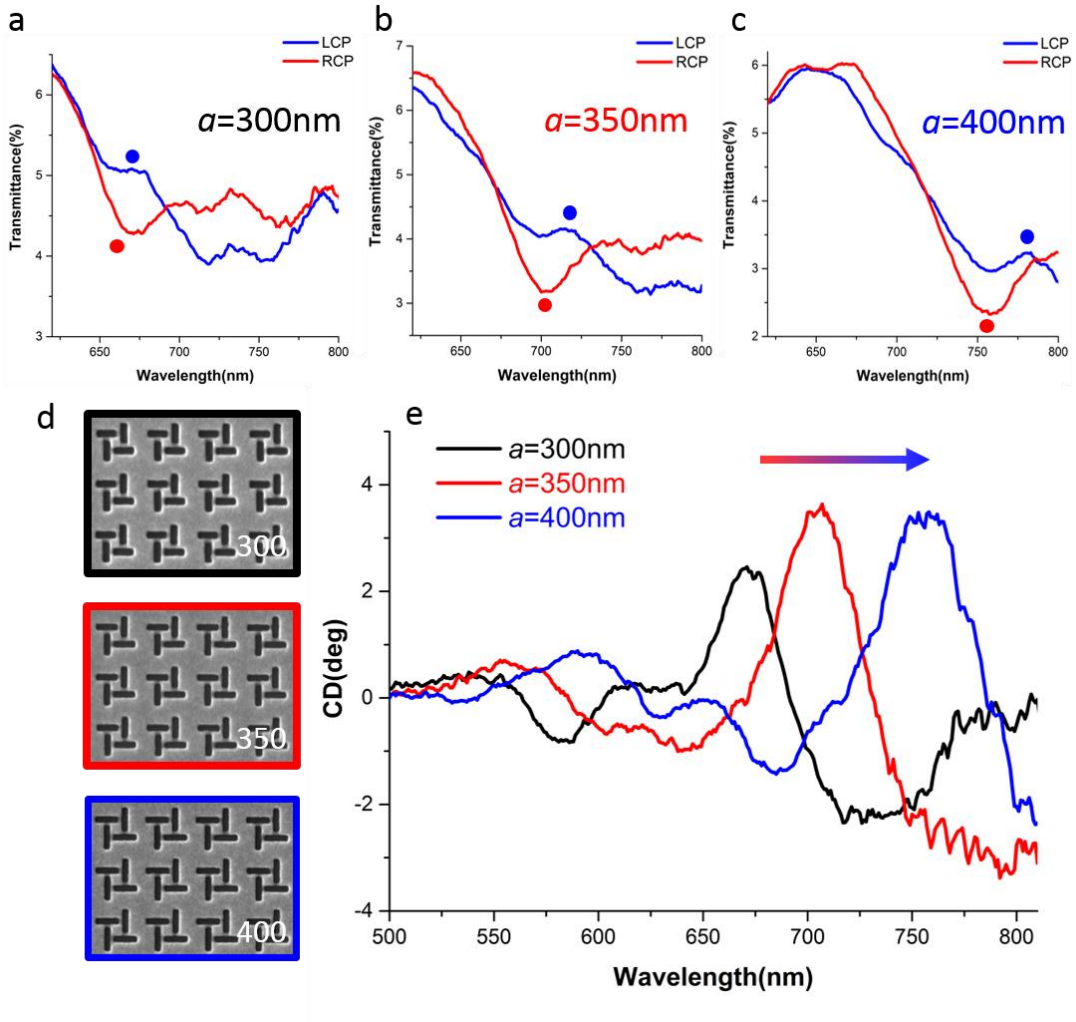

Figure 4.7*. Controlling the chiral response by modifying the localized mode. The absolute transmittance spectra of chiral metasurface with the various nanoslits length from (a) 300nm (a=300nm, b=50nm, p=750nm) to longer nanoslits of (b) 350nm (a=350nm, b=50nm, p=810nm) and (c) 400nm (a=400nm, b=50nm, p=890nm) under the illumination of LCP (blue curve) and RCP (red curve) respectively. (d) SEM images of the chiral metasurface with the various nanoslits length. (e) The CD spectra of the*

chiral metasurface with various length of nanoslits, in which the obvious blue shift can be observed corresponding to the shortening of the nanoslit.

4.4. Conclusion

Figure 4.8. *The illustration of the tuning strategy of 'coarse tuning knob + fine tuning knob'*

In conclusion, a novel metasurface with controllable chiral optical responses has been experimentally demonstrated in this work. A pronounced CD of 4 degree has been achieved, moreover the linewidth of the CD peak is very narrow around 36nm, which can highly benefit various applications, such as bio-sensing. More importantly, the influence of propagating mode on chiral optical responses has been clearly demonstrated, which in further is proved to have played an important role in negative chiral metasurfaces. What's more, based on the original localized mode plus the new tool of propagating mode, a strategy for controllable chiral responses is for the first time introduced, which is shown in figure 4.8. Via coupling the localized mode with the propagating mode in this chiral metasurface, two dependent 'knobs' are thus provided for both coarse and fine tuning of the chiral responses that on demand. This remarkable achievement will enable more space for this chiral metasurface to interact with other chiral materials.

Chapter 5. Resonant Coupling of CdSe/ZnS Quantum Dots and Chiral Metasurfaces for Enhanced Chiral Features

5.1 Introduction

Circularly polarized electromagnetic waves, which are in high demand in many fields, from distinguishing enantiomers[137,138] in life sciences to being standard qubits[139,140] in quantum computation and communication, are normally obtained by converting the linearly polarized waves from the light sources by inserting retardation optical elements which are expensive and bulky. Although with the advent of nanofabrication, compact integrated designs have been proposed[37,117,119], problems still exist in terms of energy losses and limited achromatic spectral range. In view of miniaturization and energy saving for optoelectronic devices, the direct control of the polarization states of emitters represents an extremely important step towards practical realization of next-generation optical systems. In recent years, many attempts have been made to achieve circularly polarized light (CPL) sources from various emitters, such as two dimensional materials[141,142], dye molecules[143,144], and semiconductor quantum dots (QDs)[88,145,146] which, due to the quantum confinement, show the brilliant merits of broad spectral tunability, high emitting efficiency and facile solution processibility and are therefore treated as an ideal emitter for many applications especially in nanoscale[147-151]. In order to employ these advantages, two main approaches have been proposed to

achieve QDs-based circularly polarized light emission. In the first, chiral ligands or molecules were connected to achiral QDs leading to circularly polarized luminescence and induced circular dichroism (CD)[145,152-155], however, the degree of the CPL measured was less than 1% of the total luminescence, thus making these CPL emitters very far from ideal. In the second approach, photonic crystal cavities[88,156,157] designed with chiral features, were coupled to the QDs and used to filter either the left or right CPL: this approach allowed to achieve a high degree of circular polarized emissions, nevertheless it required a very precise matching between the emission wavelength of the QDs and the photonic crystal cavity, which may be a limiting factor to their usability.

In recent years, plasmonic metamaterials[43,158-160] with engineered electromagnetic response have been used to modulate the photoluminescence (PL) properties of QDs, either for enhancing the PL intensity[161,162] or directly generating linearly polarized light (LPL) emission[83]. Concurrently, chiral metasurfaces[45,48-50,61,122,132] have realized with a remarkable ability in the manipulation of circular polarization: enormous values of CD have been reported[54,55,121], and strong chiral properties of the evanescent field in the vicinity of the chiral metasurfaces have been demonstrated[7,72,78], which not only offers a chiral platform for coupling various potential chiral systems, but also provides the possibility to break the time-reversal symmetry of achiral objects for highly efficient chiral light-matter interactions and opens a way to functionalize QDs possessing significant chiral properties.

In this work, I demonstrate a hybrid system in which controllable chiral metasurfaces are coupled with achiral semiconductor quantum dots. In order to explicitly reveal the interactions between the quantum emitters and plasmonic metasurfaces, I innovatively introduced tunable chiral responses from chiral metasurfaces to probe the unchanged achiral QDs and both the absorbing and emitting processes of such hybrid system have been studied. In the experiments I find that both processes possess clear chiral features which clearly suggests a coupling mechanism between the chiral metasurfaces and QDs. Firstly, circular dichroism spectroscopic measurements clearly indicate that, while QDs on unstructured surfaces show no preference for opposite spin excitations, QDs on chiral metasurfaces absorb preferentially for the circular polarization associated to the metasurfaces' chirality and more importantly, with the tuned chirality of chiral metasurfaces, the induced CD also moved accordingly, thus completely indicating the suggestion that the achiral QDs are chirally functionalized by the metasurface. Secondly, a preferential spin state was in further observed in the photoluminescence, leading to a high degree of circular polarization of 17%, which represent a new record for CdSe QDs based direct CPL emissions in the visible range. This work, as the first demonstration of hybrid QDs/chiral metasurface system, shows that the achiral CdSe QDs can be reshaped by certain chiral metasurfaces to turn into both an efficient CPL emitter and absorber, which holds a great potential for optimization and miniaturization of optical systems

which make use of circularly polarized light source, such as bio-sensing, bio-imaging, and quantum communications and may inspire the further work to achieve CPL laser.

5.2 Method

5.2.1 Nano-fabrication

The 100nm gold film was prepared by thermal evaporation after standard clean procedure for the sapphire substrate. A focus ion beam writer (FEI Helios 650) was utilized to fabricate the chiral metasurfaces. In order to guarantee the high quality of the chiral metasurfaces, I used the relatively small ion current of 7.7pA to etch the gold film.

5.2.2 Experimental characterizations

The continuous wave He-Cd laser delivering laser beam at optical wavelength of 442 nm was used as the excitation source. The laser power was set to be ~0.1mW such that negligible quenching effect was observed. The laser beam was focused onto the sample by an objective with diameter of ~50μm at an angle of ~45° to surface normal. The emission signal from the sample was collected in the forward direction and analyzed by a silicon-based charge coupled device equipped with an achromatic quarter wave plate (QWP, Thorlabs AQWP05M-600), a linear polarizer (LP, Thorlabs LPVISE200-A) and an achromatic half-wave plate. The achromatic quarter wave plate and the linear polarizer were used to select the targeted circular polarized emission and

the half-wave plate was utilized to fix the polarization of the emission into the monochromator. The setup used for CD measurements is same as the one in chapter 3 and 4.

5.3 Results and discussions

The chiral metasurface's design adopted to couple with QDs is schematically illustrated in the Figure 5.1a. The unit cells of this square lattice array are composed of 4 identical nanoslits fabricated by focus ion beam milling in gold film of 100nm in thickness. Scanning electron microscope (SEM) image of the chiral unit cell is shown in figure 5.1b with nanoslits of length 400nm, width 100nm and lattice period *P*. The neighboring nanoslits are perpendicular to each other and separated by a distance of 50nm. In chapter 4, this controllable chiral metasurface has been demonstrated and here, proper optical chiral response has been chosen by tuning the 2 'knobs' for the coupling with QDs.

I used canonical CdSe/ZnS core/shell QDs as the active materials. The photoluminescence spectrum of CdSe/ZnS QDs on a glass substrate peaks at 623nm as shown in figure 5.1c, while the individual quantum dots can be seen in the transmission electron microscope (TEM) image of figure 5.1d. The CD response of the chiral metasurface is tunable by simply altering the lattice period, as previously reported[122], which facilitates the resonance matching between the QDs and chiral metasurface.

Moreover, because of the circular polarization dependent surface plasmon polaritons (SPPs) that propagate between unit cells on the whole surface, the gold carved metasurface may enable a larger area of interaction between the random spin-coated QDs and metasurface.

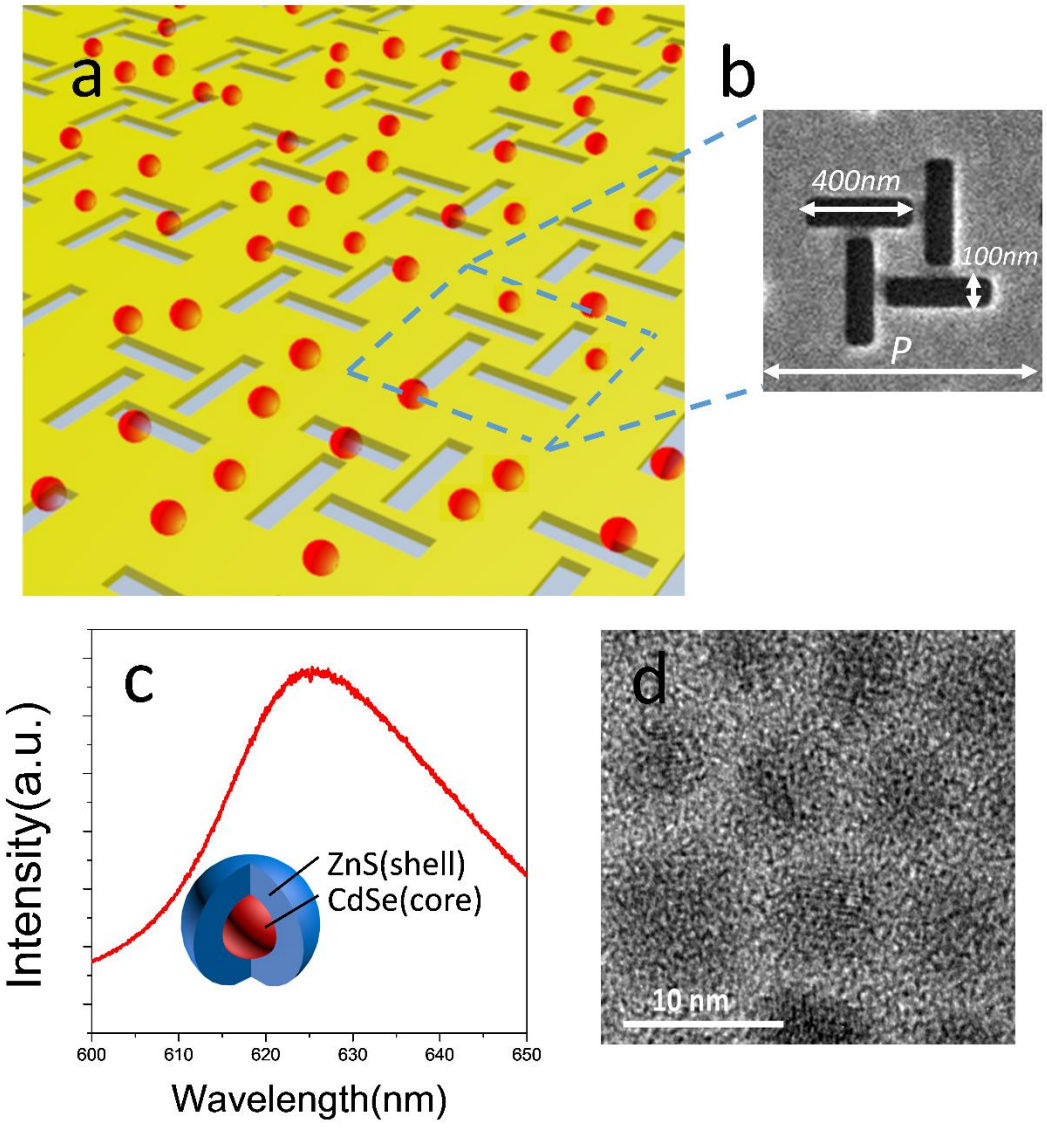

Figure 5.1. *QDs combined with chiral metasurfaces. (a)Schematic illustration of the hybrid system in which the red dots represent QDs and yellow film with slits is the chiral metasurface. (b) Scanning electron microscope (SEM) image of the chiral unit cell.*

(c)PL spectra of the CdSe QDs without chiral metasurface. (d)Transmission electron microscope (TEM) image of the QDs.

In order to reveal the interaction between the plasmonic chiral metasurface and QDs, CD spectroscopy technique is used to measure the transmission difference between the right and left CPL of the hybrid system. First, the chirality of the pure QDs, was determined by measuring CD spectrum of the QDs spin-coated on sapphire substrate. It should be noted that the spin-coating conditions were kept identical across all reported results, both on sapphire and metasurfaces. The results shown in the figure 5.2a obviously indicate that the QDs, as expected[144-146], show no preference for either left or right CPL. A chiral metasurface was then fabricated with lattice period P=1000nm and total square array area of 50μm×50μm: its CD spectrum is reported in the black curve of figure 5.2b, showing strong chiral responses in the visible range with a peak at 650nm. When the metasurface is hybridized with QDs, the CD spectral response of the hybrid system (red curve in figure 5.2b) shows a dramatic rise around the 617nm wavelength when compared to the bare chiral metasurface (black curve in figure 5.2b). The rise can be attributed to the fact that, at this wavelength, the hybrid metasurface/QDs system absorbs more right CPL than the bare chiral metasurface, while the pure QDs show no preference, as mentioned earlier. This confirms that there exists coupling between the CdSe QDs and chiral metasurface, inducing new chiral features. Full wave simulations (figure 5.2c) of the chiral metasurface show good spectral agreement to the experimental spectra (figure 5.2b) and show a clear

dependence of the spectral features on the excitation spin states, as shown in the electric field maps for LCP and RCP at the CD peak of 650nm (figure 5.2d and 5.2e). The figure 2f illustrates the experimental setup used to measure the CD, where a quarter waveplate is inserted in the optical path of a microspectrometer, to obtain the left and right CPL used to measure the CD, from the originally linearly polarized light.

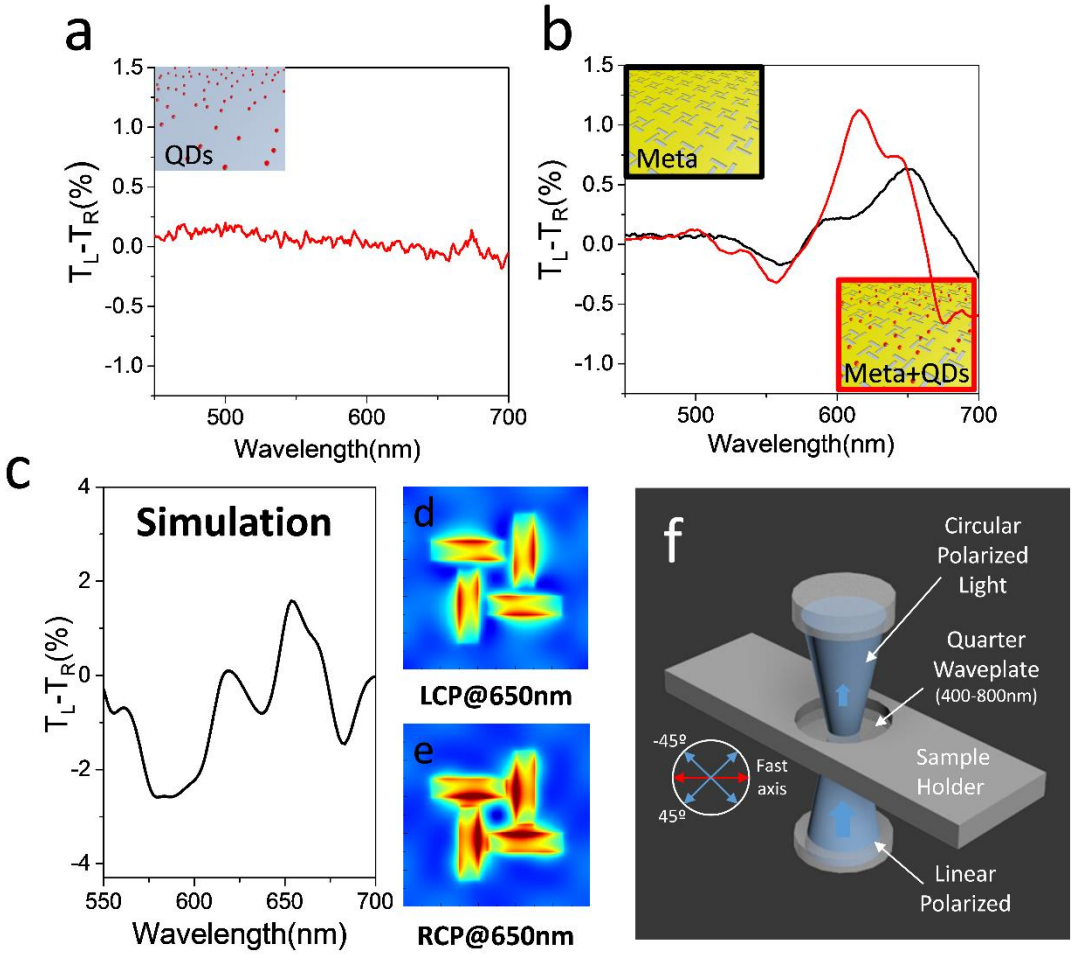

Figure 5.2. *Circular dichroism difference caused by introducing the achiral QDs on chiral metasurface. (a)CD spectrum of pure QDs on sapphire substrate. (b)CD spectrum of the chiral metasurface (black curve) and CD spectrum of the QDs combined chiral metasurface (red curve). (c) Stimulated CD spectrum of the chiral*

metasurface. (d)Electric field distribution of the chiral metasurface excited by LCP at the wavelength of 650nm. (e)Electric field distribution of the chiral metasurface excited by RCP at the wavelength of 650nm. (f)The setup for measuring the CD spectra by microspectrophotometer.

In order to explore the origin of the chiral features in the hybrid system, the QDs are combined with metasurfaces of varying lattice periods (900nm, 950nm and 1000nm), and the CD spectra of the bare metasurface and hybrid QDs/metasurface systems are compared on the background of the absorption spectrum of the bare CdSe QDs. Figure 5.3a reports the CD spectra for a metasurface with period P=1000nm: both the CD spectrum of the bare chiral metasurface (black curve) and the CD spectrum of the hybrid system (red curve) have two peaks (dashed arrows serve as guides for the eye), with the peak at shorter wavelength showing a significant increase in magnitude in the case of the hybrid metasurface/QD. To explain this phenomenon, I compare the CD spectra with the absorption of the QDs (blue dashed line) and find out that the positions of the CD increase well coincides with the peak in the QDs absorption spectrum while at longer wavelengths, where the QDs absorption is low, there is no obvious change detected (black dashed arrow). This confirms that the achiral CdSe/ZnS QDs can be chirally activated when its absorption bands overlap with the chiral responses of the metasurface. To verify this interpretation I fabricated chiral metasurfaces with identical unit cell but different lattice periods, which provide controllable shifting chiral responses. It should be emphasized here that the control of chirality is achieved by modifying the SPP propagating mode of the chiral metasurfaces.

Figure 3b shows a similar analysis for a chiral metasurface with period of 950nm, whose CD spectral peaks are ~20nm blue-shifted with respect to the metasurface of 1000 period (black curve in figure 5.3b). This implies that the overlap of the CD spectra with the QDs absorption spectra is also shifted and the effect is reflected in the CD spectrum of the hybrid system (red curve in figure 5.3b): the peak at longer wavelengths, which has now a better overlap with the QD absorption, shows a rise while a drop can be observed for the peak at shorter wavelength because its chiral response is shifting away from the absorbing peak of the QDs. A third metasurface, with period of 900nm and more blue-shifted chiral response was fabricated to confirm this trend (figure 5.3c): in this case the longer wavelength peak of the CD spectrum (black curve in figure 5.3c) fully overlaps with the absorption peak of the QDs (blue dashed line in figure 5.3c), resulting in a remarkable lift of the corresponding CD peak for the hybrid system (red curve in figure 5.3c), while the CD peak at short wavelengths, now overlapping with a dip in the QD absorption, almost disappears. The described differences in the behavior for the hybrid QD/metasurface system and the bare metasurface clearly suggest a preferential absorption of the right CPL for the CdSe QDs when combined with an appropriately designed chiral metasurface: this indicates that metasurfaces can used to induce chiral response into otherwise achiral CdSe QDs.

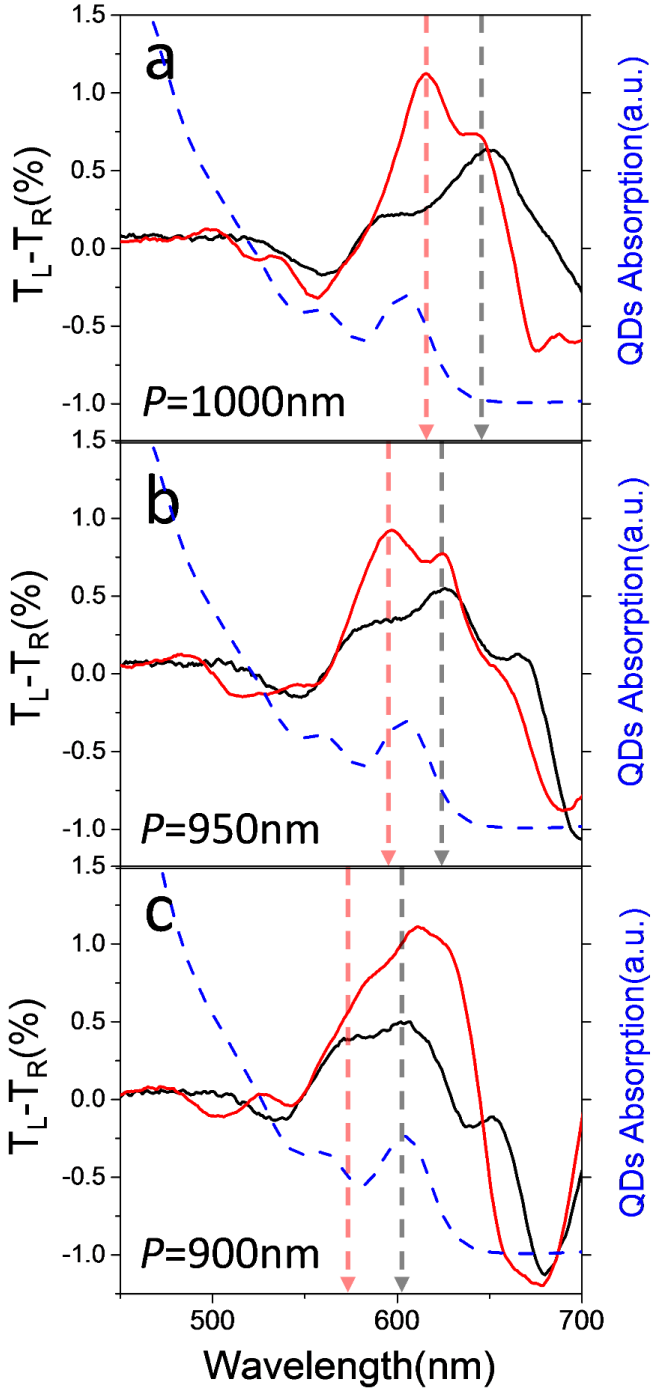

Figure 5.3. *QDs coupled with the chiral metasurfaces with various lattice periods. CD spectra of the chiral metasurfaces (black curve) and the QDs combined system (red curve) with the chiral metasurfaces' period of (a) 1000nm, (b) 950nm and (c) 900nm.*

I also studied the chiral response from the perspective of emission, and analyzed the luminescent circular polarizations of the hybrid chiral metasurface/QDs system of period P=1000nm: the setup is shown in figure 5.4a. The sample was excited by a continuous wave He-Cd laser at optical wavelength of 442 nm with an angle of ~45° to surface normal and the PL signal was collected in the forward direction and analyzed by a silicon-based charge-coupled device (CCD) equipped with a zero-order quarter-wave plate, a linear polarizer and an achromatic half-wave plate (see details in the Methods). In the experiments, I first measured the right and left circular polarized emission intensity of the QDs on the chiral metasurface and as a comparison, the QDs area without chiral pattern was also measured. The results are displayed in the figure 5.4b and 5.4c. It can be clearly observed that for the QD on the chiral metasurface, there is a very strong asymmetry in the right and left polarized PL intensity, which contributes to a degree of circularly polarized luminescence approaching 0.17 (figure 5.4b). The degree of circularly polarized luminescence g was determined to be as high as 0.17 based on the formula: $g = (I_L - I_R) / (I_L + I_R)$, where I_L, I_R represent the intensity of left and right circularly polarized luminescence, respectively. Since the CD of the metasurface is very small (~1%), the reabsorption effect (or filter-like effect) can be negligible compared to the remarkable PL chirality. Instead, for the QDs on unstructured substrate, the emission probability for a circularly polarized dipole is demonstrated to be identical for both spin states (figure 5.4c), which is also consistent with previous[145,146] reports and further proves the strong coupling between the QDs and chiral metasurface.

Consequently, for the emission process, I achieved remarkable CPL emitted directly from the QDs combined with the chiral metasurfaces and notably, this hybrid system works in free space and room temperature, which may enable practical CPL emitters and benefit various applications, such as bio-sensing.

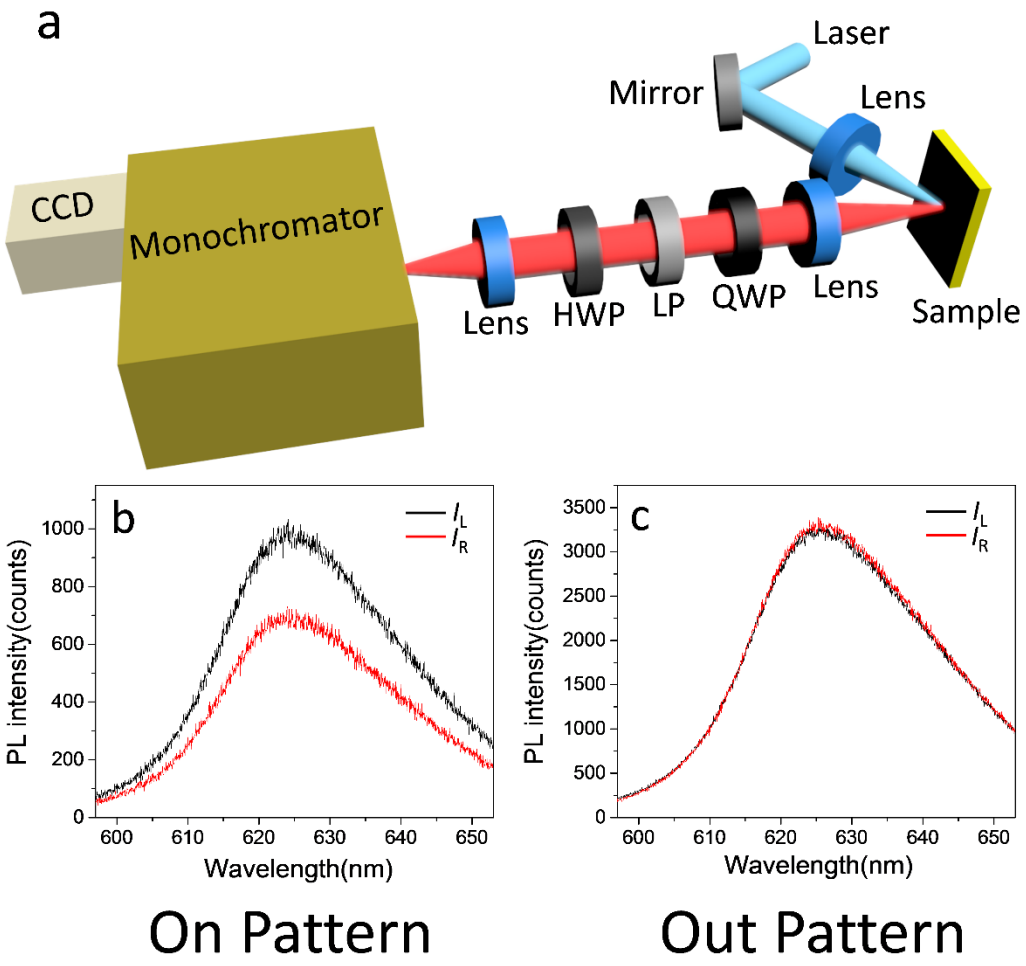

Figure 5.4. *CPL detected from the photoluminescence of the QDs combined system. (a) The setup adopted for measuring the luminescent circular polarizations from the QDs' emitting light. The experimental circular polarized PL intensity of the QDs (b) on the chiral metasurfaces and (c) out the chiral metasurface.*

5.4 Conclusion

In conclusion, I have demonstrated a hybrid system that uses chiral metasurfaces to induce surprising chiral properties into achiral QDs. First, by analyzing the CD and absorption spectra, it is shown that a significant CD can be induced by the chiral metasurfaces on the achiral QDs. In order to prove this phenomenon, I take advantage of a chiral metasurfaces with tunable chiral responses by simply altering the lattice period, coupled with the identical QDs: the results indicated that only if the chiral responses of the chiral metasurface overlap the QD absorption bands, enhanced chiral responses of the hybrid system can be detected. This is the first demonstration of chirally driving QDs by chiral metasurfaces and may open up a new way to study the QD spintronics. Second, a direct circular polarized emission from the proposed hybrid system has been achieved with a degree approaching to 0.17 which further demonstrates the strong coupling between the QDs and chiral metasurfaces. In the view of applications, I believe this proposed system and findings provide a new path to modulate QDs response with chirality and hold great potentials in various applications, including quantum communications, CPL lasers and bio-sensors.

Chapter 6. Conclusion and Future Work

6.1 Conclusion

This thesis focused on designing and realizing advanced chiral metasurfaces which not only performed significant chiral optical responses, but also as controllable chiral plasmonic platforms, enabled the manipulation of the light-matter interactions in chiral fashion. The demonstrations of the chiral metasurfaces show great potentials in controlling the emitting polarizations which may help to realize various applications, such as CPL laser. Hopefully, the work described in this thesis can shed light on the future studies on smarter chiral nanostructure and help to create more effective plasmonic biosensing platforms.

6.1.1 Introducing apexes in chiral metasurfaces for enhanced chiral responses

As shown in figure 6.1, apexes were introduced in a chiral metasurface by slightly overlapping the achiral nanoholes. These sharp nanostructures were demonstrated possessing the ability to greatly enhance the chiral property of the metasurface. In the far field, a 4 fold enhancement of CD is achieved with the apexes generated. More importantly, the apexes, regarded as super chiral hot spots enabled highly concentrated chiral field in the near field, which may lead to more efficient light-matter interactions for various applications.

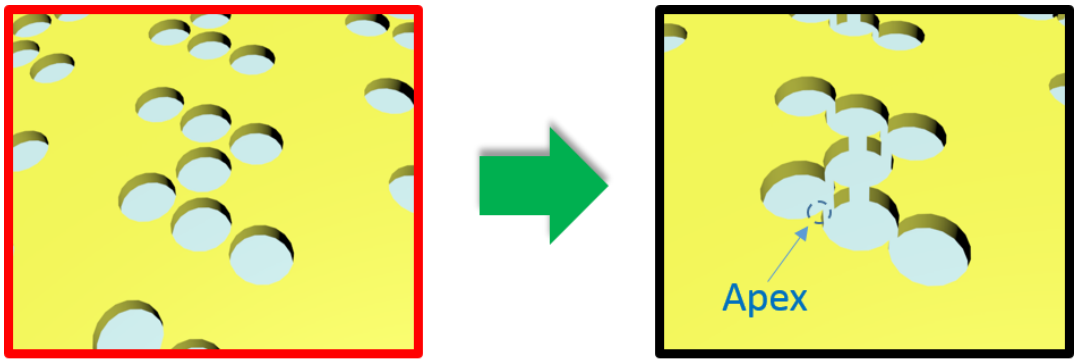

Figure 6.1. *Overlap the nanoholes to generate apexes in a chiral pattern*

6.1.2 Coupling localized and propagating modes for controllable chiral responses

In this work, a novel chiral metasurface composed by nanoslits has been demonstrated and showed remarkable controllable chiral responses ranging from visible to near-infrared frequency. By keeping the chiral unit cell unchanged and altering the lattice period, the shift of the CD spectra proved the existing influence of surface plasmon polaritons named propagating mode on the chiral responses of negative pattern. In further, via combing the propagating mode with localized mode, the chiral responses can be finely tuned to nanometer level in a wide range from 650nm to 800nm that displayed in figure 6.2. This tunability is believed can benefit many applications that need precise resonant coupling with optical chiral responses.

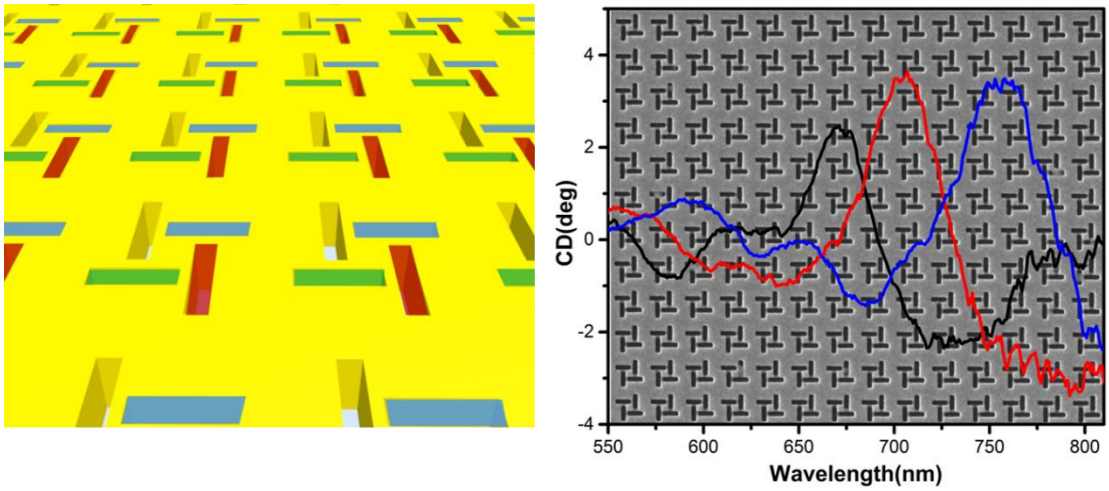

Figure 6.2. *A chiral metasurface formed by nanoslits for controllable chiral optical responses*

6.2.3 Coupling chiral metasurfaces with QDs for enhanced chiral effects

This work demonstrated the achiral CdSe QDs reshaped by the chiral metasurfaces to possess surprising chiral properties. Via employing the controllable chiral metasurface that mentioned in the chapter 4, the origin of the induced chiral features of the hybrid system was completely confirmed from the achiral QDs. Moreover, 17% circular polarization has been detected from the emission of the hybrid system, which has been displayed in figure 6.3. This is the first time induced chirality was achieved from achiral QDs by the coupling with chiral metasurface, which may provide a new path for the chiral modulation of active materials.

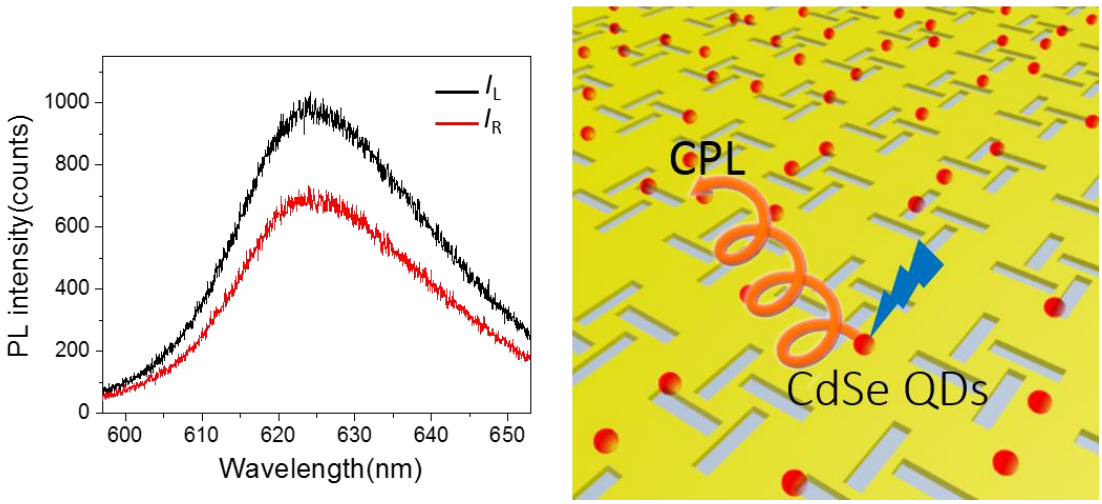

Figure 6.3. *CPL emission from QDs coupled with chiral metasurface*

6.2 Future work

Based on the work demonstrated in this thesis, there are two main directions for the future exploration. One is to move the chiral responses of metasurface into the UV range. Due to the excitation bands of numerous chiral biomolecules lie in the UV range, for the purpose of biosensing, the achievement of chiral responses in UV is significant. The obstacles existed in the poor performance of most plasmonic materials in UV and the fabrication of smaller metamolecules. Now with the rapid development of fabrication technique and wider and deeper investigations on diverse plasmonic materials[163-167], such as aluminum[168-172], it is very promising to found out the proper combination of materials and structures to provide solutions in the near future.

The other one is to utilize the chiral field that generated by chiral metasurface in the near field to interact with the spins in materials for various potential applications

shown in figure 6.4. The chiral metasurfaces demonstrated in this thesis have shown outstanding ability of generating intense chiral field which may trigger more efficient interactions between the optical chirality with the spins in materials. This rise of the interacting intensity will provide more space for the manipulations of the spins and in further activate more possibilities for semiconductor spintronic devices[173-178].

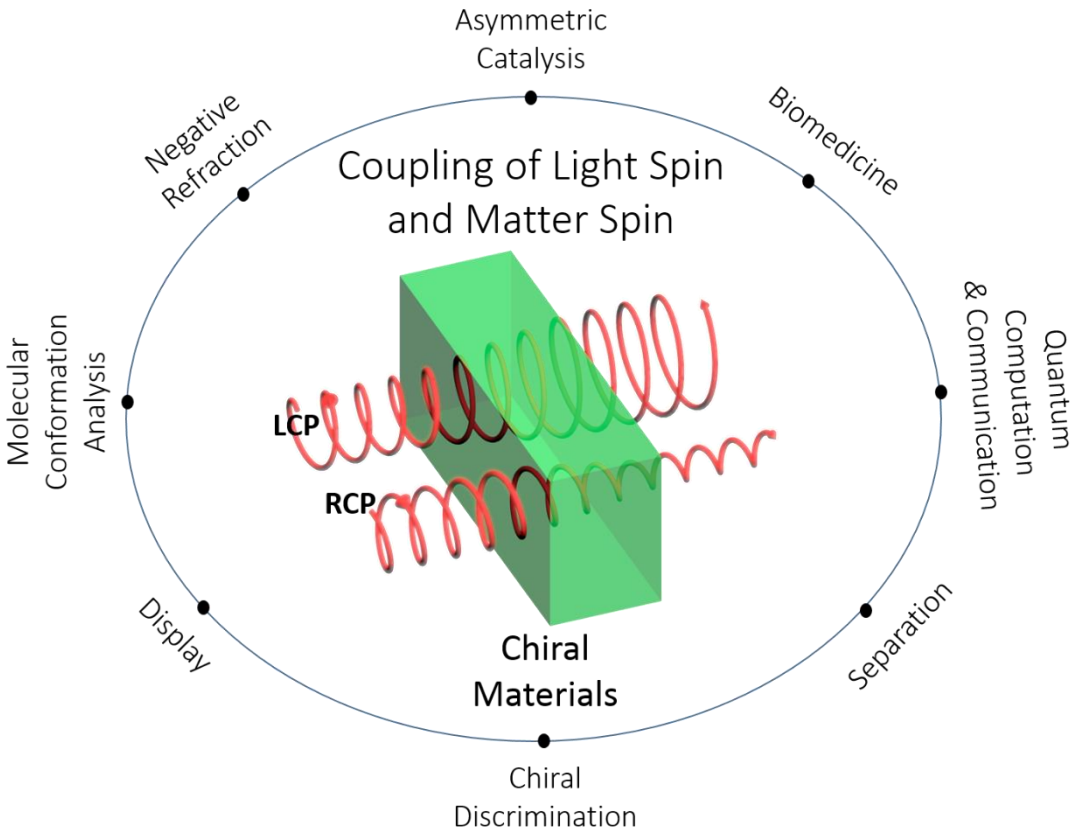

Figure 6.4. *The potential applications for the coupling of light spin and matter spin*

Transition metal chalcogenide (TMD) 2D materials have attracted tremendous attention beyond the 2D graphene in the last few years. This is because TMDs show layer dependent electronic structures. In particular, single layer TMDs have direct bandgap and large optical absorption falling in the near IR to visible wavelength

spectral range, which makes them promising for optoelectronic devices like LEDs, photodetector and solar cells etc. Figure 6.5 shows an ongoing work that coupling 2D materials[179,180] WSe_2 with chiral metasurfaces. This hexagonal 2D material[181-184] hosts two inequivalent electronic valleys that offering great potentials in both storing and transferring[185-187] binary. The efficient operations of the valleys requires strong spin-valley coupling[141,188-190], while the normal source CPL cannot offer strong optical spin for excitation, which results to harsh requirements for the spintronic operations. Therefore the intense optical spin that also named optical chirality generated by the chiral metasurface provides a big possibility to enable the strong spin-valley coupling. It can be observed the sample shown in the figure 6.5 is composed by both the left and right handed chiral metasurfaces and a single layer WSe_2 is pasted on both patterns. In next step, the valley responses of the WSe_2 will be measured, hopefully this hybrid system can achieve meaningful advances.

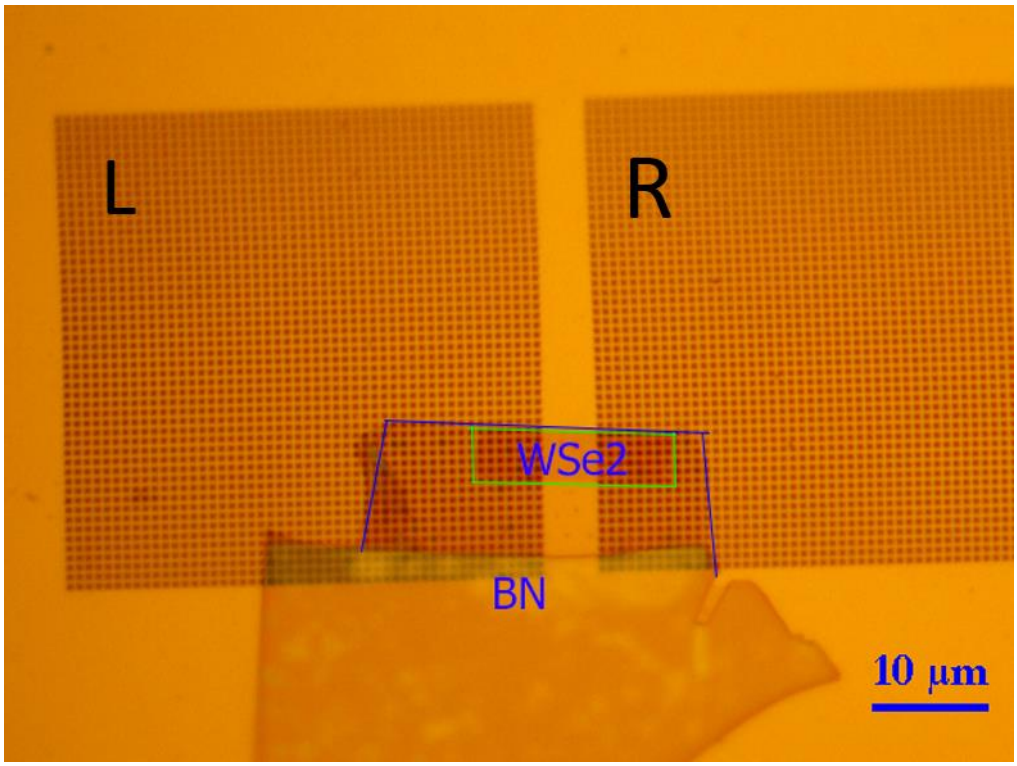

Figure 6.5. *The sample of coupling chiral metasurface with 2D materials*

Reference

1 Lakhtakia, A. Selected papers on natural optical activity. *Society of Photo Optical*, Vol. 15 (1990).

2 Nugent, W. A., RajanBabu, T. & Burk, M. J. Beyond nature's chiral pool: Enantioselective catalysis in industry. *SCIENCE-NEW YORK THEN WASHINGTON* **259**, 479-479 (1993).

3 Collins, A. N., Sheldrake, G. & Crosby, J. Chirality in industry II: Developments in the commercial manufacture and applications of optically active compounds. *John Wiley & Sons*, Vol. 2 (1997).

4 Lin, G. Q., You, Q. D. & Cheng, J. F. Chiral drugs: chemistry and biological action. *John Wiley & Sons* (2011).

5 Valev, V. K., Baumberg, J. J., Sibilia, C. & Verbiest, T. Chirality and chiroptical effects in plasmonic nanostructures: fundamentals, recent progress, and outlook. *Advanced Materials* **25**, 2517-2534 (2013).

6 Mori, K. Bioactive natural products and chirality. *Chirality* **23**, 449 (2011).

7 Tang, Y. & Cohen, A. E. Optical chirality and its interaction with matter. *Physical review letters* **104**, 163901 (2010).

8 Ha, N. Y. *et al.* Fabrication of a simultaneous red–green–blue reflector using single-pitched cholesteric liquid crystals. *Nature materials* **7**, 43-47 (2008).

9 Faraday, M. The Bakerian lecture: experimental relations of gold (and other metals) to light. *Philosophical Transactions of the Royal Society of London* **147**, 145-181 (1857).

10 Wood, R. W. On a remarkable case of uneven distribution of light in a diffraction grating spectrum. *Proceedings of the Physical Society of London* **18**, 269 (1902).

11 Chou, C.-H. & Chen, F.-C. Plasmonic nanostructures for light trapping in organic photovoltaic devices. *Nanoscale* **6**, 8444-8458 (2014).

12 Kelly, K. L., Coronado, E., Zhao, L. L. & Schatz, G. C. The Optical Properties of Metal Nanoparticles: The Influence of size, shape, and dielectric environment. *The Journal of Physical Chemistry B* **107**, 668-677 (2003).

13 Mie, G. Articles on the optical characteristics of turbid tubes, especially colloidal metal solutions. *Ann. Phys* **25**, 377-445 (1908).

14 Link, S. & El-Sayed, M. A. Size and temperature dependence of the plasmon absorption of colloidal gold nanoparticles. *The Journal of Physical Chemistry B* **103**, 4212-4217 (1999).

15 Bian, R. X., Dunn, R. C., Xie, X. S. & Leung, P. Single molecule emission characteristics in near-field microscopy. *Physical review letters* **75**, 4772 (1995).

16 Novotny, L., Bian, R. X. & Xie, X. S. Theory of nanometric optical tweezers. *Physical Review Letters* **79**, 645 (1997).

17 Yang, W. H., Schatz, G. C. & Van Duyne, R. P. Discrete dipole approximation for calculating extinction and Raman intensities for small particles with arbitrary shapes. *The Journal of chemical physics* **103**, 869-875 (1995).

18 Maradudin, A. A., Agranovich, V. & Mills, D. Surface Polaritons. *See, for example VM Agranovich, DL Mills (Eds.) North-Holland, Amsterdam*, 405 (1982).

19 Ebbesen, T. W., Lezec, H. J., Ghaemi, H., Thio, T. & Wolff, P. Extraordinary optical transmission through sub-wavelength hole arrays. *Nature* **391**, 667-669 (1998).

20 Martin-Moreno, L. *et al.* Theory of extraordinary optical transmission through subwavelength hole arrays. *Physical review letters* **86**, 1114 (2001).

21 Liu, H. & Lalanne, P. Microscopic theory of the extraordinary optical transmission. *Nature* **452**, 728-731 (2008).

22 Khanikaev, A. B., Mousavi, S. H., Shvets, G. & Kivshar, Y. S. One-way extraordinary optical transmission and nonreciprocal spoof plasmons. *Physical review letters* **105**, 126804 (2010).

23 Barnes, W. L., Dereux, A. & Ebbesen, T. W. Surface plasmon subwavelength optics. *Nature* **424**, 824-830 (2003).

24 Bozhevolnyi, S. I., Volkov, V. S., Devaux, E., Laluet, J.-Y. & Ebbesen, T. W. Channel plasmon subwavelength waveguide components including interferometers and ring resonators. *Nature* **440**, 508-511 (2006).

25 Oulton, R. F., Sorger, V. J., Genov, D., Pile, D. & Zhang, X. A hybrid plasmonic waveguide for subwavelength confinement and long-range propagation. *Nature Photonics* **2**, 496-500 (2008).

26 Walters, R. J., van Loon, R. V., Brunets, I., Schmitz, J. & Polman, A. A silicon-based electrical source of surface plasmon polaritons. *Nature Materials* **9**, 21-25 (2010).

27 Zayats, A. V., Smolyaninov, I. I. & Maradudin, A. A. Nano-optics of surface plasmon polaritons. *Physics reports* **408**, 131-314 (2005).

28 Kolesov, R. *et al.* Wave–particle duality of single surface plasmon polaritons. *Nature Physics* **5**, 470-474 (2009).

29 Tanaka, K. & Tanaka, M. Simulations of nanometric optical circuits based on surface plasmon polariton gap waveguide. *Applied Physics Letters* **82**, 1158-1160 (2003).

30 Huang, L. *et al.* Helicity dependent directional surface plasmon polariton excitation using a metasurface with interfacial phase discontinuity. *Light: Science & Applications* **2**, e70 (2013).

31 Pors, A., Nielsen, M. G., Bernardin, T., Weeber, J.-C. & Bozhevolnyi, S. I. Efficient unidirectional polarization-controlled excitation of surface plasmon polaritons. *Light: Science & Applications* **3**, e197 (2014).

32 Kildishev, A. V., Boltasseva, A. & Shalaev, V. M. Planar photonics with metasurfaces. *Science* **339**, 1232009 (2013).

33 Yu, N. & Capasso, F. Flat optics with designer metasurfaces. *Nature materials* **13**, 139-150 (2014).

34 Zheng, G. *et al.* Metasurface holograms reaching 80% efficiency. *Nature nanotechnology* **10**, 308-312 (2015).

35 Huang, L. *et al.* Three-dimensional optical holography using a plasmonic metasurface. *Nature communications* **4**, 2808 (2013).

36 Khorasaninejad, M. *et al.* Metalenses at visible wavelengths: Diffraction-limited focusing and subwavelength resolution imaging. *Science* **352**, 1190-1194 (2016).

37 Yu, N. *et al.* A broadband, background-free quarter-wave plate based on plasmonic metasurfaces. *Nano letters* **12**, 6328-6333 (2012).

38 Khoo, E. H., Li, E. P. & Crozier, K. B. Plasmonic wave plate based on subwavelength nanoslits. *Optics letters* **36**, 2498-2500 (2011).

39 Drezet, A., Genet, C. & Ebbesen, T. W. Miniature plasmonic wave plates. *Physical review letters* **101**, 043902 (2008).

40 Zhang, J., Zhang, L. & Xu, W. Surface plasmon polaritons: physics and applications. *Journal of Physics D: Applied Physics* **45**, 113001 (2012).

41 Pendry, J. Radiative exchange of heat between nanostructures. *Journal of Physics: Condensed Matter* **11**, 6621 (1999).

42 Smith, D. R., Pendry, J. B. & Wiltshire, M. C. Metamaterials and negative refractive index. *Science* **305**, 788-792 (2004).

43 Shalaev, V. M. Optical negative-index metamaterials. *Nature photonics* **1**, 41-48 (2007).

44 Valentine, J. *et al.* Three-dimensional optical metamaterial with a negative refractive index. *nature* **455**, 376-379 (2008).

45 Zhang, S. *et al.* Negative refractive index in chiral metamaterials. *Physical review letters* **102**, 023901 (2009).

46 Soukoulis, C. M., Linden, S. & Wegener, M. Negative refractive index at optical wavelengths. *Science* **315**, 47-49 (2007).

47 Schwanecke, A. *et al.* Broken time reversal of light interaction with planar chiral nanostructures. *Physical review letters* **91**, 247404 (2003).

48 Kuwata-Gonokami, M. *et al.* Giant optical activity in quasi-two-dimensional planar nanostructures. *Physical review letters* **95**, 227401 (2005).

49 Fedotov, V., Schwanecke, A., Zheludev, N., Khardikov, V. & Prosvirnin, S. Asymmetric transmission of light and enantiomerically sensitive plasmon resonance in planar chiral nanostructures. *Nano Letters* **7**, 1996-1999 (2007).

50 Fedotov, V. *et al.* Asymmetric propagation of electromagnetic waves through a planar chiral structure. *Physical review letters* **97**, 167401 (2006).

51 Gansel, J. K. *et al.* Gold helix photonic metamaterial as broadband circular polarizer. *Science* **325**, 1513-1515 (2009).

52 Helgert, C. *et al.* Chiral metamaterial composed of three-dimensional plasmonic nanostructures. *Nano letters* **11**, 4400-4404 (2011).

53 Hendry, E., Mikhaylovskiy, R., Barron, L., Kadodwala, M. & Davis, T. J. Chiral electromagnetic fields generated by arrays of nanoslits. *Nano letters* **12**, 3640-3644 (2012).

54 Hentschel, M., Schäferling, M., Weiss, T., Liu, N. & Giessen, H. Three-dimensional chiral plasmonic oligomers. *Nano letters* **12**, 2542-2547 (2012).

55 Cui, Y., Kang, L., Lan, S., Rodrigues, S. & Cai, W. Giant chiral optical response from a twisted-arc metamaterial. *Nano letters* **14**, 1021-1025 (2014).

56 Esposito, M. *et al.* Three Dimensional Chiral Metamaterial Nanospirals in the Visible Range by Vertically Compensated Focused Ion Beam Induced‐Deposition. *Advanced Optical Materials* **2**, 154-161 (2014).

57 Plum, E. & Zheludev, N. I. Chiral mirrors. *Applied Physics Letters* **106**, 221901 (2015).

58 Hopkins, B., Poddubny, A. N., Miroshnichenko, A. E. & Kivshar, Y. S. Circular dichroism induced by Fano resonances in planar chiral oligomers. *Laser & Photonics Reviews* **10**, 137-146 (2016).

59 Cui, Z. Micro-nanofabrication: technologies and applications. *Springer* (2006).

60 Goldstein, J. Scanning electron microscopy and X-ray microanalysis: a text for biologists, materials scientists, and geologists. *Springer Science & Business Media* (2012).

61 Khanikaev, A. *et al.* Experimental demonstration of the microscopic origin of circular dichroism in two-dimensional metamaterials. *Nature communications* **7**, 12045 (2016).

62 Karimullah, A. S. *et al.* Disposable Plasmonics: Plastic Templated Plasmonic Metamaterials with Tunable Chirality. *Advanced Materials* **27**, 5610-5616 (2015).

63 De Leon, I. *et al.* Strong, spectrally-tunable chirality in diffractive metasurfaces. *Scientific reports* **5**, 13034 (2015).

64 Wu, C. *et al.* Spectrally selective chiral silicon metasurfaces based on infrared Fano resonances. *Nature communications* **5**, 3892(2014).

65 Kuzyk, A. *et al.* DNA-based self-assembly of chiral plasmonic nanostructures with tailored optical response. *Nature* **483**, 311-314 (2012).

66 Decker, M. *et al.* Strong optical activity from twisted-cross photonic metamaterials. *Optics letters* **34**, 2501-2503 (2009).

67 Esposito, M. *et al.* Programmable Extreme Chirality in the Visible by Helix-Shaped Metamaterial Platform. *Nano letters* **16**, 5823-5828 (2016).

68 Zhao, R., Zhang, L., Zhou, J., Koschny, T. & Soukoulis, C. Conjugated gammadion chiral metamaterial with uniaxial optical activity and negative refractive index. *Physical Review B* **83**, 035105 (2011).

69 Valev, V. K. *et al.* Nonlinear Superchiral Meta‐Surfaces: Tuning Chirality and Disentangling Non‐Reciprocity at the Nanoscale. *Advanced Materials* **26**, 4074-4081 (2014).

70 Rodrigues, S. P., Lan, S., Kang, L., Cui, Y. & Cai, W. Nonlinear imaging and spectroscopy of chiral metamaterials. *Advanced Materials* **26**, 6157-6162 (2014).

71 Su, H. *et al.* Multipolar Effects in the Optical Active Second Harmonic Generation from Sawtooth Chiral Metamaterials. *Scientific reports* **6**, 22061 (2016).

72 Hendry, E. *et al.* Ultrasensitive detection and characterization of biomolecules using superchiral fields. *Nature nanotechnology* **5**, 783-787 (2010).

73 Banzer, P., Woźniak, P., Mick, U., De Leon, I. & Boyd, R. W. Chiral optical response of planar and symmetric nanotrimers enabled by heteromaterial selection. *Nature communications* **7**, 13117 (2016).

74 Kong, J. A. Theory of electromagnetic waves. *New York, Wiley-Interscience, 1975. 348 p.* (1975).

75 Li, Z. *et al.* Chiral metamaterials with negative refractive index based on four “U” split ring resonators. *Applied Physics Letters* **97**, 081901 (2010).

76 Lipkin, D. M. Existence of a new conservation law in electromagnetic theory. *Journal of Mathematical Physics* **5**, 696-700 (1964).

77 Jack, C. *et al.* Biomacromolecular stereostructure mediates mode hybridization in chiral plasmonic nanostructures. *Nano Letters* **16**, 5806-5814 (2016).

78 Tang, Y. & Cohen, A. E. Enhanced enantioselectivity in excitation of chiral molecules by superchiral light. *Science* **332**, 333-336 (2011).

79 Vecchi, G., Giannini, V. & Rivas, J. G. Shaping the fluorescent emission by lattice resonances in plasmonic crystals of nanoantennas. *Physical review letters* **102**, 146807 (2009).

80 Munechika, K. *et al.* Spectral control of plasmonic emission enhancement from quantum dots near single silver nanoprisms. *Nano letters* **10**, 2598-2603 (2010).

81 Russell, K. J., Liu, T.-L., Cui, S. & Hu, E. L. Large spontaneous emission enhancement in plasmonic nanocavities. *Nature Photonics* **6**, 459-462 (2012).

82 Okamoto, K. *et al.* Surface-plasmon-enhanced light emitters based on InGaN quantum wells. *Nature materials* **3**, 601-605 (2004).

83 Ren, M. *et al.* Linearly polarized light emission from quantum dots with plasmonic nanoantenna arrays. *Nano letters* **15**, 2951-2957 (2015).

84 Ming, T. *et al.* Strong polarization dependence of plasmon-enhanced fluorescence on single gold nanorods. *Nano letters* **9**, 3896-3903 (2009).

85 Lozano, G. *et al.* Plasmonics for solid-state lighting: enhanced excitation and directional emission of highly efficient light sources. *Light: Science & Applications* **2**, e66 (2013).

86 Coenen, T., Vesseur, E. J. R., Polman, A. & Koenderink, A. F. Directional emission from plasmonic yagi–uda antennas probed by angle-resolved cathodoluminescence spectroscopy. *Nano letters* **11**, 3779-3784 (2011).

87 Konishi, K. *et al.* Circularly polarized light emission from semiconductor planar chiral nanostructures. *Physical review letters* **106**, 057402 (2011).

88 Lobanov, S. *et al.* Controlling circular polarization of light emitted by quantum dots using chiral photonic crystal slabs. *Physical Review B* **92**, 205309 (2015).

89 Biswas, A. *et al.* Advances in top–down and bottom–up surface nanofabrication: Techniques, applications & future prospects. *Advances in colloid and interface science* **170**, 2-27 (2012).

90 Mijatovic, D., Eijkel, J. & Van Den Berg, A. Technologies for nanofluidic systems: top-down vs. bottom-up—a review. *Lab on a Chip* **5**, 492-500 (2005).

91 George, S. M. Atomic layer deposition: an overview. *Chemical reviews* **110**, 111-131 (2009).

92 Whitesides, G. M. & Grzybowski, B. Self-assembly at all scales. *Science* **295**, 2418-2421 (2002).

93 Xiao, S. *et al.* Selfassembly of metallic nanoparticle arrays by DNA scaffolding. *Journal of Nanoparticle Research* **4**, 313-317 (2002).

94 Wong, A. K.K. Resolution enhancement techniques in optical lithography. *SPIE press*, Vol. 47 (2001).

95 Chen, W. & Ahmed, H. Fabrication of 5 – 7 nm wide etched lines in silicon using 100 keV electron - beam lithography and polymethylmethacrylate resist. *Applied physics letters* **62**, 1499-1501 (1993).

96 Reyntjens, S. & Puers, R. A review of focused ion beam applications in microsystem technology. *Journal of micromechanics and microengineering* **11**, 287 (2001).

97 Giannuzzi, L. A. & Stevie, F. A. A review of focused ion beam milling techniques for TEM specimen preparation. *Micron* **30**, 197-204 (1999).

98 Melngailis, J. Focused ion beam technology and applications. *Journal of Vacuum Science & Technology B: Microelectronics Processing and Phenomena* **5**, 469-495 (1987).

99 Giannuzzi, L. A. Introduction to focused ion beams: instrumentation, theory, techniques and practice. *Springer Science & Business Media* (2006).

100 Tseng, A. A. Recent developments in micromilling using focused ion beam technology. *Journal of Micromechanics and Microengineering* **14**, R15 (2004).

101 Wu, H. *et al.* Focused helium ion beam deposited low resistivity cobalt metal lines with 10 nm resolution: implications for advanced circuit editing. *Journal of Materials Science. Materials in Electronics* **25**, 587 (2014).

102 Fu, Y. & Bryan, N. K. Semiconductor microlenses fabricated by one-step focused ion beam direct writing. *IEEE Transactions on semiconductor manufacturing* **15**, 229-231 (2002).

103 Ocelic, N. & Hillenbrand, R. Subwavelength-scale tailoring of surface phonon polaritons by focused ion-beam implantation. *Nature materials* **3**, 606-609 (2004).

104 Gierak, J. Focused ion beam technology and ultimate applications. *Semiconductor science and technology* **24**, 043001 (2009).

105 Volkert, C. A. & Minor, A. M. Focused ion beam microscopy and micromachining. *MRS bulletin* **32**, 389-399 (2007).

106 Vieu, C. *et al.* Electron beam lithography: resolution limits and applications. *Applied Surface Science* **164**, 111-117 (2000).

107 Tseng, A. A., Chen, K., Chen, C. D. & Ma, K. J. Electron beam lithography in nanoscale fabrication: recent development. *IEEE Transactions on Electronics Packaging Manufacturing* **26**, 141-149 (2003).

108 Fujita, J., Ohnishi, Y., Ochiai, Y. & Matsui, S. Ultrahigh resolution of calixarene negative resist in electron beam lithography. *Applied Physics Letters* **68**, 1297-1299 (1996).

109 Empedocles, S. A., Neuhauser, R., Shimizu, K. & Bawendi, M. G. Photoluminescence from single semiconductor nanostructures. *Advanced Materials* **11**, 1243-1256 (1999).

110 Kira, M., Jahnke, F. & Koch, S. Microscopic theory of excitonic signatures in semiconductor photoluminescence. *Physical review letters* **81**, 3263 (1998).

111 Perkowitz, S. Optical characterization of semiconductors: infrared, Raman, and photoluminescence spectroscopy. *Elsevier*, Vol. 14 (2012).

112 Meyer, B. *et al.* Bound exciton and donor–acceptor pair recombinations in ZnO. *physica status solidi (b)* **241**, 231-260 (2004).

113 Bogardus, E. H. & Bebb, H. B. Bound-exciton, free-exciton, band-acceptor, donor-acceptor, and Auger recombination in GaAs. *Physical Review* **176**, 993 (1968).

114 Decker, M., Klein, M., Wegener, M. & Linden, S. Circular dichroism of planar chiral magnetic metamaterials. *Optics letters* **32**, 856-858 (2007).

115 Plum, E., Fedotov, V. & Zheludev, N. Optical activity in extrinsically chiral metamaterial. *Applied Physics Letters* **93**, 191911 (2008).

116 Plum, E., Fedotov, V. & Zheludev, N. Extrinsic electromagnetic chirality in metamaterials. *Journal of Optics A: Pure and Applied Optics* **11**, 074009 (2009).

117 Zhao, Y., Belkin, M. & Alù, A. Twisted optical metamaterials for planarized ultrathin broadband circular polarizers. *Nature communications* **3**, 870 (2012).

118 Kang, L. *et al.* An Active Metamaterial Platform for Chiral Responsive Optoelectronics. *Advanced Materials* **27**, 4377-4383 (2015).

119 Du, L. *et al.* Broadband chirality-coded meta-aperture for photon-spin resolving. *Nature communications* **6**, 10051 (2015).

120 Fang, Y., Verre, R., Shao, L., Nordlander, P. & Käll, M. Hot electron generation and cathodoluminescence nanoscopy of chiral split ring resonators. *Nano Letters* **16**, 5183-5190 (2016).

121 Maoz, B. M., Ben Moshe, A., Vestler, D., Bar-Elli, O. & Markovich, G. Chiroptical effects in planar achiral plasmonic oriented nanohole arrays. *Nano letters* **12**, 2357-2361 (2012).

122 Wang, Z. *et al.* A Novel Chiral Metasurface with Controllable Circular Dichroism Induced by Coupling Localized and Propagating Modes. *Advanced Optical Materials* **4**, 883-888 (2016).

123 Banzer, P., Wozniak, P., Mick, U., De Leon, I. & Boyd, R. W. Chiral optical response of planar and symmetric nanotrimers enabled by heteromaterial selection. *Nature communications* **7**, 13117 (2016).

124 Gramotnev, D. K. & Bozhevolnyi, S. I. Plasmonics beyond the diffraction limit. *Nature photonics* **4**, 83-91 (2010).

125 Roxworthy, B. J. *et al.* Application of plasmonic bowtie nanoantenna arrays for optical trapping, stacking, and sorting. *Nano letters* **12**, 796-801 (2012).

126 Kinkhabwala, A. *et al.* Large single-molecule fluorescence enhancements produced by a bowtie nanoantenna. *Nature Photonics* **3**, 654-657 (2009).

127 Schäferling, M., Dregely, D., Hentschel, M. & Giessen, H. Tailoring enhanced optical chirality: design principles for chiral plasmonic nanostructures. *Physical Review X* **2**, 031010 (2012).

128 Tian, X., Fang, Y. & Sun, M. Formation of enhanced uniform chiral fields in symmetric dimer nanostructures. *Scientific reports* **5**, 17534(2015).

129 Ferry, V. E., Hentschel, M. & Alivisatos, A. P. Circular dichroism in off-resonantly coupled plasmonic nanosystems. *Nano Letters* **15**, 8336-8341 (2015).

130 Liu, N., Liu, H., Zhu, S. & Giessen, H. Stereometamaterials. *Nature Photonics* **3**, 157-162 (2009).

131 Plum, E. *et al.* Metamaterials: optical activity without chirality. *Physical review letters* **102**, 113902 (2009).

132 Singh, R. *et al.* Terahertz metamaterial with asymmetric transmission. *Physical Review B* **80**, 153104 (2009).

133 Kravets, V., Schedin, F. & Grigorenko, A. Extremely narrow plasmon resonances based on diffraction coupling of localized plasmons in arrays of metallic nanoparticles. *Physical review letters* **101**, 087403 (2008).

134 Auguié, B. & Barnes, W. L. Collective resonances in gold nanoparticle arrays. *Physical review letters* **101**, 143902 (2008).

135 Maier, S. A. Plasmonics: Fundamentals and Applications: Fundamentals and Applications. *Springer* (2007).

136 Yin, X. *et al.* Active Chiral Plasmonics. *Nano letters* **15**, 4255-4260 (2015).

137 Berova, N. & Nakanishi, K. Circular dichroism: principles and applications. *John Wiley & Sons* (2000).

138 Dolamic, I., Knoppe, S., Dass, A. & Bürgi, T. First enantioseparation and circular dichroism spectra of Au38 clusters protected by achiral ligands. *Nature communications* **3**, 798 (2012).

139 Duan, L.-M., Cirac, J., Zoller, P. & Polzik, E. Quantum communication between atomic ensembles using coherent light. *Physical review letters* **85**, 5643 (2000).

140 Aolita, L. & Walborn, S. Quantum communication without alignment using multiple-qubit single-photon states. *Physical review letters* **98**, 100501 (2007).

141 Mak, K. F., He, K., Shan, J. & Heinz, T. F. Control of valley polarization in monolayer MoS2 by optical helicity. *Nature nanotechnology* **7**, 494-498 (2012).

142 Zeng, H., Dai, J., Yao, W., Xiao, D. & Cui, X. Valley polarization in MoS2 monolayers by optical pumping. *Nature nanotechnology* **7**, 490-493 (2012).

143 Sánchez-Carnerero, E. M. *et al.* Circularly polarized luminescence by visible-light absorption in a chiral O-BODIPY dye: unprecedented design of CPL organic molecules from achiral chromophores. *Journal of the American Chemical Society* **136**, 3346-3349 (2014).

144 Meinzer, N., Hendry, E. & Barnes, W. L. Probing the chiral nature of electromagnetic fields surrounding plasmonic nanostructures. *Physical Review B* **88**, 041407 (2013).

145 Tohgha, U. *et al.* Ligand induced circular dichroism and circularly polarized luminescence in CdSe quantum dots. *ACS nano* **7**, 11094-11102 (2013).

146 Mukhina, M. V. *et al.* Intrinsic chirality of CdSe/ZnS quantum dots and quantum rods. *Nano letters* **15**, 2844-2851 (2015).

147 Alivisatos, A. P. Semiconductor clusters, nanocrystals, and quantum dots. *Science* **271**, 933 (1996).

148 Norris, D. & Bawendi, M. Measurement and assignment of the size-dependent optical spectrum in CdSe quantum dots. *Physical Review B* **53**, 16338 (1996).

149 Wang, Y. *et al.* Stimulated emission and lasing from CdSe/CdS/ZnS core‐multi‐shell quantum dots by simultaneous three‐photon absorption. *Advanced Materials* **26**, 2954-2961 (2014).

150 Wang, Y. *et al.* Blue liquid lasers from solution of CdZnS/ZnS ternary alloy quantum dots with quasi‐continuous pumping. *Advanced Materials* **27**, 169-175 (2015).

151 Wang, Y. *et al.* All‐Inorganic Colloidal Perovskite Quantum Dots: A New Class of Lasing Materials with Favorable Characteristics. *Advanced Materials* **27**, 7101-7108 (2015).

152 Ben-Moshe, A., Teitelboim, A., Oron, D. & Markovich, G. Probing the Interaction of Quantum Dots with Chiral Capping Molecules Using Circular Dichroism Spectroscopy. *Nano Letters* **16**, 7467-7473 (2016).

153 Moloney, M. P., Govan, J., Loudon, A., Mukhina, M. & Gun'ko, Y. K. Preparation of chiral quantum dots. *Nature protocols* **10**, 558-573 (2015).

154 Moloney, M. P., Gun'ko, Y. K. & Kelly, J. M. Chiral highly luminescent CdS quantum dots. *Chemical Communications*, 3900-3902 (2007).

155 Elliott, S. D., Moloney, M. c. l. P. & Gun'ko, Y. K. Chiral shells and achiral cores in CdS quantum dots. *Nano letters* **8**, 2452-2457 (2008).

156 Lobanov, S. V. *et al.* Polarization control of quantum dot emission by chiral photonic crystal slabs. *Optics letters* **40**, 1528-1531 (2015).

157 Maksimov, A. *et al.* Circularly polarized light emission from chiral spatially-structured planar semiconductor microcavities. *Physical Review B* **89**, 045316 (2014).

158 Smith, D., Pendry, J. & Wiltshire, M. Metamaterials and negative refractive index. *Science* **305**, 788-792 (2004).

159 Zhang, S., Genov, D. A., Wang, Y., Liu, M. & Zhang, X. Plasmon-induced transparency in metamaterials. *Physical Review Letters* **101**, 047401 (2008).

160 Cui, T. J., Smith, D. R. & Liu, R. Metamaterials. *Springer* (2014).

161 Tanaka, K., Plum, E., Ou, J., Uchino, T. & Zheludev, N. Multifold enhancement of quantum dot luminescence in plasmonic metamaterials. *Physical review letters* **105**, 227403 (2010).

162 Plum, E., Fedotov, V., Kuo, P., Tsai, D. & Zheludev, N. Towards the lasing spaser: controlling metamaterial optical response with semiconductor quantum dots. *Optics express* **17**, 8548-8551 (2009).

163 Alcaraz de la Osa, R. *et al.* Rhodium tripod stars for UV plasmonics. *The Journal of Physical Chemistry C* **119**, 12572-12580 (2015).

164 Blaber, M. G., Arnold, M. D. & Ford, M. J. A review of the optical properties of alloys and intermetallics for plasmonics. *Journal of Physics: Condensed Matter* **22**, 143201 (2010).

165 McMahon, J. M., Schatz, G. C. & Gray, S. K. Plasmonics in the ultraviolet with the poor metals Al, Ga, In, Sn, Tl, Pb, and Bi. *Physical Chemistry Chemical Physics* **15**, 5415-5423 (2013).

166 Appusamy, K., Jiao, X., Blair, S., Nahata, A. & Guruswamy, S. Mg thin films with Al seed layers for UV plasmonics. *Journal of Physics D: Applied Physics* **48**, 184009 (2015).

167 Jeong, H.-H., Mark, A. G. & Fischer, P. Magnesium plasmonics for UV applications and chiral sensing. *Chemical Communications* **52**, 12179-12182 (2016).

168 Knight, M. W. *et al.* Aluminum plasmonic nanoantennas. *Nano letters* **12**, 6000-6004 (2012).

169 Huang, Y.-W. *et al.* Aluminum plasmonic multicolor meta-hologram. *Nano letters* **15**, 3122-3127 (2015).

170 Martin, J., Proust, J., Gérard, D. & Plain, J. Localized surface plasmon resonances in the ultraviolet from large scale nanostructured aluminum films. *Optical Materials Express* **3**, 954-959 (2013).

171 Knight, M. W. *et al.* Aluminum for plasmonics. *ACS nano* **8**, 834-840 (2013).

172 Castro-Lopez, M., Brinks, D., Sapienza, R. & van Hulst, N. F. Aluminum for nonlinear plasmonics: resonance-driven polarized luminescence of Al, Ag, and Au nanoantennas. *Nano letters* **11**, 4674-4678 (2011).

173 Yamanouchi, M., Chiba, D., Matsukura, F. & Ohno, H. Current-induced domain-wall switching in a ferromagnetic semiconductor structure. *Nature* **428**, 539 (2004).

174 Pershin, Y. V. & Di Ventra, M. Spin memristive systems: Spin memory effects in semiconductor spintronics. *Physical Review B* **78**, 113309 (2008).

175 Gardelis, S., Smith, C., Barnes, C., Linfield, E. & Ritchie, D. Spin-valve effects in a semiconductor field-effect transistor: A spintronic device. *Physical Review B* **60**, 7764 (1999).

176 Flatté, M. E. Semiconductor Spintronic Devices. *Handbook of Magnetism and Advanced Magnetic Materials* (2007).

177 Awschalom, D. D. & Flatté, M. E. Challenges for semiconductor spintronics. *Nature physics* **3**, 153 (2007).

178 Bogani, L. & Wernsdorfer, W. Molecular spintronics using single-molecule magnets. *Nature materials* **7**, 179 (2008).

179 Xia, F., Wang, H., Xiao, D., Dubey, M. & Ramasubramaniam, A. Two-dimensional material nanophotonics. *Nature Photonics* **8**, 899-907 (2014).

180 Schaibley, J. R. *et al.* Valleytronics in 2D materials. *Nature Reviews Materials* **1**, 16055 (2016).

181 Jones, A. M. *et al.* Optical generation of excitonic valley coherence in monolayer WSe2. *Nature nanotechnology* **8**, 634-638 (2013).

182 Tonndorf, P. *et al.* Photoluminescence emission and Raman response of monolayer MoS 2, MoSe 2, and WSe 2. *Optics express* **21**, 4908-4916 (2013).

183 Huang, J.-K. *et al.* Large-area synthesis of highly crystalline WSe2 monolayers and device applications. *ACS nano* **8**, 923-930 (2013).

184 Fang, H. *et al.* High-performance single layered WSe2 p-FETs with chemically doped contacts. *Nano letters* **12**, 3788-3792 (2012).

185 Wolf, S. *et al.* Spintronics: a spin-based electronics vision for the future. *Science* **294**, 1488-1495 (2001).

186 Zibouche, N., Philipsen, P., Kuc, A. & Heine, T. Transition-metal dichalcogenide bilayers: Switching materials for spintronic and valleytronic applications. *Physical Review B* **90**, 125440 (2014).

187 Žutić, I., Fabian, J. & Sarma, S. D. Spintronics: Fundamentals and applications. *Reviews of modern physics* **76**, 323 (2004).

188 Xiao, D., Liu, G.-B., Feng, W., Xu, X. & Yao, W. Coupled spin and valley physics in monolayers of MoS 2 and other group-VI dichalcogenides. *Physical Review Letters* **108**, 196802 (2012).

189 Yuan, H. *et al.* Generation and electric control of spin–valley-coupled circular photogalvanic current in WSe2. *Nature nanotechnology* **9**, 851-857 (2014).

190 Grujić, M. M., Tadić, M. Ž. & Peeters, F. M. Spin-valley filtering in strained graphene structures with artificially induced carrier mass and spin-orbit coupling. *Physical review letters* **113**, 046601 (2014).